Methods for Time – Frequency – Space Parameterization of the Human Visual System

Dissertation

Zur Erlangung des akademischen Grades

Doktoringenieur (Dr.-Ing.)

vorgelegt der Fakultät für Informatik und Automatisierung

der Technischen Universität Ilmenau

von Dipl.-Ing.:   Andreas Halbleib

geboren am: 08.04.1978   **in:** Würzburg

vorgelegt am: Juni 2012

Gutachter: **1.) Univ.-Prof. Dr.-Ing. habil Jens Haueisen**

2.) Univ.-Prof. Dr. rer. nat. habil. Herbert Witte

3.) Univ. Prof. (assoc.) Dr. Eng. Tarek Elsarnagawy

Acknowledgments

The completion of this thesis would not have been possible without the contribution and support of many people, to whom I would like to express my deepest gratitude.

Many thanks go to my principal supervisor Prof. Dr. Jens Haueisen for his constant support, professional advice and guidance from the very early stage of the research. Furthermore I would like to thank him for giving me extraordinary experiences throughout the work. Above all, he provided unflinching encouragement and support in various ways.

I would like to thank Dr. Maciej Gratkowski for the motivating and pleasant collaboration. I am much indebted to him for his valuable advice and support. Additionally, I am very grateful for the friendship of all of the members of the institute, especially Daniel S., Sebastian, Patrique and Daniel L..

This work would not have been possible without the support of my family. I want to thank my parents for the understanding and support they showed.

The support and encouragement of my wife has been indispensable. Her patience, love and persistent encouragement were my basis for completing this work.

Abstract

Accurate parameterization and decomposition of brain activity are major engineering problems posed by neuroscience. Brain activity is usually generated by a multitude of neural sources. Additionally, the measurement of the signal is impaired by noise from biologic or technologic sources. With the purpose of gaining new insight into the mechanisms of the brain, a new strategy for topography analysis and a new method for proper simultaneous parameterization of neural activity are developed in this thesis. Both approaches hinge on the assumption that single neural oscillators generate the meaningful components of the recorded data. The Matching Pursuit (MP) algorithm approximates measured signals in the real valued case with windowed cosine functions, and, thus, serves as the basic method for the developed strategies.

The developed topographic analysis parameterizes recorded data and subsequently analyzes the statistical properties. The data stem from an experiment with 10 human subjects, in which flickering lights cause a steady-state response in the visual system. The newly developed strategy detects intra-individually similar topographies for small number of stimulation frequencies. However, inter-individually there is no similarity between the topographies. My analysis shows that approximately 10 stimuli are needed for a stable response. Additional results reveal that the topographies persist after the end of the stimulation. The results are not limited to the topographies, but also occur in the analysis of time and frequency parameters. The results support the theory of a coupled system and lead to the investigation of the spatial properties of the underlying neural oscillators.

The aim of the new method for localizing neural sources is simultaneously disentangling sources from noise and parameterizing in time, frequency and space. My source localization method retains the basic principle of Matching Pursuit and extends it by dipoles. This combination leads to the concepts of Dipole Atoms, which describe oscillators disentangled from noise in time, frequency and space. The method is developed further to allow for a set-up of two mirrored sources, so that it meets the requirements derived from the experiment. The goodness of parameter reconstruction of the new method is tested in simulations. Subsequently, the method is applied to the data from the flicker experiment. Mirrored Dipole Atoms reconstruct the time and frequency parameters identically to the topographic analysis and allow for the simultaneous spatial description of the underling sources.

As expected, the neural generators are located in the visual cortex on both hemispheres of the brain. The localization results are clearly distinguished into two subsets, one of which shows alpha entrainment while the other does not. The observations extend the understanding of the human visual system and lead to the formulation of a new stimulation paradigm.

Kurzfassung

Akkurate Parametrisierung und Dekomposition von Gehirnaktivität stellen bedeutende ingenieurtechnische Fragestellungen durch die Neurowissenschaften dar. Gehirnaktivität ist von einer Vielzahl von neuronalen Quellen generiert. Hinzu kommt, dass gemessene Signale durch Rauschen aus biologischen und technischen Quellen beeinträchtigt sind. Mit der Absicht neue Einsicht in die Funktionsweise des Gehirns zu gewinnen, werden in dieser Arbeit eine neue Strategie der topographischen Analyse und eine neue Methode für die geeignete Parametrisierung neuraler Aktivität entwickelt. Beide Herangehensweisen fußen auf der Annahme, dass neurale Oszillatoren die aussagekräftigen Komponenten der gemessenen Daten erzeugen. Die Matching Pursuit (MP) Methode approximiert gemessene Signale im realwertigen Fall mit gefensterten Cosinus-Funktionen, und dient somit als Grundlage für die entwickelten Strategien.

Die entwickelte topographische Analyse parametrisiert Messdaten und analysiert die statistischen Eigenschaften. Die Daten stammen von einem Experiment mit 10 Probanden, in welchem flackerndes Licht einen stationären Zustand im visuellen System erzeugt. Die neu entwickelte Strategie detektiert intra-individuell ähnliche Topographien bei einer kleinen Anzahl von Stimulationsfrequenzen. Jedoch besteht die Ähnlichkeit dieser Topographien nicht inter-individuell. Meine Analyse zeigt, dass ungefähr 10 Stimuli für eine stabile Antwort nötig sind. Weitere Ergebnisse enthüllen, dass diese Antworten nach Stimulationsende weiterexistieren. Diese Beobachtungen sind nicht auf die Topographien begrenzt, sondern treten auch in der Analyse der Zeit- und Frequenzparameter auf. Die Ergebnisse unterstützen die Theorie eines koppelten Systems und führen zur Untersuchung der räumlichen Eigenschaften der zugrunde liegenden neuralen Oszillatoren.

Das Ziel der neuen Methode für die Lokalisierung neurale Quellen ist das simultane Trennen der Quellen vom Rauschen, und die Parametrisierung in Zeit, Frequenz und Raum. Meine Quellenlokalisationsmethode behält das grundlegende Prinzip von Matching Pursuit bei und erweitert es um Dipole. Dies führt zum neuen Konzept der Dipol Atome, welche Oszillatoren in Zeit, Frequenz und Raum, vom Rauschen getrennt, beschreiben. Die Methode ist weiterentwickelt um gespiegelte Quellenkonfigurationen zu ermöglichen, so dass die aus dem Experiment hergeleiteten Anforderungen erfüllt werden. Die Güte der Parameter-rekonstruktion der neuen Methode wird in Simulation getestet. Daraufhin wird die Methode auf Messdaten aus dem Flackerlichtexperiment angewendet. Gespiegelte Dipol Atome rekonstruieren die Zeit- und Frequenzparameter identisch zur topographischen Analyse und erlauben eine räumliche Beschreibung der zugrunde liegenden Quellen.

Erwartungsgemäß werden neurale Generatoren im Visuellen Cortex beider Gehirnhälften gefunden. Die Lokalisationsergebnisse sind klar in zwei Gruppen unterteilt, wobei eine Gruppe so genanntes Alpha-Entrainment zeigt, während dies bei der Anderen nicht der Fall ist. Die Erkenntnisse erweitern das Verständniss des menschlichen visuellen Systems und führen zur Formulierung eines neuen Stimulationsparadigmas.

Table of Contents

Abbreviations and Symbols

Abbreviations

A17   Brodmann area 17

cc   Correlation coefficient

CSeq   Correlation sequence

CSF   Cerebrospinal fluid

DA   Dipole Atom

EP   Evoked Potential

GOF   Goodness of Fit

GFP   Global Field Power

LGN   Lateral Geniculate Nucleus

IN   Local-circuit Inter Neurons

IP   Induced Potential

M-/EEG   Magneto-/Electroencephalogram

MDM   Mean of distance means

MP   Matching Pursuit

(N)EG   (No-) Entrainment-group

O1/O2   Electrode positions according to international 10-20 System: Occipital 1 / 2

RE   Reticular Thalamic Neurons

RMSE   Root Mean Square Error

Sec   Secant

SNR   Signal to Noise Ratio

SQUID   Superconducting Quantum Interference Device

(SS)VEP   (Steady State) Visual Evoked Potential

STD   Standard Deviation

TMP   Topographic Matching Pursuit

TCR   Thalamo-Cortical Neurons

V1   Primary Visual Cortex

Var   Variance

Symbols

a	Atom weighing factor in the Matching Pursuit approximation
$\boldsymbol{B}$	Magnetic field
$dirx$	x -Direction of a dipole
$diry$	y -Direction of a dipole
$dirz$	z -Direction of a dipole
$\boldsymbol{E}$	Electric field
$\boldsymbol{F}$	Measured or calculated activity
Fr	Frequency
g	Gabor Atom
I	Electric current
$\boldsymbol{J}$	Electric current density
$\boldsymbol{J}_{loop}$	Total loop current flow
$\boldsymbol{J}_p$	Primary current density
$\boldsymbol{J}_v$	Secondary volume current
$\boldsymbol{L}$	Lead field
m	Amount of stimulation periods
n	Amount of Sensors
$\boldsymbol{Q}$	Current Dipole
$\boldsymbol{r}$	Radius/Position
Rf	Residual of a signal (in Matching Pursuit)
T	Stimulation period in the flicker experiment
V	Electrical potential
v	Single measured values
$\bar{v}$	Mean value of a number of single measured values v
x, y, z	Spatial coordinates of a dipole
$\delta(\boldsymbol{r})$	Dirac delta function
σ	Electrical conductivity
∇	Gradient operator

Parameter

K	Normalization factor of the Gabor Atom
l	Matching Pursuit Iteration depth and amount of atoms approximating a signal
s	Scale of the Gabor Atom
t	Time
u	Translation of a Gabor Atom
ξ	Modulation of a Gabor Atom
ϕ	Cosine-phase of a Gabor Atom

Indices

ag	Alpha-group
CL	Lower filter cut-off frequency
CH	Higher filter cut-off frequency
ch	Channel index in TMP
DA	Related to Dipole Atoms
fr	Stimulation frequency
FWD	Related to forward solutions
i	Channel index
ii	Channel index
ind	Individual
j	Index of the Gabor Atoms and the weighing factor
J	Amount of atoms approximating a time series
k	Residual index
$Meas$	Measured
$Mirr$	Related to mirrored Dipole Atoms
MP	Related to Matching Pursuit
nag	No-alpha-group
Q	Dipole
$samp$	Sampling rate
$Sensor$	Electric or magnetic sensor

si	Sample index
$sink$	(Current) sink
$source$	(Current) source
TMP	Related to Topographic Matching Pursuit
γ	Index of the atom approximating a time series $f(t)$

Units

m	Meter
V	Volt; Voltage
Ω	Ohm; Electric resistance
T	Tesla; Magnetic flux density

1. Motivation

In the 1920s Hans Berger constructed the first apparatus with the ability to measure the electroencephalogram (EEG) (Berger 1929). What he measured was the electrical activity of the brain in a range of 10Hz over the back of the head. Today this phenomenon of 8-13Hz activity over the occipital region of the head is called resting alpha (Chartrian et al. 1974). Although the alpha rhythm was the first activity discovered, up to today it is not completely understood how it is generated. Even the definitive configuration and interaction of the generators in the alpha system are not fully known. In this thesis a novel approach of data analysis is developed, which allows for insightful investigation of the brain response to rhythmic visual stimulation. Additionally, the development, evaluation and application of a new especially tailored method for the localization and detailed parameterization of the (neural) generators of the alpha system is presented. Both methods are successfully applied to experimental data, thus the gained results are analysed and interpreted with regard to their neuroscientific meaning.

The first aim of the data analysis is the investigation of spatial patterns (topographies) in recordings of the EEG and the magnetoencephalogram (MEG), which formed after repetitive visual stimulation of human subjects. The study is based on the working hypothesis that the topographies are generated by spatially fixed neural oscillators. The examination of the topographies yields indicative results regarding the spatial stability of the assumed underlying oscillators. The second aim is the quantification of the engagement and disengagement of the generators of neuronal activity by investigating the transient behaviour of the spatial patterns. Both research objectives are accomplished by parallel analysis of multi-trial and single-trial data. Besides the investigated oscillators, also other sources generate overlapping activity or noise. Before proceeding with the analysis, noise components have to be removed from the examined signal, while preserving the time-frequency-space properties of the signal and thus the topographies. In this work, the problem of noise is tackled by means of the Topographic Matching Pursuit (TMP (Gratkowski et al.2007; Gratkowski et al. 2008) algorithm. The analysis is followed by the interpretation and evaluation of the time-frequency-space parameters of the unravelled activity of the oscillators and topographies. The methodology, results and interpretation are published in (Halbleib et al. 2012).

Generally, the exact localization of neural sources is of high importance in the field of neuroscience. The engineering task derived from this requirement is the core aim of the development of the new source localization method. Further requirements from the scope of this work closely relate the source localization method to the investigation of spatial patterns and, more precisely, to pinpointing and identifying the underlying neural oscillators. Thus, the desired specifications of this technique do not only concentrate on the identification of the spatial properties of the generators, but also on the joint determination of its time and frequency parameters. Hence, the desired source localization method is developed as an extension to the Matching Pursuit (MP)-algorithm by incorporating spatial

parameters in the precise time-frequency characterization of the oscillations, while simultaneously unraveling the oscillatory activity from noise. Consequently, the aim of this work is the development, verification and application of a new source localization algorithm based on Topographic Matching Pursuit (TMP), which overcomes the constraints of the already existing source localization method linked to MP (Durka 2005). With the newly introduced concept of Dipole Atoms, the statistical findings of the topographic analysis are confirmed and refined, leading to a better understanding of underlying physiological processes.

The following chapters introduce the necessary concepts. Section 2.1 provides an overview of the anatomic and physiologic basics of the brain, the investigated visual system, repetitive visual stimulation and alpha entrainment. Section 2.2 gives an overview of the EEG and the MEG. Matching Pursuit and TMP are introduced in section 2.3. The technical concepts fundamental to source localization are described in section 2.4.

Section 3 presents the design of the experiment and states pre-processing steps.

Section 4 explains the details of the methodological developments, focussing on the topographic analysis of multi trial and single trial data (section 4.1), and the source localization tool including the novel concept of Dipole Atoms as well as the algorithmic and technical specifications (section 4.2).

The results of the topographic analysis are presented in section 5, by describing the fundamental properties of the data (section 5.1) and the actual topographic analysis (section 5.2) covering a range of parameters.

Section 6 is committed to the source localization tool. The results of various simulated scenarios are given in section 6.1, while the results obtained from the above mentioned experiment are explained in section 6.2.

The results presented in section 5 and 6 are discussed in section 7, where the insights gained from the topographic analysis are depicted in section 7.1, while the findings inferred from the source localization are presented in section 7.2. Model assumptions arising from the results of this thesis that may lead to future work are given section 7.3.

2. Principles

2.1. Anatomy / Physiology

2.1.1. General brain structure

In ancient Greece the heart was considered to be the place which accommodates ratio and soul, while the brain was regarded as a cooling device for the blood. In the understanding of today, 'all behaviour is the result of brain functions' (Kandel 2000), which includes motor action, e.g., typing, cognitive processes, e.g., forming sentences. 'The building blocks of the brain are the nerve cells, usually referred to as neurons. All nervous systems consist of distinct cells called neurons, which are specialized for nervous functions and which produce prolongations (axons) and branches (dendrites)' (Basar 1998). Four types of neurons can be distinguished. There are motoneurons, secretory cells, sensory neurons and interneurons. Central for the visual system are sensory neurons in form of photoreceptor cells in the retina of the eye and interneurons receiving and propagating input in the further visual pathway (section 2.1.2.1). On the macroscopic scale, the brain is protected by the skull, is surrounded by cerebrospinal fluid and protective membranes and consists of 5 main components: spinal cord, brain stem, cerebellum (little brain), interbrain (diencephalon), and cerebrum (telencephalon).

The *brain stem* is the evolutionary oldest part and is in control of essential systems such as the cardiovascular system and the respiration. It is subdivided into the medulla oblongata, the pons and the midbrain (see Figure 2.1). At its lower end it merges with the spinal cord whereas the upper end connects to the diencephalon. This position allows the brain stem to serve as a two-way relay for information travelling from the body to the cerebrum or cerebellum, e.g., pain. The main aspect of the *cerebellum* is the control of movement, motor learning and control of some cognitive functions. The *diencephalon* is located above (dorsal to) the brain stem and can be subdivided into thalamus, hypothalamus and further subdivisions (e.g., metathalamus and epithalamus) according to functional characteristics. It comprises centres for olfactory, auditory and optic nerves and connections to various cortical areas of the cerebrum. An example is the second cranial nerve (optical nerve), which emerges from the diencephalon connecting the retina with the lateral geniculate nucleus (LGN) in the thalamus. The thalamus thus serves as a relay and pre-processing station between the eyes and the visual cortex (see section 2.1.2 for more detail).

The *cerebrum* consists of two symmetric hemispheres, which are connected by three structures, e.g., corpus callosum (see Figure 2.1). The main components in the cerebrum are the white matter (substantia alba, main mass) and the grey matter (substantia grisea, surface). For the most part, the white matter is formed by axons and is the main mass in the interior of the cerebrum. Thus, its major role is the conduction of sensory input and interconnection of different centres of the brain.
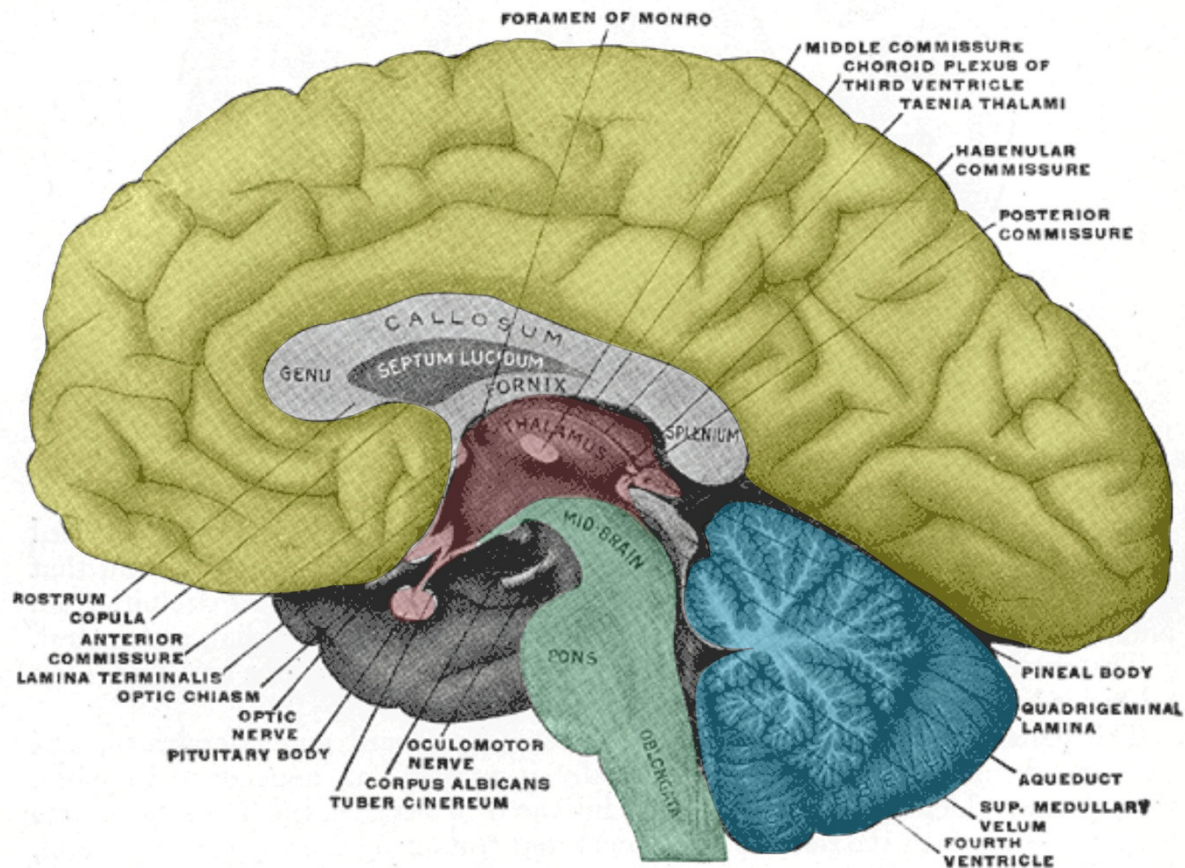
Figure 2.1: Brain structure according to table 715 in Gray's anatomy. View of the human brain sectioned at the midsagittal (median sagittal) plane (Source: Gray 1918).

In contrast, the grey matter is (mainly) located on the surface of the cerebrum, where it forms the cortex (cortex cerebri). It consists of neurons in large number and high density. To accommodate the number of cells, the surface is not smooth/planar, but enlarged by several sulci (fissures) and gyri (hills) of different depth/height and length. Along the major gyri, the cortex can be subdivided into five lobes. The frontal, parietal, temporal and the occipital lobe form the outer surface hiding the insular cortex. Each of the lobes comprises functionally specific areas. Some areas process primary sensory input (sensory areas) while other areas associate and coordinate the sensory input with further regions in the brain (association areas) or control voluntary movements (motor areas). An example for an area processing primary sensory input is the visual cortex in the occipital lobe.

For example, the primary visual cortex reveals a layered structure which is numbered from the outside (1) to the inside (6, towards the white matter), where layer 4 is subdivided in several further layers. Each of the layers possesses a characteristic way of synaptic wiring. The cells of the various layers also reveal interconnections. They are organized so that neurons which process input from a receptive field are organized in columns. The typical sizes range between 30 and 100µm in diameter and 2mm in thickness (Kandel 2000). Hence the functional columns are always oriented perpendicular to the folded brain surface.

4

In 1909 Korbinian Brodmann published the first description of the cellular architecture of the cortex (Brodmann 1909). In his work he subdivided the human brain into 52 areas based on the histological structure of the grey matter. His map assigns a specific number to a distinct area and is still used (and improved) today. For example Brodmann area 17 (see Figure 2.2) is the primary visual cortex (also V1) and receives direct input from the lateral geniculate nucleus (LGN).
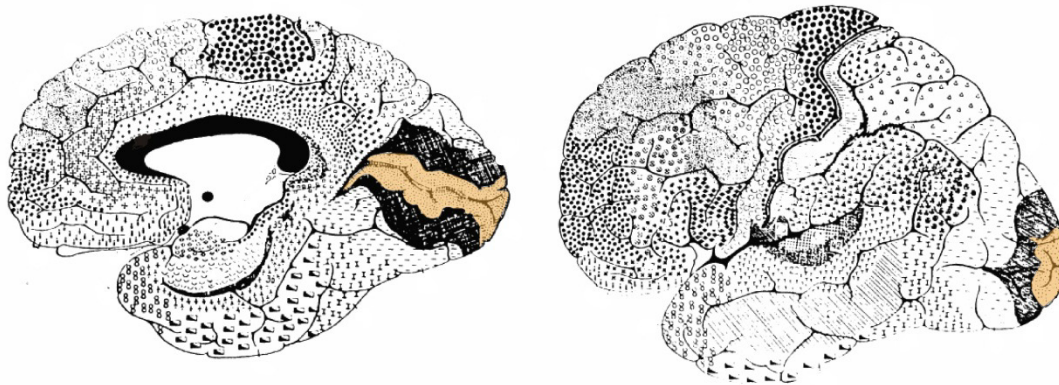

Figure 2.2: Brodmann area 17, the primary visual cortex, is highlighted in yellow. Left hand side shows the midsagital view, the right hand side shows the cortex view. Gyri and fissures separate the distinct functional areas (Source: Brodmann 1909, Kandel 2000).

2.1.2. Pathways in the central visual system

2.1.2.1. General description

The retina receives light as the (adequate) stimulus and transduces it via photoreceptors (rods and cones) and adjunct inter-neurons into nerve impulses, which are conducted by ganglion cells in the optic nerve. There exist (mainly) two main types of ganglion cells: the M-cells (M stands for magni, large) and the P-cells (P stands for parvi, small). M-cells are ganglion cells with large receptive fields and therefore indentify 'large' objects and respond rapidly to stimulus changes. P-cells possess only a small receptive field and are mainly involved in the processing of colour and form of objects. The oscillations produced by the retina are not synchronous, therefore they do not produce a (large) measureable field (Kandel 2000). The impulses are conducted along the optic nerve. However, in terms of position and wiring, the retinas have to be discriminated into temporal and nasal hemiretinae (see blue and red part of the optic tract in Figure 2.3). Although only one nerve cord exits the eyeball, the wiring distinction becomes apparent at the optic chiasm. Here the nerve cords are split and crossed over so that the nerve cords from nasal hemiretinas and the respective contralateral temporal hemiretina are merged. For example, the nerve cords from the left temporal hemiretina and the right nasal hemiretina are merged and enter the thalamus on the left side. Thus the complete visual information obtained by one hemifield of vision (assuming both foveae fixate the same point) is conducted in only one nerve cord.
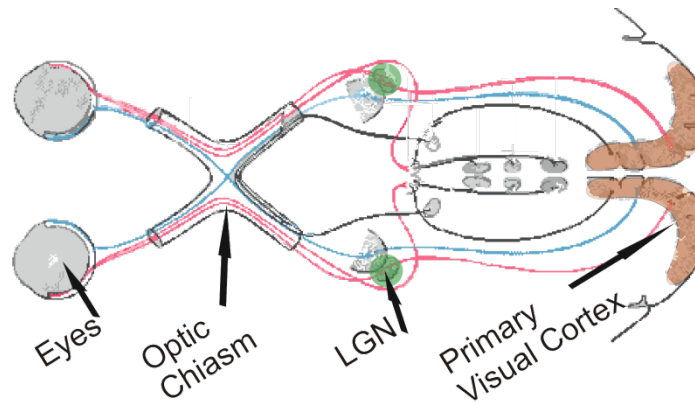
Figure 2.3: Anatomy Table 722 (rotated and coloured), according to (Gray 1918) shows the general structure of the central visual system including the optic chiasm, the LGN (highlighted in green) and the primary visual cortex (highlighted in orange). The blue and red lines point out the temporal (red) and nasal (blue) hemiretinae and the according nerve tracts.

90% of the optic nerve fibres terminate in the LGN in the thalamus. The nerve cord with nerves from the left temporal hemiratina and the right nasal hemiretina enter the left LGN, while the right side is constructed accordingly. The LGN is a relay station made up from six concentric semicircular layers. Each layer receives input from one eye only. That is, the layers 1, 4 and 6 of the left LGN receive input from the right nasal hemiretina and the layers 2, 3 and 5 receive input from the left temporal hemiretina. Thus, the optical information of the hemifields of vision remains separated. Furthermore, the M-cells are processed separately from the P-cells in layers 1 and 2. This segregation continues in the conduction of the visual information, since the M- and P-cells end in different terminals in the primary visual cortex (V1).

In the visual system, the information flows from the retina to thalamus and is relayed from there to the occipital lobe. The wiring of this sensory system, the second cranial nerve, has over one million nerve fibres (Kandel 2000). In contrast, the auditory system is a compound of only 30000 nerve fibres.

2.1.2.2. The role and the properties of the LGN

The function of the LGN is not well understood yet. Only 10-20% of the presynaptic connections that enter the LGN have their origin in the retina, the rest originates in several structures in the brain and are largely feedback connections (Kandel 2000). For example, the primary visual cortex sends modulating feedback input back to the LGN and could thus have an influence on the processing of visual information. Cortico-thalamic feedback projections from V1 comprise approximately 30% of the modulatory input to the LGN (Kastner 2006). Physiological properties of different pathways obtained from animal studies are presented in section 2.1.2.4

2.1.2.3.   The input and output of V1

Like the entire cortex, the V1 consists of 6 anatomically different layers numbered from 1 (outer surface) to 6 (inside). Layer 4 is further subdivided in layers 4A (towards layer 1), 4B, 4Cα and 4Cβ (towards layer 6). Most afferent fibres from the LGN end in layer 4. The input from the M- pathways ends in layer 4Cα, while the P-pathways terminate in 4Cβ. From there they are wired via layers 4B, 2 and 3 to either other cortical areas or via layer 5 to layer 6. Cells in layer 6 then project to both 4C-layers, thus forming a loop. Furthermore layer 6 projects back to the LGN forming another loop, which modulates the thalamic relay (Sherman 2001). The connecting neurons between the different layers beginning at the input in 4C to the various outputs are organized in columns around the input terminal. The columns are approximately 2mm high and 30μm to 100μm wide. Figure 2.4 shows the simplified feedback network of the M-pathway discussed above, excluding connections to other visual cortices.
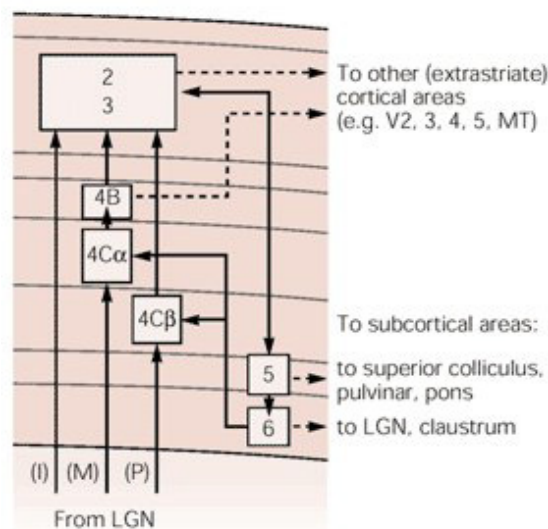

Figure 2.4: A (simplified) network of the information flow in the different layers in the primary visual cortex (adapted from: Lund 1988 and Kandel 2000). The flow of information from the M-pathway forms a loop including layers 4Cα, 4B, 3, 2, 5 and 6. Layer 6 closes the loop to layer 4Cα and connects to the LGN. The information flow is bidirectional for the connection of layers 2, 3 to layer 5. Information is relayed to other cortical areas.

Of course the processing of visual stimuli is not limited to the V1, but the V1 has strong feedforward connections to the secondary (associative) visual cortex V2 (Brodmann area 18), which in turn has both, feedback connections to the V1 and forward connections to the other visual cortices. Each visual cortex has a specific task, e.g., the detection of movement (Kandel 2000). Furthermore a difference in the susceptibility to flicker (section 2.1.3.2) stimulation between the various participants in visual pathway(s) becomes apparent.

7

2.1.2.4. *Physiology of the pathways gained from animal studies*

The neuronal structures of the optical tract are very similar among primates. The (visual) cortex of both, monkeys and humans is composed of 6 layers and therefore very similar. Results of experiments performed on monkeys are therefore to some extent applicable to humans. One experiment, which was conducted with monkeys, examined the contribution of M- and P-cells in the reception of luminance contrasts (Merigan and Maunsell 1993). The stimulus was a stationary grating with darker and brighter bars of variable luminance contrast and of low spatial frequency presented in a flash mode. Additionally, the lengths of the on-off cycles was varied and ranged from milliseconds up to several seconds. Then, in the monkey subjects either the M-pathways or P-pathways were disabled. At low flash frequencies (~1Hz) the P-pathways show higher contrast sensitivity than the M-pathways cells. The opposite is true at a flash frequency around 10Hz, then the M-pathways show 'considerably' higher contrast sensitivity than the P-pathways. The peak contrast sensitivity of the M-pathways at 10Hz is even higher than the sensitivity of the P-pathways at the peak at around 1Hz. At the corresponding peaks, the lesioned pathways show no difference to the control monkeys (Merigan and Maunsell 1993). According to these results, the M-pathways show the highest temporal resolution and reach the peak sensitivity for stimulation with a flashed pattern with a flashing-frequency at around 10Hz. However, this does not reveal which structure in the M-pathway increases the responses to the 10Hz steady state stimulation.

2.1.3. **Electrical activity of neural populations in the visual system**

2.1.3.1. *Spontaneous resting alpha generation*

The most prominent brain rhythm is the alpha rhythm. A human subject at rest with closed eyes mainly produces sinusoidal-like oscillations in a range from 8Hz to 13Hz (Basar 1998), whereas each individual has a specific individual alpha frequency. However some subjects with a normally functioning brain do not reveal alpha activity. The highest amplitudes occur over the occipital and parietal lobes; again the spatial distribution varies across the individuals.

The physiological mechanisms generating alpha rhythm are unclear. An initial hypothesis emphasized the pace making role of the thalamus (Andersen and Andersson 1968), but studies with dogs (Lopes da Silva et al. 1978) reported that the alpha rhythm is of a cortical origin, with large layer 5 pyramidal neurons acting as pacemakers. Conversely, alpha waves with identical characteristics can be recorded from the visual cortex and the lateral geniculate nucleus (Lopes da Silva et al. 1973).

Thalamic neurons, when measured in vitro (i.e.: without synaptic transmission), exhibit the tendency of generating intrinsic oscillations in a range from 6-10Hz (Jahnsen et al. 1984a, b). These neurons belong to different networks. Hence, it is likely that they play a role in the

generation of the rhythmic behavior of their network. However, the rhythmic activity of the respective network cannot be explained sufficiently by the intrinsic oscillators alone (Lopes da Silva 1991b).

In the thalamus, there are 3 types of neurons that can be differentiated in the network(s) underlying the generation of alpha activity. The first type are the reticular thalamic neurons (RE) located in the in the reticular nucleus of the thalamus, the second type are thalamo-cortical neurons (TCR) projecting to the cortex and giving collaterals to the first type, and the third type is the group of *local-circuit* interneurons (IN) (Lopes da Silva 1991a). TCR neurons can show two different behaviors depending on the resting membrane potential of the neurons. On one hand they can depolarize according to an input and thus act as relays of information, e.g., from the retina), or on the other hand they can produce bursts in a rhythmic fashion (Steriade et al. 1988; Lopes da Silva 1991a). The axons of the RE neurons mainly connect synaptically to the TCR neurons (Lopes da Silva 1991b) and also oscillate more readily then the TCR neurons.

Together the RE and TCR neurons form an oscillatory circuitry (Steriade et al. 1990), where the RE neurons inhibit the TCR neurons, 'which produce rebound excitation which returns to the RE neurons' (Steriade et al. 1988). The TCR neurons are linked to second oscillatory system via pyramidal cells in the cortex, which -while returning to thalamus- give collaterals to the RE neurons (Steriade et al. 1990). There is yet a third oscillatory circuit including the IN neurons. The IN neurons receive excitatory input from afferent fibers and are connected in an inhibitory fashion to the TCR neurons, yet the IN neurons also receive inhibitory from the RE group (Lopes da Silva 1991b) and excitatory/modulatory input from (cortex) layer 6 neurons, which in turn are connected to the TCR neurons (Sherman 2009). In addition to the 3 presented networks, the thalamo-cortical neurons (TCR) receive excitatory input from the brainstem, which inhibits RE neurons (Steriade 2000). In vivo experiments on cats show that relay-mode TCR neuron show cyclic suppression of firing, which is centered around the negative peak of the alpha oscillation for one population and centered around the positive peak for the second population. The allocation to the negative or to the positive group is determined by the inhibiting interneurons. This is supposed to lead to temporal framing of action potentials relative to the alpha oscillation (Lörincz et al. 2009).

In vitro preparations have further established that cortical neurons can oscillate intrinsically (Steriade et al. 1990; Connors and Amitai 1997). When recorded with micro-electrodes, alpha oscillations are usually composed of a variety of oscillations with slightly different properties, which seem to be generated by a large number of small areas, so-called epicentres (Lopes da Silva et al. 1978). Furthermore, (Lopes da Silva et al. 1991a; Flint and Connors 1996) have tested the role of cortical layer 5 pyramidal cells in alpha pacemaking, and in augmenting response (Castro-Alamancos and Connors 1996), a resonance-like phenomenon observed on repetitive stimulation at 10 Hz. The intracortical coherences are larger than the thalamo-cortical coherences (Lopes da Silva et al. 1980), while the LGN neurons show smaller influence on the intracortical coherences than the pulvinar.

These findings have motivated computational models to incorporate an alpha pacemaker at the level of layer 5 (Karameh et al. 2006). However, 10 Hz oscillations, which do not show the classic visual alpha reactivity, are also found in other areas such as auditory (Lehtelä et al. 1997), and motor (Castro-Alamancos and Tawara-Hirata 2006) cortices. (Speckmann et al. 2004) state that the electrical activity measured by the electroencephalogram (EEG) is generated by pyramidal neurons in layer 5.

The EEG-scalp electrodes record thus a complex mixture of (cortical) sources. However, only fields generated by a sufficient number (see section 2.2.1) of synchronous neurons can be measured on the scalp. This implies that the sufficient number of neurons forms a patch on the cortex with a size of up to the centimetre scale. In order to achieve sufficient synchronous activity, the patches have to be coordinated (Nunez et. al 2001), for example through adequate stimulation in a repetitive manner.

2.1.3.2. *Responses elicited by adequate stimulation*

Besides eliciting spontaneous activity, which is uncorrelated to any form of stimulation, the brain creates measurable response activity to adequate stimulation. The response can either be an evoked potential (EP) occurring temporally/phase-locked to the stimulus or an induced potential (IP) occurring after a stimulation without temporal/phase locking. For example, induced gamma activity consists of oscillatory bursts, which do not have an exact temporal relationship to the stimulus (Tallon-Baudry and Bertrand 1999).

By contrast, the EP is the most notable sensory stimulation and always occurs at a fixed time after the stimulus. The stimulation can be electrical, acoustical or tactile; in the following the visual evoked potential (VEP) is described. A VEP can be elicited by two major categories of stimulation, namely luminance or pattern. A pattern-based stimulation is usually performed with a checkerboard pattern. It is viable to present the stimulus either by reversing the pattern or using an on(set)/off(set) mode (Odom et al. 2004). The luminance stimulation is usually presented with light flashes, where usually the whole visual field is stimulated (whole field stimulation).

Empirical evidence shows that LGN cells can synchronize their responses in a stimulus-dependent way (Sillito et al. 1994). The evidence indicates that synchronous LGN responses in turn are particularly effective in driving cortical cells (Alonso et al. 1996). This suggests the possibility that the oscillatory patterning of visual responses in the retina and the LGN (Castelo-Branco et al. 1998) contributes to the oscillatory modulation and synchronization of cortical responses. 'However, retinal and cortical oscillations differ in frequency and time course, making it unlikely that synchronization phenomena in the cortex simply reflect retinal interactions' (Ito et al. 1994; Neuenschwander et al. 1996).

In experiments, the stimulating repetitive light flashes (or flickering light) typically are presented at a range of frequencies, e.g., (Hermann 2001) stimulated subjects with flashes

between 1Hz and 100Hz. The activity of the neurons in the visual cortex is synchronized to the stimulus, thus the response frequency is locked to the (neuronal-) stimulation frequency: flickering light entrains (alpha) activity in the cortex. Due to the mode of stimuli presentation this type of evoked potential is referred to as steady state visual evoked potential (SSVEP) or photic driving. Although this effect is used in clinical routine as a measure for the functional flexibility of the cortex only about 50 to 80% of healthy subjects (Lazarev et al. 2001) show evaluable results.

An animal flicker experiment studied the whole-field stimulation of the cat visual cortex (Rager and Singer 1998). In this experiment, responses stabilized not immediately after stimulus onset but after continuous flickering of 300ms. The maximal response magnitude was elicited at a stimulation frequency of 25Hz at the fundamental response frequency. However, when stimulated with 12Hz, the 1st harmonic response is approximately 10 times stronger than the fundamental response.

The role of the thalamus is the link between the sensor (here: the retina) and various areas in the cortex, which are occupied in the processing of visual information. The flow of information does occur (at least partially) in the above described networks (see section 2.1.3.1). The work of (Sherman 2007) describes loops between different nuclei in the thalamus and various cortices. In this model, information is relayed (and modulated) via the LGN into a first cortical area. Information is fed back to the LGN (to TCR + RE neurons) but also serves as input for other thalamic nuclei, e.g. pulvinar. From there information is sent to higher visual cortices, from where the information is again fed back to the thalamus. There exists a clear differentiation between two classes of circuitry in the thalamus and the cortices, where class 1 relays information, while class 2 modulates (Sherman 2012). In the model mentioned above, the class 1 circuit guides the information stream on the way to the various stations in the thalamus and the cortex. Class 2 circuitry is responsible for the feedback loops from the cortex modulating the thalamus. It is yet unclear how much of the visual information is relayed via corto-thalmo-cortical paths compared to corto-cortical paths (Sherman 2009; Sherman 2012).

2.1.3.3.   Alpha entrainment/Repetitive visual stimulation

It is well known that stimulation by repetitive light flashes yields a frequency-locking between the alpha frequency and the stimulation frequency. Neurons in the human visual cortex synchronize their firing rate to the stimulation frequency of flickering light (Silberstein 1995). The resulting entrainment of the alpha activity in the electroencephalogram (EEG) appears in the changes of the alpha frequency toward the stimulation frequency (Rager 1998; Herrmann 2001). Clinically, this effect is called photic driving and serves as an indicator of the functional flexibility of the cortex and as an activation method in clinical practice e. g. in epilepsy, schizophrenia or other neuropsychiatric diseases (Jin et al. 1997; Takahashi et al. 1998; Lazarev et al. 2006).

A fundamental examination of the photic driving effect in the human EEG is given by (Herrmann 2001) by stimulating from 1 to 100 Hz in 1-Hz-steps. (Miranda de Sa and Infantosi 2005) show that stimulations close to the alpha peak were most effective. Photic driving in the EEG and the magnetoencephalogram (MEG) was first quantified by (Kalitzin et al. 2002) and (Parra et al. 2003).

Topographic effects of encephalographic photic driving effects in the case of children and adolescents are described by (Lazarev, Infantosi et al. 2004), for patients with migraine by (de Tommaso et al. 2003), and for patients with schizophrenia by (Jin et al. 1998).

In experiments of repetitive visual stimulation by photic pulses the elicited responses show interhemispheric phase differences. (Kawaguchi et al. 1993) focused on the phase differences between bilateral homologous loci. The examined (oscillatory) sources are located in the occipital areas of each hemisphere. In case of photic driving with a constant frequency, interhemispheric phase differences decrease for stimulation frequencies close to 'EEG frequencies' (Kawaguchi et al. 1993; interpreted in this thesis as the individual alpha frequency). However, for other stimulation frequencies the estimated phase differences are larger. Furthermore it is discovered that the phase differences fluctuate throughout the duration of a stimulation sequence (15 sec). It must be noted that these results are purely based on the comparison of single electrodes, like for example the pair O1-O2, and not on source analysis, e.g., dipoles.

In 2006 (Schwab et al. 2006) perform for the first time a photic driving experiment, which simultaneously records EEG and MEG with a high density of stimulation frequencies which are adapted to the individual alpha rhythm of each volunteer. They showed that the alpha peak in the power spectra is significantly elevated when stimulating at or close to the individual alpha frequency of the volunteer (~0.9 - 1.1*alpha). A fixed response frequency (plateau) in the EEG as well as MEG recordings is obtained for all stimulation frequencies close to the individual alpha frequency. A similar response could be shown for stimulation frequencies around half the individual alpha (~0.45 - 0.55*alpha). These findings support the hypothesis that the functional basis for this phenomenon is formed by a coupled system of non-linear neural oscillators with an individual resonance frequency. A pure linear system would respond with high mean amplitudes around the resonance frequency. The fixed resonance plateau matching the individual alpha frequency indicates nonlinear behaviour. Additionally, the presence of harmonic and subharmonic resonance peaks leads to the conclusion that the involved oscillators form a nonlinearly coupled system. This interpretation contributes to the findings of (Stam et al. 1999) suggesting that the human alpha rhythm behaves in a nonlinear fashion.

As described in section 2.1.3.1, the visual system contains oscillating elements (TCR, RE neurons and associated networks), which oscillated intrinsically and thus are self-sustained. An external stimulator connected to the oscillating elements can perturb the intrinsic oscillation. The oscillating elements may synchronize to periodic perturbation, e.g., light flashes, and synchronize to the external driver. The synchronization implies a fixed phase

relation between the driver and the oscillator. In a model suggested by (Thut et al. 2011) a population of self-sustained oscillators represents a group of neurons, which become synchronized by an external repetitive stimulus. The focus of this simulation lies on a stimulation frequency identical to the natural frequency of the neural assembly. The authors illustrate 'two main characteristics of the entrainment at population level: (a) adjustment of phase of the underlying oscillation to the periodic force, and (b) increase in amplitude' (Thut 2011), where the amplitude is building up to a maximum over a number of stimuli. For continuing stimulation the response amplitude remains on the maximal level. The explanation provided is, that the phases of the oscillators align. Entrainment and locking are synonymous under these conditions (Pikovsky 2001; Thut 2011). In an experiment with one stimulation frequency identical to the natural frequency of the underlying neural population, the amplitude increase over stimuli and the phase adjustment must be detectable.

2.2. Electroencephalography (EEG) and Magnetoencephalography (MEG)

2.2.1. General properties

The activity in the EEG is usually subdivided into distinct rhythms which stem from different areas in the brain and are thus caused by different processes in the brain. Besides the already described alpha rhythm in the range from 8Hz to 13Hz further distinct brain oscillation band are found in EEG and MEG recordings. The next higher frequent rhythm is the Beta-activity ranging from 14Hz to 30Hz. It is associated with the waking state of human brains (Kandel 2000). The (cortical) Theta (3Hz to 8Hz) and Delta (0.5Hz to 3.5Hz) waves appear in some (but not all) sleep states but rarely occur in the waking state of adult humans. The Gamma band ranges from ~30Hz to 80Hz and can be found all over the brain. Experiments show that they are correlated with cognitive functions. Thus, the oscillations allow for a binding or association of the features (Herrmann and Demiralp 2005).

Typically the oscillation frequency of the recording differs depending on time, recording places and different states of awareness. Conventionally, the recorded oscillations range from 0.5Hz to over 100Hz (Basar 1998).

The EEG and the MEG record the magnitude of the electrical or magnetic fields by means of adequate sensors at a pre-set sampling rate. Moreover, the electrical and magnetic fields of one source are mutually orthogonal (Hämäläinen et al. 1993). The magnitude of the measureable activity generated in the cortical neurons depends on the number of the synchronously active (coherent) neuronal columns. There are approximately 10^6 cells and 10^{10} synapses (Nunez 1995) in a column (see section 2.1.1) of 3mm diameter. (Abeles 1982) states that 'at this spatial scale, cortical tissue appears to demonstrate homogeneous statistical properties'. However, (Lopes da Silva 2010) concludes from the work of (Murakami 2006) and (Hämäläinen et al. 1993), that 'an assembly of 50000 synchronously active cells would generate a field [...], which corresponds precisely to the value measurable

from the human cortex using the MEG'. Thus, a minimum of 50000 (synchronous) cells in a column of neurons basically form a dipolar structure, which produces detectable activity. Excitation by a sufficient stimulus changes the polarization characteristics of a neuronal column, 'impressing a space averaged synaptic and action potential current' (Nunez 1995) or primary current. In order to compensate for this shift of charge carrying ions, secondary (passive) currents in the surrounding medium have to complete the loop. Hence, the currents produce the electric potentials on the scalp and also the magnetic fields measured by the MEG (see section 2.2.3).

2.2.2. EEG

The EEG measures the electrical potentials on the scalp generated by electrical brain activity via a set of electrodes. The electric potentials produced in the cortex are influenced by the highly conductive cerebrospinal fluid and three membranes and the skull. The potentials generated in the cortex are spatially diffused. Additionally, the skull is a poor electrical conductor with an average electrical resistivity around 80 times that of brain or scalp tissue (Rush and Driscoll 1968; Nunez 1981). The size of the electrodes has only a small effect on scalp potentials, since they are already spatially filtered. Besides the properties of the surrounding tissues, also the orientation of the column influences the magnitude of the measured potential. A typical value for the amplitude of the recordings lies between 10µV and 200µV.
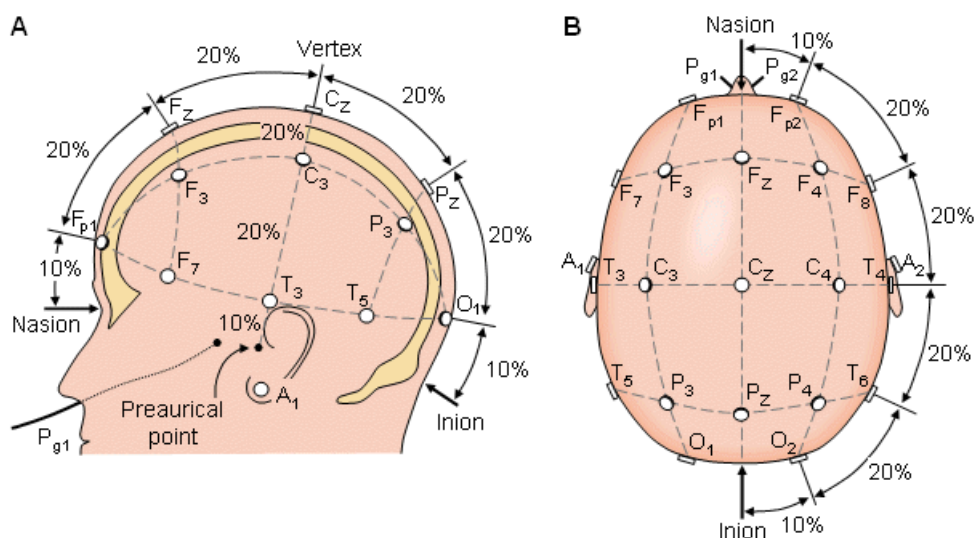
Figure 2.5: The 10/20 system showing the standard placing of electrodes and the according names (Source: BEMFI, according to: Jasper 1958). The anatomical references nasion, inion and the preaurical point are shown.

In clinical practice, the EEG is usually recorded using silver–silver chloride electrodes, which are placed on the scalp in a standardized and reproducible arrangement. The most common setup is the so called 10/20 lead system (Jasper 1958, see Figure 2.5). The name is derived from the spacing of the electrodes. The electrodes are spaced at distances of either 10% or

20% of the whole distance between the following anatomical landmarks: Nasion, Inion, Preaurical point. (see Figure 2.5). Electrodes are labelled according to their position in the frontal, parietal, temporal, or occipital region.

The spacing based on 10% and 20% can be enhanced to, e.g., a 10/10 system. Here the same landmarks count, just the distance between them is subdivided into stretches of 10%. Also mixed setups like a standard 10/20 with an enhancement by 10/10 system over a specific area can be arranged.

Potentials cannot be recorded by a single electrode alone. Therefore each electrode in any given system is recorded to a reference. One way to achieve this is a setup with the misleading name monopolar montage or referential montage. In the monopolar montage all electrodes are wired to a common (supposedly) inactive electrode, which is usually placed at a mastoid. Furthermore, there is the bipolar montage, in which active electrodes are connected to other single electrically active electrodes. Also the averaged signal calculated from all electrodes can be used as reference. Basically the mentioned montages can be calculated from the monopolar montage.

2.2.3. MEG

The basic process of the generation of the electric and magnetic fields in the brain is described in section 2.2.1. The magnitude of the measured magnetic field does depend on the orientation of the generating source. While the EEG is most sensitive to radial sources, the MEG is recorded best for sources of tangential orientation. In this respect, the MEG and EEG supplement each other, since one method can detect sources that the other method cannot find (Cuffin et al. 1979). Sources measured by the MEG are (mainly) of tangential origin and thus are located in the fissures of the brain (Hämäläinen et al. 1993). The tissues surrounding the brain do not compromise the magnetic fields as much as the electric fields.

The magnetic signals generated by the brain are usually in the range of 50-500fT and thus are considerably smaller than the magnetic field of the earth (~50μT), and other sources of magnetic noise, e.g. power lines. The fields are measured by means of a superconducting device (SQUID) and special coils in a magnetically shielded room. The coils (gradiometer) are constructed such that the external fields (noise) are hugely reduced in comparison to the desired signal by the correct geometrical design. The gradiometer is made of two coils of identical area, which are connected in series: one pickup coil (close to the source) and a compensation coil. Since they are coiled in the opposing senses, currents, which are caused by spatially uniform magnetic fields (such as the magnetic field of the earth, and other distant sources), cancel each other out. This setup is sensitive to fields, which are inhomogeneous (fields created in the cortex) and vary overt time (Hämäläinen et al. 1993). Typical MEG sensor arrangements are hexagonal patterns on a dish or closely spaced creating a helmet-like geometry.

2.3. **Matching Pursuit (MP)**

2.3.1. **Introduction**

It is estimated that there are approximately 10^{10} neurons and thus 10^{14} synapses in the cortex (Hämäläinen et al. 1993) which are active if stimuli are processed. As for example the EEG is sensitive to groups of 50000 (see section 2.2.1) neurons, electrical activity stemming from a large amount of sources is measured. Only the analysed activity is to be considered as signal, the rest as noise. Additional noise signals are for example of biological origin, as for example the electric potentials created by the heart, or of technical origin, as for example power lines, cell phones or even fluorescent lamps. It is thus of major importance to tell noise and signal apart. Filters attenuate certain frequencies in the signal, for example a band stop filters can minimize the 50/60Hz power line artefact. The approach of filtering data is limited if the noise and the signal contain (almost) similar frequency components.

There are several methods available, which estimate data by operators. Setting thresholds to estimators, as for example wavelets, can suppress additive noise while still preserving the signal (Mallat 1998). Furthermore, these estimators can describe the signal with few components only, yielding a sparse representation of the signal. For example (Gratkowski et al. 2006) state that the 'MP algorithm was found suitable for time-frequency filtering'. Additionally, they conclude that 'the description of an analyzed signal created by the atoms localized in time-frequency space allows the separation of the signal components that are of interest.' Based on these findings, Matching Pursuit is used to estimate a sparse yet concise representation of the signal by components of interest. In section 4.2 the development of a MP-based source localization technique is described, where besides the time and frequency components also spatial attributes of the sources (location in the brain) are analyzed. In the subsequent section the mathematical basics (Mallat and Zhang 1993) of MP are presented.

2.3.2. **Formalism of Matching Pursuit**

The iterative MP-algorithm decomposes a (single-channel) time series $f(t)$ into an estimation of a sum of weighted Gabor atoms:

$$f(t) = \sum_{j=1}^{J} a_j * g_{\gamma_j}(t) , \qquad\qquad (2.1)$$

where a_j represents the weights and $g_{\gamma_j}(t)$ are atoms, with γ_j being the index of the chosen atom, ranging from $j = 1 \dots J$, where J is the amount of atoms in the approximation of the signal.

Gabor atoms are constructed from a (Gaussian) window function, which is modulated in the real valued case by a cosine function of a fixed frequency and a phase shift ϕ_{MP}.

Consequently, an atom is well localized in time and frequency; as an additional parameter, the window function can be scaled.

$$g_{(\gamma,\phi)}(t) = \frac{K_{(\gamma,\phi)}}{\sqrt{s}} * g\left(\frac{t-u}{s}\right) * cos(\xi t + \phi_{MP}), \tag{2.2}$$

where s is the scale, u stands for translation and ξ represents the modulation; $\gamma = (s, u, \xi)$; $K_{(\gamma,\phi)}$ is a normalization factor so that $\|g_{(\gamma,\phi)}(t)\| = 1$.

The MP method allows for a concise signal approximation by a small number of atoms. The algorithm chooses the atoms from a set called the dictionary. In theory, the dictionary can be composed of an infinite number of atoms. In practice the number of dictionary elements is limited, however high enough to preserve high redundancy. Thus, MP has a high amount of possible waveforms for describing features of a signal, but uses only a few in the final estimation. This is in contrast to the Fourier analysis, which works on an orthogonal basis, and thus needs many sinusoidal functions to approximate a signal.

A signal approximation by MP-atoms is calculated iteratively. In the first step, the algorithm correlates a given single channel data set with each atom in the dictionary. The atom with the highest correlation - and therefore the highest inner product with the signal - serves as the first approximation of the signal f. Subtracting the first atom from the signal yields the first residual $R^1 f$:

$$f = \langle f, g_{(\gamma,\phi)} \rangle g_{(\gamma,\phi)} + R^1 f \tag{2.3}$$

The algorithm repeats these two steps on the first residual $R^1 f$, producing the second atom and second residual $R^2 f$:

$$R^1 f = \langle R^1 f, g_{(\gamma,\phi)} \rangle g_{(\gamma,\phi)} + R^2 f \tag{2.4}$$

Or more general (k residual index):

$$R^k f = \langle R^k f, g_{(\gamma,\phi)} \rangle g_{(\gamma,\phi)} + R^{k+1} f \tag{2.5}$$

This recurs until a criterion, such as a predefined number of atoms or a predefined percentage of explained energy, is met. After l iterations the signal can be written as the linear combination of fl atoms plus a residual (Mallat and Zhang 1993). We call the set of l atoms the atom set.

$$f = \sum_{k=0}^{l-1} \langle R^k f, g_{(\gamma,\phi)} \rangle g_{(\gamma,\phi)} + R^l f \tag{2.6}$$

2.3.3. **Topographic Matching Pursuit (TMP)**

For the decomposition of the multi-channel EEG and MEG recordings (section 4.1) I apply an extension of the MP algorithm, which is suitable for multi-channel-analysis: the Topographic

Matching Pursuit (TMP) algorithm (Gratkowski et al. 2007; Gratkowski et al. 2008). TMP uses a standard MP-dictionary of Gabor atoms. The key difference between TMP and standard MP lies in the computation of the correlation: the TMP algorithm chooses the atom which has the highest simultaneous correlation in all channels. For each channel ch the TMP-atom $g_{(\gamma,\phi_{TMP,ch},\text{l})}(t)$ has a different phase $\phi_{TMP,ch}$ and amplitude, where the latter parameter is obtained from the inner product between atom-channel and data-channel, thus resulting in:

$$g_{(\gamma,\phi_{TMP,ch},\text{l})}(t) = \frac{K_{(\gamma,\phi_{TMP,ch})}}{\sqrt{s}} * g\left(\frac{t-u}{s}\right) * cos(\xi t + \phi_{TMP,ch}), \qquad (2.7)$$

Thus the channel-dependent phase parameter allows for a more precise signal approximation if the analysed signal has asynchronous channels. The left hand side of Figure 2.6 shows a measured signal. The right hand side of Figure 2.6 shows a real valued TMP-approximation by one atom.
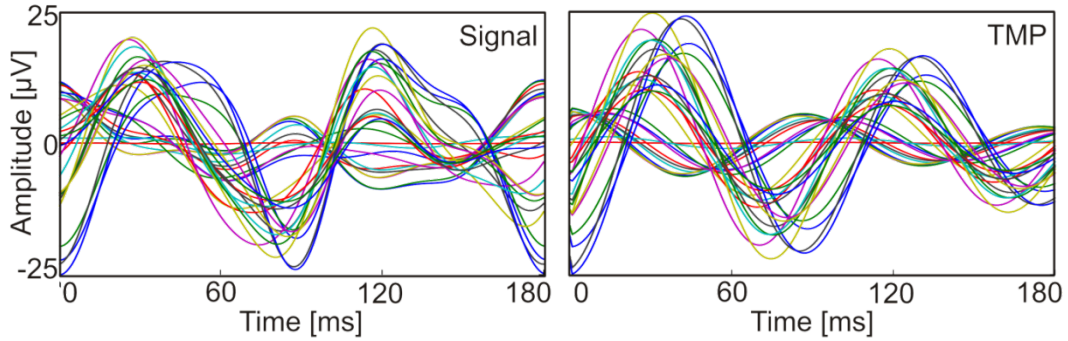
Figure 2.6: On the left: EEG-signal as obtained by the experiment described in section 3.1. On the right: the according approximation by the first TMP atom. The different EEG channels are represented by lines of different color. The signal is sampled at a rate of 1000 samples per second.

2.4. Source localization

2.4.1. Introduction

The general idea behind source localization is pinpointing the generator of measured activity. For the purpose of source localization based on EEG and MEG recordings, this translates into (noninvasively) finding the spatial coordinates of an active area, e.g., a columnar structure in the cortex, inside the brain or in the cortex.

The solution to this problem cannot be obtained in a straightforward manner. However, the sources generating a measured signal can be estimated, based on theoretical physical models of the source and of the head. The combination of sources and head model allows for the prediction of measurements by solving the *forward problem*. For the localisation of a source the task is the opposite, parameters of underlying sources are deduced from measurements. The solution to this so called *inverse problem* is not (necessarily) unique, even if an exact theoretical model of the underlying reality exists. A major problem is that there are many equivalent solutions to the problem. From the outside of a conductor it is

not possible to determine a unique solution for the internal current distribution (von Helmholtz 1853), so that the inverse problem is ill-posed. The determined solution is the best answer to the given problem. Thus the position of a generator estimated by an algorithm for a given EEG/MEG-signal is not necessarily the real location, but the one which provides the best solution to the problem. The localization also depends heavily on the noise in the signal.

2.4.2. **Source models**

The generating source of the measured activity can be modelled by either a focal source or a distributed source. The latter assumes that the main generators of electrical activity are a large number of dipolar sources distributed in a specific region (used in various methods, e.g., LORETA (Pascal-Marqui et al.1994)). Distributed source localization is often an under-determined problem, meaning that there are more parameters to be estimated then measured values. Focal source localization assumes that the mean activity of a not point like source can be approximated by a point like dipole which is defined by few parameters only. The parameters of a (current) dipole are optimized so that the residual energy (or a similar measure) between the measurement and computation is minimized.

The magnetic and electric properties of the generated fields by this current dipole are described by the Maxwell equations. The quasi-static approximation of the Maxwell equations apply, since the spectrum of the analysed signal in this work lies well below 100Hz, and the size of the head is in the scope of centimetres (Baillet et al. 2001). Any time-dependent components for the calculation of the electric field $\boldsymbol{E}$ and the magnetic field $\boldsymbol{B}$ ($\frac{\partial \boldsymbol{E}}{\partial t}$ and $\frac{\partial \boldsymbol{B}}{\partial t}$) can be ignored (Hämäläinen et al. 1993).

As stated in section 2.2.3, the cortical sources produce an electrical current density $\boldsymbol{J}_{loop}$, which can be divided into a primary current density $\boldsymbol{J}_p$ and a secondary volume current $\boldsymbol{J}_v$.

$$\boldsymbol{J}_{loop} = \boldsymbol{J}_p + \boldsymbol{J}_v \qquad (2.8)$$

The passive volume current is produced by the macroscopic electric field $\boldsymbol{E}$:

$$\boldsymbol{J}_v(\boldsymbol{r}') = \sigma(\boldsymbol{r}')\boldsymbol{E}(\boldsymbol{r}'), \qquad (2.9)$$

where σ is the electrical conductivity and $\boldsymbol{r}'$ a location in the conductive medium.

When applying quasi-stationary Maxwell equations, the electric field $\boldsymbol{E}$ is given by the negative gradient of a potential V (Baillet et al. 2001):

$$\boldsymbol{E} = -\nabla V. \qquad (2.10)$$

The total current flow J_{loop} can thus be expressed as:

$$J_{loop}(r') = J_p(r') - \sigma(r')\nabla V(r').$$ (2.11)

A focal source models the primary current J_p of an active cortical area concentrated in a single point and can be interpreted as current I, which is pumped from a sink at position r_{sink} to a source at position r_{source} (Hämäläinen et al. 1993, de Munck et al. 1988). This current is approximated by a current dipole Q, concentrating the primary current J_p to a single point:

$$J_p(r') = Q\delta(r' - r_Q),$$ (2.12)

where $\delta(r)$ is the Dirac delta function and r_Q is the position of the current dipole Q.

The current dipole Q can thus be defined by three location parameters, three direction parameters and the magnitude of the current I:

$$Q = I(r_{source} - r_{sink}).$$ (2.13)

2.4.3. Head models

Besides the source model, solving the forward problem furthermore requires modelling the volume in which this problem is to be solved. For, e.g., the EEG, a head model must be constructed based on electrical conductivities and geometrical properties. The resulting gain transfer matrix is usually called the lead field L and relates each source position to each sensor position. In simple cases the underlying geometry can be assumed as a sphere with one or multiple concentric shells of homogeneous conductors. Boundary element methods or finite element methods allow for anatomically more correct head models.

For the preparation of the present work several spherical head models with various conductivities and different amounts of concentric shell representing the brain, the skull and other compartments are used (Electric: Frank 1952; Rush and Driscoll 1968; Cuffin and Cohen 1979; Stok 1986; Magnetic: Sarvas 1987). Additionally different methods are applied for calculating the head models (Mosher et al. 1999; Berg and Scherg 1994; Sun 1997).

2.4.4. The forward problem

Measuring values can be simulated for all sensors, given a head model L and a current dipole Q defined by a position r_Q, a defined direction and strength. This set of simulated values (or predicted measurements) is the solution F_{Fwd} to the forward problem. The simulations F_{Fwd} can be either magnetic or electric solutions, depending on the type of lead field. Equation 2.14 puts this in a basic mathematical expression:

$$F_{Fwd} = L(r_Q)Q$$ (2.14)

2.4.5. The inverse problem

Electric potentials, registered at, e.g., the scalp, are generated by a large amount of possible dipolar sources. The activity of each of the columnar structures in the brain adds to the measurement besides the examined source Q and can be summed up in a noise matrix E. The noise matrix E also contains noise from other sources (e.g., biological, technical). Equation 2.15 extends Equation 2.15 to:

$$F_{meas} = L(r_Q)Q + E \qquad (2.15),$$

where F_{meas} is the measured activity. The challenge in solving the inverse problem is the determination of the most plausible position and direction of the examined source Q, given the noisy measurements.

An infinite number of dipoles and dipole configurations can serve as the estimated source of a measured potential. The amount of possible solutions can be reduced by introducing a priori information (or: constraints) such as the number of sources, symmetry of sources or limiting allowed source positions to a certain brain region. However, finding the best solution for the model with given a priori information (two mirrored dipoles with independent directions, see section 4.2.2) still presents a forward calculation of $\sim 10^{57}$ parameter combinations (given a certain parameter quantisation of position, direction etc.) and thus possible solutions. Due to the immense computational cost, not all parameter combinations are calculated.

The best parameter combination is obtained by an optimization routine. The basic strategy is calculating a forward solution for a set of start parameters (3 position parameters and 3 direction parameters including the magnitude namely the dipole moment). Then a new forward solution is calculated for one or numerous varied new parameter sets. The best solution thereof is estimated by a measure such as the root mean square error (RMSE, see Equation 2.16.

$$RMSE = \sqrt{\frac{\sum_{i=1}^{n} \sum_{si=1}^{w} \left(v_{i,si} - \bar{v}_i\right)^2}{n * w}}, \qquad (2.16)$$

where n is the amount of channels, i is the channel index, w is the amount of samples, si is the sample index and $\bar{v}_i$ is the mean value of the i-th channel.

Based on the RMSE, the best solution(s) are selected and are the basis for the next iteration of the optimizer. The process is repeated until the improvements gained by the variation of the parameters falls under a pre-set threshold. There are different strategies to the variation of the parameters and amounts of simultaneous forward solutions. Each strategy produces a best solution, which is not necessarily identical to the solutions obtained from other strategies. Typical strategies are, e.g., gradient descent, simplex method, simulated annealing, differential evolution and particle swarm.

3. Experiment and preprocessing of experimental data

3.1. Experiment

The algorithms developed in the scope of this thesis are tested by simulations and applied to experimental data. The experiment was conducted in 2005. The description shall be limited to the major facts.

The responses of 10 volunteers (mean age 28.8±5.81 years, 5 male; 5 female) to flicker stimulation are recorded simultaneously with MEG and EEG. The stimuli are delivered via optical fibers from 2 LEDs, 9 cm away from the closed eyes of the subjects. The 32-channel EEG (Synamp, Compumedics Neuroscan, El Paso, USA) is recorded with 10-20 system over the frontal region and with a 10-10 system over the occipital region. Additionally, a MEG with 31 channels (Philips, Hamburg, Germany) is recorded over the occipital region (Figure 3.1). Both EEG and MEG are recorded at a sampling rate of $Fr_{samp} = 1kHz$ and a hardware band pass filter between 0.1 and 300 Hz.
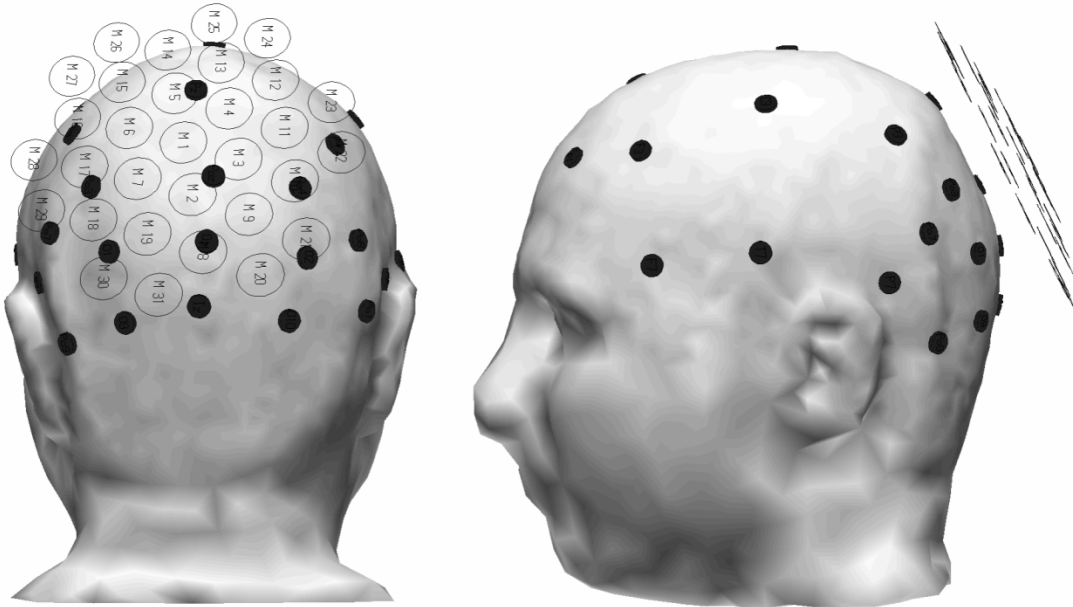
Figure 3.1: Positioning of electrodes (black dots, enhanced 10/20 system) and magnetic sensors over the occipital region (circles). Left: back view, right: side view (Source: Schwab et al. 2006).

Prior to the actual experiment, the resting alpha frequency of each subject is measured. The individual resting alpha frequencies range from 9.5 Hz to 11.8 Hz (Schwab et al. 2006). The volunteers are stimulated with light flashes of frequencies with a fixed ratio to the individual alpha frequency ranging from 0.4 to 1.6 times the individual alpha frequency (short: 0.4*alpha and 1.6*alpha). This stimulation elicits a steady state visually evoked potential (SSVEP). The following stimulation frequencies (expressed as multiples of the individual alpha frequency) are presented: 0.4, 0.45, 0.5, 0.55, 0.6, 0.7, 0.8, 0.9, 0.95, 1, 1.05, 1.1, 1.2,

1.4, and 1.6. (Please note that the stepping of the stimulation frequency around 0.5*alpha and 1*alpha is finer: ±0.05*alpha instead of 0.1*alpha.) Thus, the stimulation periods differ among the subjects for specific stimulation frequencies depending on their individual resting alpha frequencies. For example, the stimulation period for 0.4 times individual resting-alpha ranges from 212ms to 264ms and the stimulation period for 1.6*alpha from 52ms to 66ms. Therefore time points relative to the beginning of a stimulation period as a reference point could not be expressed in milliseconds but as multiple (<1) of the individual stimulation period $T_{ind,fr}$ (ind=individual; fr = stimulation frequency).

Each stimulation frequency is presented in a block of 20 trains. A resting period of 30 to 60 seconds exists between the stimulation blocks of different stimulation frequencies. Each train consists of 40 flicker periods (50% on and 50% off cycles for each frequency). Between two trains there is a resting period of 4 seconds (Figure 3.2).
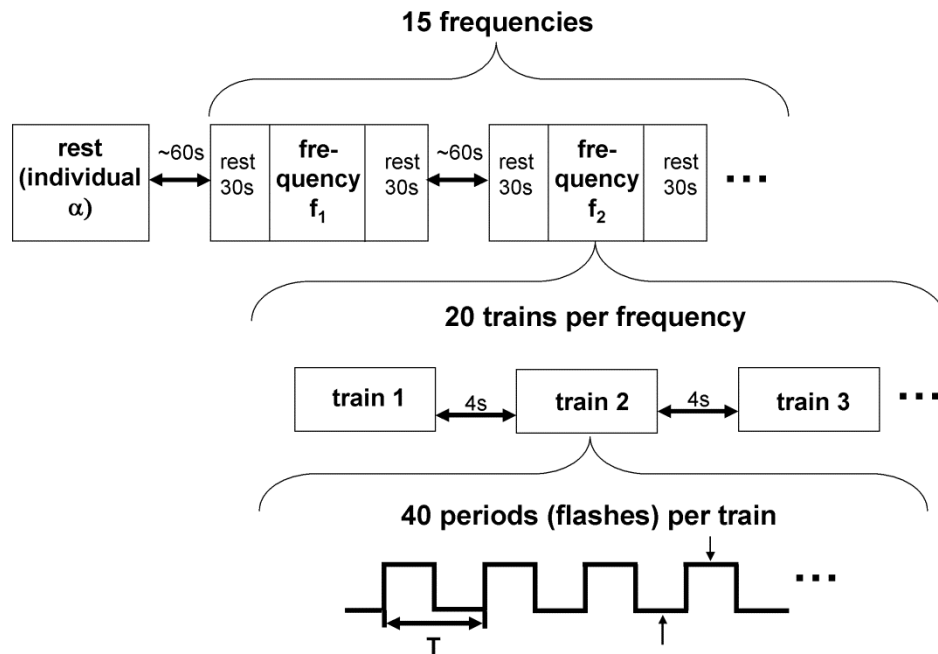
Figure 3.2: The stimulation pattern (Source: Schwab et al. 2006). Before the stimulation, the resting alpha is estimated. Based in each individuals resting alpha frequency the cycle duration T of each stimulation period is calculated. Each stimulation frequency is presented in 20 trains with 40 stimulation periods each. Between the trains and the stimulation blocks of different frequencies resting periods are included.

This experiment accomplishes for the first time a photic driving experiment which is (1) performed with a high density of stimulation frequencies, (2) close to the individual alpha rhythm of each volunteer and (3) records MEG and EEG simultaneously.

3.2. **Preprocessing**

The following preprocessing steps are within the scope of this work. The steps described here prepare the data for the further processing in section 4.

The EEG and MEG recordings of all subjects are again filtered by an identical digital filter in order to ensure identical treatment. Each train of each frequency is filtered separately. The lower (Fr_{CL}) and upper (Fr_{CH}) cut-off frequencies are determined by the highest and the lowest response frequencies expected. The lower margin is expected at the stimulation frequency of 0.4*alpha for the subject with the lowest individual alpha frequency (9.5Hz), the upper margin is expected at 1.6*alpha of the subject with the highest individual alpha frequency (11.8Hz). The limits are thus estimated for 3.8Hz up to 18.9Hz. Given that the response frequencies can deviate from the stimulation, the cut-off frequencies are chosen to Fr_{CL}= 2Hz and Fr_{CH}=20Hz (see Figure 3.3). Thus for preprocessing the data are filtered with a zero phase Butterworth band pass filter of order 4 with the given cut-off frequencies. The zero phase filtering is obtained by filtering in forward and reverse direction, applying a filter of half the desired order in each direction.
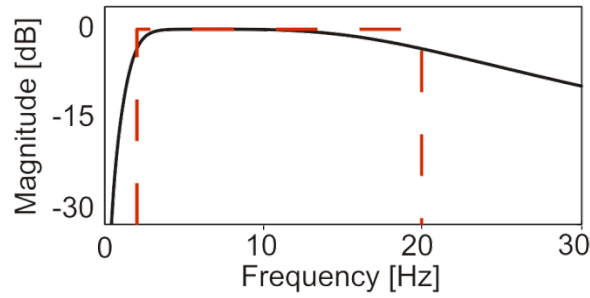
Figure 3.3: Response characteristic of the applied filter (black). The dashed red line marks the pass band.

In order to avoid filter artifacts at both ends, the filter interval has to be extended by a certain amount of data points before and after the end of a train. The response of the filter to a step of amplitude 1 has approximately a settling time of 500ms if an error band with an amplitude of 0.02 is assumed (see Figure 3.4). For the given sample rate of $Fr_s = 1kHz$, the filter interval is extend by 500 samples in front and 500 samples after the end of a train. The extensions are removed for further investigation.
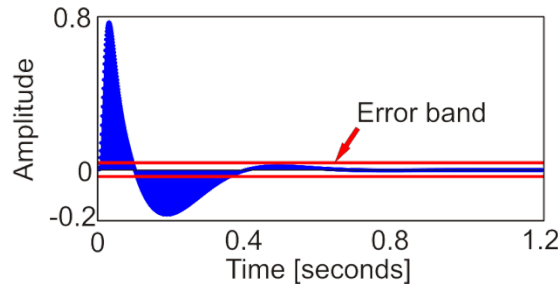
Figure 3.4: The step response (blue) to a step of amplitude 1. The red lines indicate the limits for the error band of amplitude 0.02.

Inspection of the measured data is conducted also visually. Of special interest are topographies obtained at the peaks of the global field power (GFP) for each of the stimulation periods. The GFP is calculated according to the reference free version described in (Lehmann 1980):

$$GFP = \sqrt{\frac{1}{2n}\sum_{i=1}^{n}\sum_{ii=1}^{n}(v_i - v_{ii})^2} ,$$

(3.1)

where n is the amount of channels, v_i, v_{ii} are the measured values at the channel indices i and ii. It is also common to normalize the GFP to the maximum value and thus express the GFP as percentage rate.

4. Methodological developments

4.1. Topographic Analysis

4.1.1. Reference atom

First, the stimulation frequency identical to the individual alpha frequency (1*alpha) is examined for each volunteer. The responses consistently produce the highest signal to noise ratio (SNR) and presumably the most stable topography. Second, the mean over 20 trains is calculated so that only one averaged train, representing 1*alpha, remains per volunteer (see Figure 5.5 for the GFP). For each of the 40 stimuli in that averaged train, 40 corresponding TMP atom sets are calculated. The atoms sets have a length of 125ms and an iteration depth of l=10 atoms. Additionally, the atom sets for 10 virtually following stimulations after the end of the 40 real stimulations are computed in a similar fashion. This is motivated by the assumption that the frequency entrainment will last after the end of the real stimulation (as it is obvious from Figure 5.5, the GFP is on the same level after the end of the stimulation as during the ~20 preceding stimuli).

For all atoms sets, except the virtual ones, a paired t-test is performed. The energy content of an atom set is compared to the energy content of each atom of the same set. Only the first atoms (atoms of the first iteration, l=1) of each atom set are significant at the 5% significance level of the t-test. Therefore further analysis is conducted with the first atoms only. From these 40 atoms (l=1), the average atom for each volunteer is computed separately for the EEG and the MEG. This average atom is called reference atom in the following. For each volunteer an individual reference atom is used. The topography of a reference atom varies over time, since there is a phase shift between the channels.

The similarity of the observed topographies and the reference atom is quantified by correlation coefficients. Correlation coefficients are computed between the reference atom and the 40 atoms used for building the reference atom, as well as the 10 virtual stimulation atoms after the end of the real stimulation. For each of the 40 + 10 stimulation periods, this results in one correlation coefficient per channel. Expressed in a different manner, one sequence of 40 + 10 correlation coefficients for each channel reflects the 40 + 10 stimulation periods.

For each sequence, the mean and the standard deviation (STD) of the first 40 correlation coefficients (cc) are calculated. The STD is applied as a statistical measure to categorize the 40 + 10 cc: inside the 90% confidence interval they were accepted (see Equation 4.1).

$$cc > mean(CSeq) \pm \frac{1.645 * \sqrt{Var(CSeq)}}{\sqrt{m}}, \qquad (4.1)$$

where $CSeq$ denotes a correlation sequence of m=40 correlation coefficients, the expression $\sqrt{Var(CSeq)}$ in Equation 4.1 denotes the STD of the correlation sequence.

In the next step, the obtained reference atom for each volunteer at the stimulation frequency of 1*alpha is used for the analysis of similarity of topographies at the other stimulation frequencies

4.1.2. **Multi trial**

The filtered data are averaged over the 20 trains of each stimulation frequency so that only one train per frequency and per volunteer remained. For the averaged train of each stimulation frequency, TMP atoms are calculated with an iteration depth of l=10. Atoms of length 125ms are computed. The atoms are calculated so that the absolute maximum of the GFP of a stimulation period is included. The maximum for each volunteer occurs relative to the onset of a stimulation period at approximately $0.9 * T_{ind,fr}$. The time point of this maximum is determined across all stimulation frequencies and volunteers. Thus, the stimulation onset, the individual length of the stimulation period, and the time point of the maxima determine the timeframe (with a length of 125ms) in which the atoms are calculated. The exact time index (translation) of the atoms is determined by the algorithm through an optimization of the translation parameter u. Even for not well phase locked cases, optimization of the translation parameter u ensures the approximation quality. Please note that for each of the 10 volunteers and each of the 15 stimulation frequency, atoms have to be calculated for 40 + 10 stimulations, accumulating to 7500 atoms.

Over all 10 volunteers, 15 stimulation frequencies and 40 (real) stimulation periods, thus 6000 atom sets (with 10 atoms each) and paired t-tests of the energy contribution of an atom set versus energy content of each atom of the respective atom set are computed. All atoms from the first iteration (l=1), only 5 atoms from the second iteration (l=2), and no atoms from all further iterations contribute significantly to the energy of the set of atoms at the 5% significance-level. Consequently, in the subsequent correlation analysis only the first atom (i.e. the one obtained in the first iteration) of each set of atoms is used.

As indicated in the previous section, the averaged atom (reference atom) calculated at 1*alpha serves as reference for the correlation analysis. For each volunteer and stimulation frequency, the (channel-wise) correlation sequences are calculated between the reference atom and each of the 40 + 10 first atoms. Figure 4.1 shows some correlation sequences between the reference atom and one first atom representing responses from a stimulation frequency. 1*alpha represents the ideal case; the channels of the EEG and MEG are (respectively) in phase and show (almost) identical patterns. 0.5*alpha and 0.9*alpha responses also show similar patterns, but reveal less synchrony across the channels. For 0.4*alpha, the responses differ from the 0.5*alpha, 0.9*alpha and 1*alpha, since the MEG shows no similarity to the MEG from 1*alpha. Although synchrony is given in the 0.4*alpha EEG, the maximal correlation coefficient (approx. 0.5) reveals a low correlation between the underlying atoms. A high similarity (or correlation) between the any correlation sequence (for, e.g., 0.9*alpha) and the 1*alpha correlation sequence indicates similarity of the

underlying function (e.g., 0.9*alpha atoms) to the reference atom. The opposite is true for low similarity; the compared correlations sequences reveal low similarity between the investigated atoms and the reference atom.
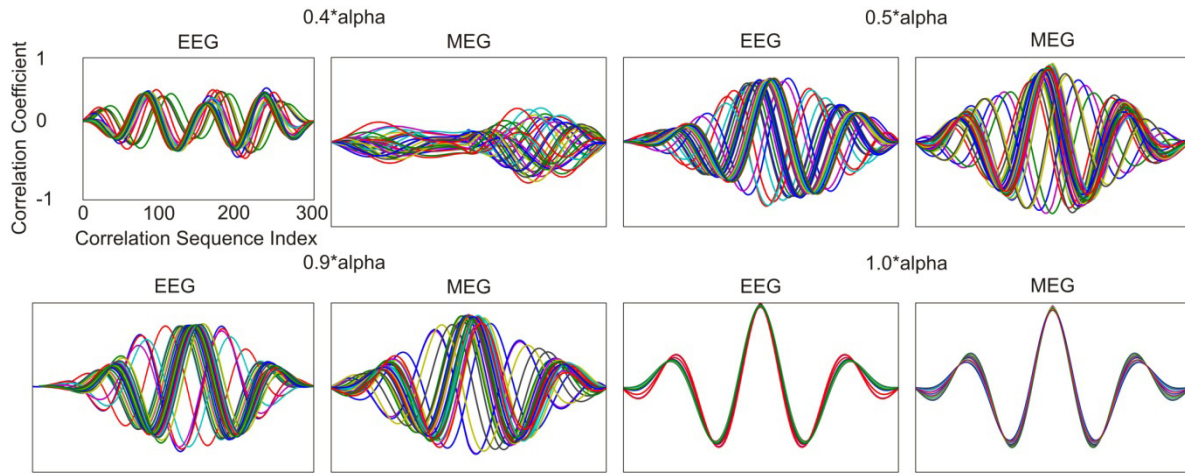
Figure 4.1: Correlation sequences for all channels between the reference atom and an exemplary multi-trial atom calculated for the indicated stimulation frequency. The correlation sequences, representing the EEG and the MEG for 1*alpha, show high similarity and synchrony. 0.5*alpha and 0.9*alpha show qualitatively the same behavior, but the channels are less synchronous than for 1*alpha. 0.4*alpha reveals synchrony, but also low correlation coefficients. Index 150 is the zero lag of the correlation sequence.

From each of the 40 + 10 correlation sequences, the correlation coefficients obtained at the index with the highest simultaneous correlation in all channels are selected. The selected correlation coefficients quantify the (channel-wise) similarity between the reference atom and the atom under consideration. For one stimulation period (of one volunteer and stimulation frequency; reference atom versus one atom from one stimulation period) this yields a vector of 32 correlation coefficients for the EEG-case and a vector of 31 correlation coefficients for the MEG-case. The concatenated vectors from all stimulation periods (of one volunteer and stimulation frequency; according to the type of recording) yield for each volunteer and stimulation frequency a series of 40 + 10 correlation coefficients for each of the 32 EEG-channels and 31 MEG-channels. This series of correlation coefficients is called a correlation coefficient sequence (note: this is not a correlation sequence). A total of 300 correlation coefficients sequences are calculated for the 10 volunteers and 15 stimulation frequencies and recording modalities (EEG/MEG).

The results are categorized as follows: outlying channels of cross-correlation sequences are discarded. A channel is considered outlying if its mean is outside the 90% confidence interval of the mean of a cross-correlation sequence (calculated over 40 stimulations; Equation 4.1). For a channel-wise approach, for each channel of these sequences the mean and the STD of the first 40 coefficients are calculated. Analogous to section 4.1.1, the correlation coefficients inside the 90% confidence interval were accepted.

4.1.3. **Single trial**

In contrast to the earlier steps, the atoms are now computed for the single-trial data. Thus, there is no averaging across the recorded trains. Instead, the correlation sequences from atoms which are calculated on not-averaged stimulation responses are averaged. This prevents an eventual smoothing of responses that are not well phase-locked to the stimulus, which might occur at stimulation frequencies other than 0.5*alpha and 0.9*alpha to 1.1*alpha. Single-trial analysis implies calculating TMP atoms for each of the 40 + 10 stimulations of 20 trains for each of the 15 stimulation frequencies per volunteer for EEG and MEG (300000 atoms). The reference atoms used here are the same as in the multi-trial analysis and are described in section 4.1.1. As before, only the first atom of each atom set is used.

Thus, for each volunteer, cross-correlation sequences are calculated between 2000 (20 trains à 40 + 10 stimuli per EEG and MEG) single-trial atoms per stimulation frequency and the respective MEG or EEG reference atom.

The cross-correlation sequences and the auto-correlation sequence of the reference atom are correlated. The correlation coefficients obtained at 100% overlap of the two correlation sequences (zero lag) represent the similarity of all approximated channels of one stimulus to the reference. Correlation coefficient sequences are produced from the single-trial correlation coefficients of one stimulation frequency. The sequences are averaged over the 20 single-trial correlation coefficient sequences of one stimulation frequency, so that one sequence of 40 + 10 correlation coefficients per stimulation frequency is produced.

4.1.4. **Frequency parameters**

Besides topographic analysis, the TMP decomposition also allows for an investigation of the frequency parameters of the stimulation responses. The examination bases on the TMP modulation parameters ξ calculated for 40+10 multi-trial responses. Thus, for each subject, a sequence of 40+10 modulation parameters ξ is created for each stimulation frequency. The modulation parameter sequences of a specific stimulation frequency are averaged across the subjects. This results in 15 averaged modulation parameter sequences, each representing a certain stimulation frequency. For each of the modulation parameter series the mean as well as the standard deviation are calculated from stimulus 10 to 40. From the mean and the standard deviation, the 90% confidence interval is calculated for each sequence according to Equation 4.1. Next, the parameter sequences are sorted into two categories: sequences of *category 1* show an increase of the modulation parameter during the first 10 stimuli, a clear plateau (not more than 3 modulation parameters ξ are outside the 90% confidence interval) for the stimuli 10 to 42/43 and a decrease of the modulation parameters ξ afterwards. Sequences of *category 2* show no increase before stimulus 10 and/or no decrease after stimulus 42/43. Thus, in *category 2*, there is no plateau.

4.2. **Source Localization**

4.2.1. **Introduction**

As a working hypothesis I assume that spatially defined sources underlie the topographies elicited during the experiment with flickering light. The sources must therefore show a development of their time and frequency parameters, which is highly similar the topographic patterns. The number of active sources is derived from the own research as well as from literature. Hence two sources in the occipital region of the brain have to be localized and described in their time and frequency parameters by the applied localization method. The TMP-method is well suited for the approximation and the description of the time-frequency parameters of a source; however, it is not capable of localizing its position. Consequently, a new, first source localization method on the basis of the TMP-algorithm has to be developed a) to overcome the lack of localization ability and b) to ensure the quality of the time frequency parameterization of the localized generators. This chapter describes the principle of operation of the newly developed method. The performance is verified by means of simulations (see section 6.1). Furthermore the method is applied to the experimental data described in section 3.1 and the corresponding results are analyzed in section 6.2.

4.2.2. **The source model: Dipole Atoms**

The dipoles are defined for the duration of the TMP-atom. Accordingly, a dipole of this source localization approach combines qualities of TMP atoms and dipoles to a construct which I call Dipole Atom DA. The Dipole Atom comprises also the direction (moment) known from the dipole. Further parameters from the MP-method are (see section 2.3): scale s, translation u, modulation ξ, normalization factor $\mathrm{K}_{(\gamma,\phi)}$ and time t. The new phase parameter ϕ_{DA} introduced for the dipole atom is calculated independently from the channel-wise TMP-phases $\Phi_{TMP,ch}$. TMP-atoms provide in the present case phases for 32 EEG channels, making it impossible to allocate TMP phase information to a single dipole atom.

My source model assumes that the EEG is produced by two mirrored neural sources. The parameters obtained from the TMP-atom (s, u, ξ, $\mathrm{K}_{(\gamma,\phi)}$, t) are identical for the dipole atom and the mirrored dipole atom. However, with regard to the new parameter sets (location, direction and phase), the dipole atom and its mirrored counterpart differ. The spatial coordinates of the dipole atom mirrored at the midsagittal plane yield the coordinates for the mirrored dipole atom DA_{Mirr}. The direction/moment parameters of the two dipole atoms are independent. The same holds for their phase parameters, yielding the phase parameter $\phi_{\mathrm{DA,Mirr}}$ for the mirrored dipole-atom. All parameters are static for the duration of one dipole-atom.

The midsagittal plane is constructed from individual electrode positions. First the sphere which best fits/approximates the electrode position is calculated. The center of this best

fitting sphere then serves as the origin of the coordinate system (electrode positions are transformed accordingly for the computations) and the midsagittal plane is defined by the origin and the sagittal coordinate axis.

4.2.3. The head model

A gain transfer matrix L typically relates points inside a brain volume to the sensor positions on the scalp and is based on assumptions made for geometric and electric/magnetic properties of a head. The head model I used is calculated based on a spherical 3-shell-model as introducedby (Rush and Driscoll 1968) by using the computation method introduced by (Berg and Scherg 1994) applying quasi static solutions to the Maxwell equations. The mirrored dipoles inside the brain volume (brain sphere) are thus related to the channels of the TMP-atom associated to the digitized electrode position.

My proposed source localization algorithm is verified by simulations (see section 4.2.7). Besides the already presented 3-shell approach, also a 4 shell approach as introduced by (Cuffin 1979) is applied. These two models use different values for modeling the conductivities and radii of the tissues and the cerebrospinal fluid (CSF). Table 4.1 gives an overview of the specification of the two models.

Table 4.1: A list of conductivities and radii as suggested in head models by (Rush and Driscoll 1968) (short RD1968) and (Cuffin 1979) (short Cu1979). Please note that the RD1968-model is a 3 shell model only, therefor it does not model the conductivity and the radii of the CSF. The Cu1979 as 4 shell model includes the CSF.

		Scalp	Skull	CSF	Brain
Conductivity (1/Ωm)	RD1968	0.33	0.0042	-	0.33
	Cu1979	0.33	0.0041	1	0.33
Radii (prop. to head radius)	RD1968	1	0.9280	-	0.8700
	Cu1979	1	0.9659	0.9205	0.8977

In the present algorithm the lead field L is constructed in two degrees of resolution, which is defined by a grid. The lead field L of the coarser resolution is calculated for the entire brain shell. The center of the finer lead field L is identical to the estimated position of the source in the coarser grid. The procedure requires a two-step algorithm.

In the first step a cubic grid is constructed inside the boundaries defined by individual anatomical electrode positions. Next, the electrode positions are projected onto a spherical surface representing the scalp surface. Accordingly, the cubic grid is transformed resulting in a grid with uneven distances between the grid points. Subsequently, the grid points outside the inner shell (brain shell) of the 3-shell head model are eliminated. For this transformed and reduced grid, a lead-field-matrix based on the head model is calculated. Thus, the grid points inside the inner shell (brain shell) of the 3-shell-model become the spatial coordinates for which the (mirrored) dipole atom(s) positions can be selected.

In the second step, following the optimal solution (section 4.2.5) found for the grid employed in first the step, the search is continued in a finer sub-grid, which is created based

on the untransformed grid. More specifically, this finer grid is constructed in the space spanned by the 26 neighboring grid-points surrounding the optimal location of the first step. The sub-grid is then transformed similar to the original grid. Moreover, the sub-grid points outside the brain-shell are eliminated.

4.2.4. Forward solution with Dipole Atoms

The combination of forward model and source model allows for the computation of a forward solution F_{Fwd}, which represents the, e.g., electric potential calculated for all sensors. The forward solution F_{Fwd} is thus a vector of the forward solutions $F_{Fwd,Sensor}$ of the amount n of considered sensors:

$$F_{Fwd} = \begin{pmatrix} F_{Fwd,Sensor\,1} \\ \dots \\ F_{Fwd,Sensor\,n} \end{pmatrix}.$$

(4.2)

The forward solution $F_{Fwd,Sensor}$ is then obtained via a product of the gain transfer matrix L and the source Q. As described in section 4.2.2, I model the underlying sources with the Dipole Atom DA, so that:

$$F_{Fwd,Sensor} = L_{Sensor}(x,y,z) * DA\big(s,u,K_{(\gamma,\phi)},\xi,t,\phi_{DA},dirx,diry,dirz\big),$$

(4.3)

where $L_{Sensor}(x,y,z)$ describes the gain transfer from one dipole (location defined by the Cartesian coordinates x,y,z) in the brain shell to the specific sensor in three spatial directions $dirx, diry, dirz$. Multiplication with the spatial components of DA generates a scalar value for the potential $F_{Fwd,Sensor}$. Equation 4.4 splits the dipole atom DA in its components:

$$F_{Fwd,Sensor} = L_{Sensor}(x,y,z) * \frac{K_{(\gamma,\phi)}}{\sqrt{s}} * g\left(\frac{t-u}{s}\right) * cos(\xi t + \phi_{DA})\begin{pmatrix} dirx \\ diry \\ dirz \end{pmatrix},$$

(4.4)

where $g\left(\frac{t-u}{s}\right)$ represents standard Gabor atoms. The parameters $s, u, K_{(\gamma,\phi)}, \xi$ and t are determined by the TMP-algorithm. Hence, for a further optimization routine they can be combined with the gain transfer matrix $L_{Sensor}(x,y,z)$ to a constant $C_{Sensor}(x,y,z)$ for each sensor and position in the brain shell. This leads to Equation 4.5:

$$F_{Fwd,Sensor} = C_{Sensor}(x,y,z) * cos(\xi t + \phi_{DA})\begin{pmatrix} dirx \\ diry \\ dirz \end{pmatrix},$$

(4.5)

with

$$C_{Sensor}(x,y,z) = (c_{Sensor,x}, c_{sensor,y}, c_{sensor,z})$$

(4.6)

As stated in section 4.2.2 the source model assumes two dipole atoms DA and DA_{Mirr} which form the (sensor-wise) forward solution $\boldsymbol{F_{Model,Sensor}}$. To obtain the position of the second dipole, the location of the first dipole is mirrored at the symmetry axis. The second dipole has an additional phase parameter $\phi_{DA,Mirr}$ and direction set $(dirx_{Mirr}, diry_{Mirr}, dirz_{Mirr})'$. The constant $C_{Sensor,mirr}(-x, y, z)$ for the mirrored case is located at the mirrored position $-x$. The forward solution $\boldsymbol{F_{Model,Sensor}}$ then is a superposition of two forward solutions:

$$\boldsymbol{F_{Model,Sensor}} = \boldsymbol{C_{Sensor}}(x, y, z) * cos(\xi t + \phi_{DA}) \begin{pmatrix} dirx \\ diry \\ dirz \end{pmatrix} +$$

$$\boldsymbol{C_{Sensor,mirr}}(-x, y, z) * cos(\xi t + \phi_{DA,Mirr}) \begin{pmatrix} dirx_{Mirr} \\ diry_{Mirr} \\ dirz_{Mirr} \end{pmatrix}. \qquad (4.7)$$

4.2.5. Inverse calculation

A two-stepped algorithm determines the best forward solution of the inverse problem (Not to be confused with the two steps of the lead field $\boldsymbol{L}$ calculation described in section 4.2.3). The first step hereby is the TMP-approximation, while the localization of the dipole atom constitutes the second step. The localization uses an optimizer to minimize the root mean square error ($RMSE$; see Equation 2.16) of the forward calculation.

The optimization problem is solved by a Differential Evolution (DE) optimization routine. The applied Matlab implementation (Buehren 2008) employs the core code of the original publication of the DE optimizer by (Storn and Price 1997).

Two phase parameters (ϕ_{DA} and $\phi_{DA,Mirr}$), two 3-D direction sets, one dipole magnitude and one coordinate set are optimized to minimize the $RMSE$ between the TMP-atom and the forward calculation. The optimizer has to fulfill several requirements. First, it has to deliver consistent results, even with a high number of parameters (12 in the present case) in reasonable time; second the implementation must be able to process both, integer, e.g., grid indices, and non-integer, e.g., direction values; third, the implementation has to take full advantage of the multi-core processors. I chose the DE optimizer since it provides the most reliable localization results of the tested optimization implementations (GA, Particle swarm, simulated annealing). The population size is set to 120, the number of iteration is set to 1000, the scale factor is set to 0.8 and a cross over rate is set 0.7. As mutation strategy, I chose DE/best/1/exp, which means that the best individual is chosen for mutation, that one mutation vector is used and that the 'exp' crossover mode is applied.

After finding the optimal solution for the inverse problem, the indices of the grid/sub-grid yield the coordinates of the dipole in the untransformed grid, thus the respective dipole-atom parameters are adjusted accordingly. Following the Matching Pursuit principle, the

best forward solution is then subtracted from the original signal. Based on the resulting residuum, a new TMP-atom is calculated, which allows for the localization of further sources. The algorithm is depicted in the flowchart in Figure 4.2.
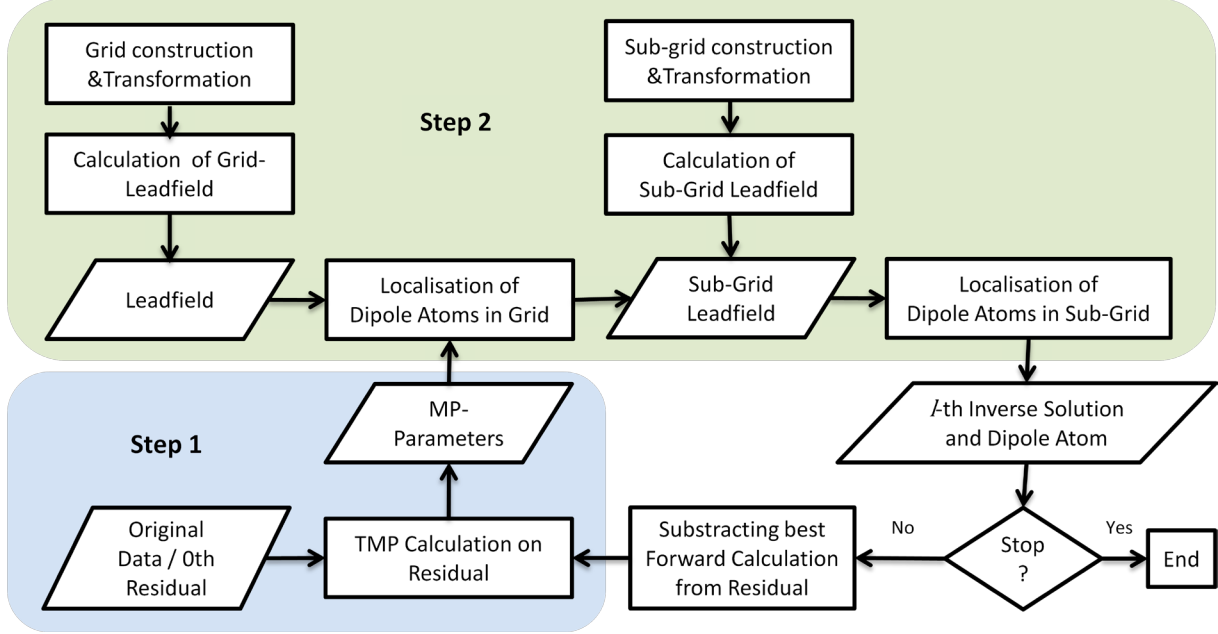
Figure 4.2: Flowchart depicting the two-step source localization algorithm. In the first step the Matching Pursuit parameters of the measured data (or residual of order zero) are calculated. In the second step, the lead fields for the grid and sub-grid are calculated. The MP-Parameters are then used in localization in the grid and sub-grid. The best fitting Dipole Atom then serves as the inverse solution. The according best fitting forward calculation is –if the algorithm is continued- subtracted from the data. The resulting residual is then subject to a new iteration.

4.2.6. Potential sources of error

The potentials one dipole generates on the scalp are defined by Equation 4.5. Replacing the term $C_{Sensor}(x, y, z)$ in Equation 4.5 as suggested in Equation 4.6 yields:

$$F_{Fwd,Sensor} = (c_{Sensor,x}, c_{sensor,y}, c_{sensor,z}) * cos(\xi t + \phi_{DA}) \begin{pmatrix} dirx \\ diry \\ dirz \end{pmatrix}. \qquad (4.8)$$

Equation 4.8 assumes that only one dipole atom acts as source and generates the potential $F_{Fwd,Sensor}$.

Through parameter optimization, the difference between the potential of a forward calculation $F_{Fwd,Sensor}$ and the measured potential $F_{Meas,Sensor}$ is minimized and is in the optimal case equal to zero.

$$F_{Meas,Sen}{}^2 - F_{Sim,Sensor}{}^2 = 0 \qquad (4.9)$$

This yields the following optimization condition:

$$F_{Meas,Sen}{}^2 - \left((c_{Sensor\,,x}, c_{sensor\,,y}, c_{sensor\,,z}) * cos(\xi t + \phi_{DA}) \begin{pmatrix} dirx \\ diry \\ dirz \end{pmatrix} \right)^2 = 0 \quad (4.10)$$

The solution to Equation 4.10 for the variables $dirx$, $diry$ and $dirz$ yields 8 different outcomes, one of which is denoted here as Equation 4.11 (refer to Appendix 1 for the complete set of 8 solutions).

$$\left\{ \begin{aligned} dirx &\to -\frac{F_{Maes,Sen} * Sec\,[\xi t + \phi_{DA}]}{c_{Sensor\,,x}}, \\ diry &\to -\frac{F_{Maes,Sen} * Sec\,[\xi t + \phi_{DA}]}{c_{Sensor\,,y}}, \\ dirz &\to -\frac{F_{Maes,Sen} * Sec\,[\xi t + \phi_{DA}]}{c_{Sensor\,,z}} \end{aligned} \right\} \quad (4.11)$$

The variables $dirx, diry$ and $dirz$ now depend on the constants $F_{Maes,Sen}$, $C_{Sensor}\,(x, y, z)$ and the secant (Sec) of the expression $\xi t + \phi_{DA}$. The modulation parameter ξ is given by the TMP-approximation and is constant for this purpose. Figure 4.3 shows the impact of the dipole phase ϕ_{DA} ($\phi_{DA} \in [0 \dots 2\pi]$) on the variables $dirx$ (Subplot A), $diry$ (Subplot B) and $dirz$ (Subplot C) at time index $t = 0$.
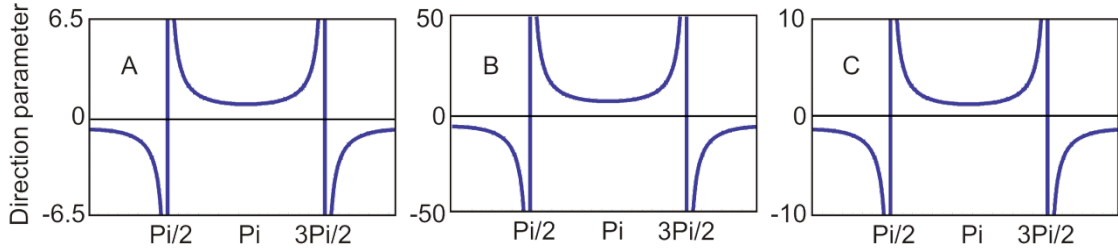
Figure 4.3: Impact of a change of the dipole atom phase ϕ_{DA} ($\phi_{DA} \in [0 \dots 2\pi]$, X-axis) on the magnitude of the variables $dirx$ (Subplot A), $diry$ (Subplot B) and $dirz$ (Subplot C) (Y-axis) by applying Equation 4.11. Random amplitudes are assumed for the following variables on which die directions depend: $Fmeas, Sen = 0.81$ and $C_{Sensor}(x, y, z) = (0.91\ 0.13\ 0.63)$. A small change in phase can have strong influence on the magnitude of the direction, and even switch the orientation by 180°, as can be seen by the impact of the dipole phase for $\phi_{DA} = \frac{\pi}{2}$ in the subplots.

As can be seen in all subplots of Figure 4.3 a small change in the phase parameter ϕ_{DA} can have a strong impact on the magnitude of the direction variables $dirx, diry$ and $dirz$. This particularly the case, if the optimization routine fails to accurately pinpoint the phase ϕ_{DA}, especially at values close to $\phi_{DA} = \frac{\pi}{2}$ and $\phi_{DA} = \frac{3}{2}\pi$. Thus a small phase error can entail a large direction error. This effect occurs also at indexes following $t = 0$. Figure 4.4 shows the trend from $\xi t = 0$ until $\xi t = \pi$. While completing half an oscillation, the direction parameters are definitely influenced by a jump equal to the example above ($\phi_{DA} = \frac{\pi}{2}$ and $\phi_{DA} = \frac{3}{2}\pi$).
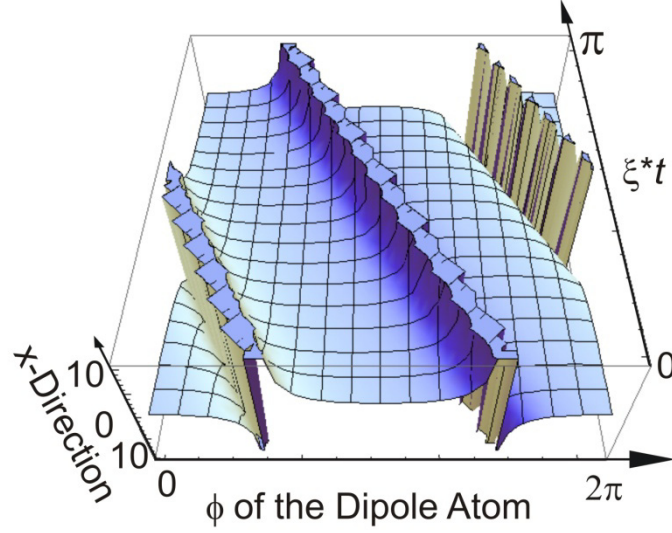
Figure 4.4: Influence of the dipole atom phase ϕ_{DA} (X-axis) on the dipole x-direction (Z-axis) displayed for one half of the oscillation cycle $\xi t = [0 \dots \pi]$ (Y-axis). In one half of an oscillation cycle for on dipole atom, the direction parameter crosses at least one point of discontinuity.

For the present simulations (section 4.2.7) with two dipole atoms and a phase difference of $\phi_{\text{DA}} - \phi_{\text{DA.Mirr}} = 1$, the situation complicates further. In an example with two dipole atoms, the phase of one dipole atom (e.g., $\phi_{\text{DA}} = \pi - 0.5$) allows for a reliable reconstruction of the direction error due to its small ϕ - dependent gradient. At this point a second dipole atom can be assumed, which has a phase (e.g., $\phi_{\text{DA.Mirr}} = \pi + 0.5$) that puts the direction parameter into an interval of a high ϕ - dependent gradient. In this example, the direction of one dipole atom would be reconstructed correctly, while the direction of the second dipole atom is influenced comparably strong by phase reconstruction errors. Figure 4.5 shows the direction parameters $dirx$ (blue) and $dirx_{\text{Mirr}}$ (red) for two dipoles with an assumed phase difference of 1rad.
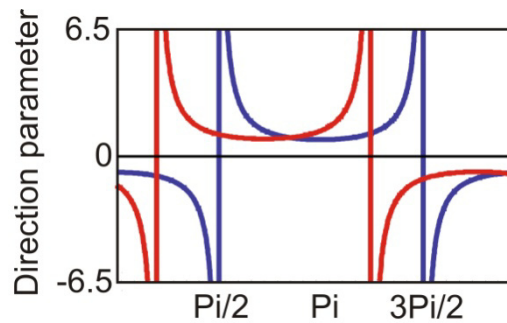
Figure 4.5: The magnitude of the direction parameters ($dirx$ (blue) and $dirx_{\text{Mirr}}$ (red)) of two (mirrored) dipole atoms with a phase difference of $\phi_{\text{DA}} - \phi_{\text{DA.Mirr}} = 1$. Slight phase variations can cause considerable variations of the magnitude of the direction parameter.

Furthermore, Figure 4.3 shows that all direction parameters show a sign change at the same phase ϕ_{DA}, regardless of the values of $C_{\text{Sensor}}(x, y, z)$. This indicates that, in some cases of ϕ_{DA}, a change of direction of the dipole by 180° can occur. In the case that the optimization

36

routine does not estimate one direction parameter in agreement to the others, the change of direction can amount to approximately 90°.

4.2.7. Verification with simulations

The performance of the source localization algorithm is tested with regard to several factors. The reconstruction error of simulated EEGs sheds light on the dependency on factors such as asymmetries and head models. The examined factors are described and listed below. The locations of the generator (dipoles) of the simulated EEGs are defined by all grid-points in a transversal plane in the back half of the head, by choosing the plane with the largest circumference (see Figure 4.6). The width of the brain hemisphere (average ~70mm) is divided into 6 steps, which yields a step size of ~11.6mm per grid point. Each simulation calculates the forward solution from two dipoles only – the original dipole and the corresponding mirrored dipole. Throughout the simulation, I apply dipole atoms with identical Matching Pursuit-derived parameters: (s, u, ξ, $\mathrm{K}_{(\gamma,\phi)}$, t) and moments, yielding simulation generators of the same frequency.

The impact of the following parameters on the goodness of localization was examined in a series of simulations:

- Phase relation of the two simulated generators (ϕ_{DA}, $\phi_{\mathrm{DA,Mirr}}$)
- Geometrical setup of the sources
- Model used for simulating and solving the inverse problem
- Employed MP-type.

Table 4.2 lists the parameter combinations of the verification process for the simulations/inverse pairs in cases A through E.

Table 4.2: Parameter changes during the verification process. In case A, all model assumptions used for simulation and inverse calculation are identical. In case B, the simulated dipoles have no phase difference. Case C introduces an asymmetric setup of the sources in the simulation. In case E, the simulation is calculated with dipoles of a phase difference, while the TMP model for the inverse solution employed a fixed phase approach.

CASE	Phases [rad] $\phi_{\mathrm{DA,sim}}$ $\phi_{\mathrm{DA,Mirr,sim}}$	Geometry	Simulation vs. inverse model	TMP model	Noise-factor
A (standard)	2, 1	Symmetric	Identical	VAR	[0, 0.1...1]
B (Equally phased)	0, 0	Symmetric	Identical	VAR	[0, 0.1...1]
C (Asym. Geometry)	2, 1	Asymmetric	Identical	VAR	[0, 0.1...1]
D (Dif. Models)	2, 1	Symmetric	Different	VAR	[0, 0.1...1]
E (2phase Simulated /TMPFIX inverse)	2, 1	Symmetric	Identical	FIX	[0, 0.1...1]
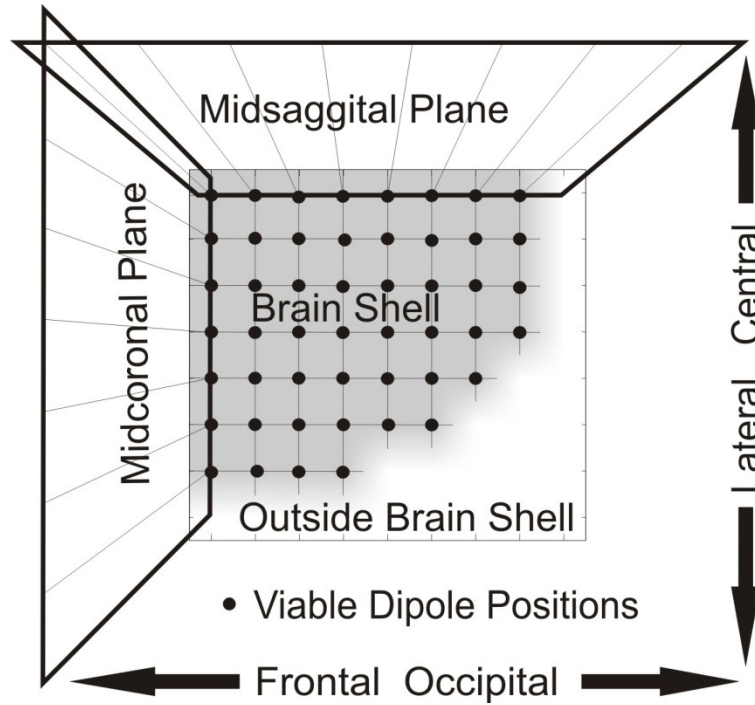
Figure 4.6: The plane (top view) in which the simulations take place. The black dots indicate possible dipole positions inside the brain shell (gray). The uppermost row of dipole positions is the symmetry axis i.e.: the midsagittal plane, while the leftmost column of dipoles is the midcoronal plane.

In case A, the parameters for creating the simulated potentials F_{Sim} are chosen so that they can be obtained by the source localization algorithm. The other cases are chosen so that the source localization algorithm cannot find a solution identical to the simulation.

In case B, the simulation is conducted with generators of identical phase. For evaluation of the error of phase reconstruction, the phases of the reconstructed generators are subtracted from each other. The absolute value of the reconstructed generator-phase-difference is subtracted from the simulated one. The phase relation of the two simulated generators (ϕ_{DA}, $\phi_{DA,Mirr}$) is in all simulation cases, except for case B, set to a generator-phase-difference of 1rad.

In case C, an asymmetric position is obtained by shifting the mirrored dipole one grid point (i.e.: $1/10^{th}$ of head radius) towards cranial. In all cases, except for the simulation case C, the generator positions are perfectly mirrored.

Case D tests the impact of different head models for the simulation and inverse calculation. The simulation uses the 4-shell model suggested by (Cuffin and Cohen 1979) and applies the Sun computation method (Sun 1997). For the inverse solution the model described in section 4.2.3 is applied.

Simulation case E deviates from the simulation procedure regarding the calculation of the inverse solution, in the sense that the TMP-phase model is altered. Case E restricts the TMP-phases to be of identical value (compare to Multichannel MP (Durka et al. 2005)). This restriction stands out against the standard TMP-approach, which explicitly allows for

different phases in its channels. Case E thus simulates two generators having a phase difference of 1rad, and localizes with a modified fix-phase TMP. However, the dipole fit still explicitly allows for a reconstruction with two dipoles with two independent phases.

Furthermore the impact of noise on the localization results is analyzed for each case of the simulations. Therefore, white noise of the amplitude range from -1 to 1 is multiplied with a variable weighting factor or noise-factor ([0, 0.1, 0.2...1]). This noise is further multiplied with the $RMSE$ (see Equation 2.16) of one simulation, which is taking all channels of the forward simulation into account. The resulting automatically scaling noise matrix is added to the forward simulation. The equivalent of signal-to-noise ratio in dB is given in Table 4.3, in which the values are calculated using the standard formula for SNR:

$$SNR = 10 * log_{10} \left(\frac{P_{Sig}}{P_{Noise}} \right), \qquad (4.12)$$

where P_{Sig} and P_{Noise} represent the power of the signal and noise. The periodogram estimates the power of the signal and the noise.

Table 4.3: Signal to noise ratio for different simulated noise level weighing factors and their equivalence as in [dB].

Noise level	0	0.1	0.2	0.3	0.4	0.5	0.6	0.7	0.8	0.9	1
SNR [dB]	inf	26	20	16	14	12	10	9	8	7	6

For each simulation, the Euclidean error distance is calculated in the untransformed state/grid. The quality of the reconstruction is evaluated by means of the goodness of fit (GOF_{Sim}) (Hara et al.1999):

$$GOF_{Sim} = 100 \sqrt{1 - \frac{\sum_{i=0}^{n}(F_{sim,i} - F_{inv,i})^2}{\sum_{i=0}^{n} F_{sim,i}^2}}, \qquad (4.13)$$

where $F_{sim,i}$ are the potentials obtained from the channels $i = 1 \dots n$ of the forward simulation including noise, while $F_{inv,i}$ are the solutions obtained from the channels of the inverse calculation.

5. Results of the topographic analysis

5.1. Fundamental Parameters

5.1.1. Measured topographies

The 20 filtered trains of one stimulation frequency are averaged for each subject. This yields for each subject one EEG train and one MEG-train representing the response to that specific stimulation frequency. Over the time course, for the responses measured for 1*alpha the EEG- and MEG-trains show repeating patterns. These topographies occur in a rhythmic pattern at the peak of the Global Field Power (GFP, see Figure 5.1 and Equation 3.1), agreeing with the stimulation frequency.
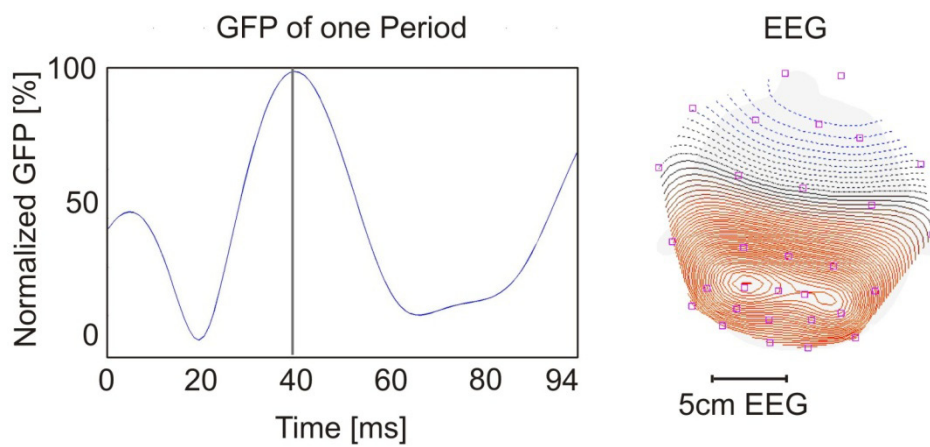
Figure 5.1: The GFP of one averaged stimulation period at 1*alpha on the left hand side, the black line indicates the index of the peak. On the right hand side the according EEG-topography recorded at the indicated maximum of the normalized GFP. The data are recorded at a sample rate of 1 kHz. The line increment for the EEG topography is 0.5µV per line.

The topographies at 1*alpha vary among the subjects as Figure 5.2 for EEG-topographies shows, so that no common topography can be determined.
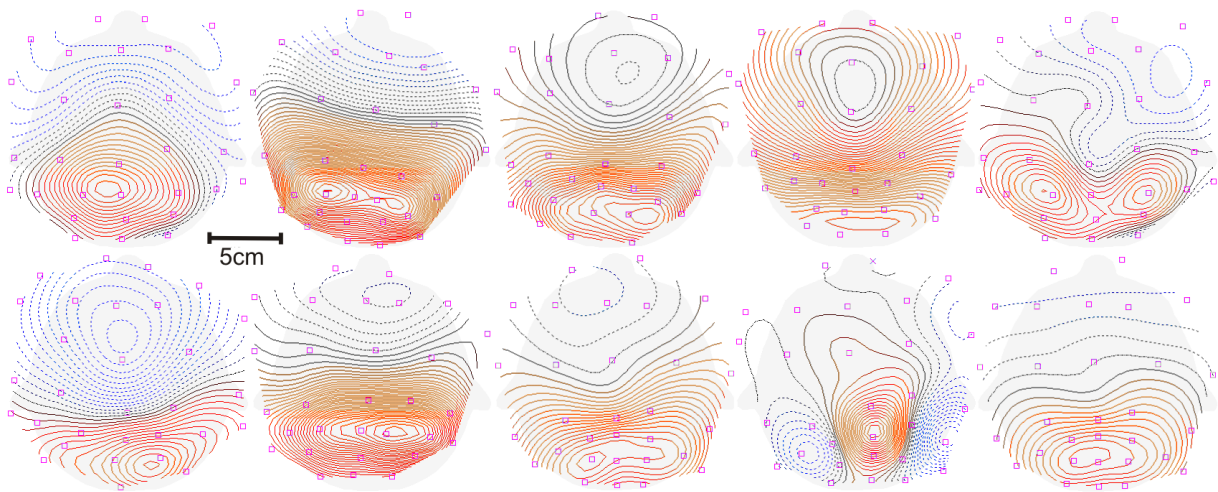
Figure 5.2: EEG Topographies of 10 subjects obtained at the peak of the respective GFP for 1*alpha. No interindividual similarities can be observed. The line increment for all EEG topographies is 0.5µV per line.

The topographies as depicted in Figure 5.2 develop at fix latencies relative to each stimulus onset and coincide with the maxima in the GFP. This latency is $\sim 0.9 * T_{ind,fr}$ (ind = individual; fr = stimulation frequency, thus $T_{ind,fr}$ is the individual period duration).
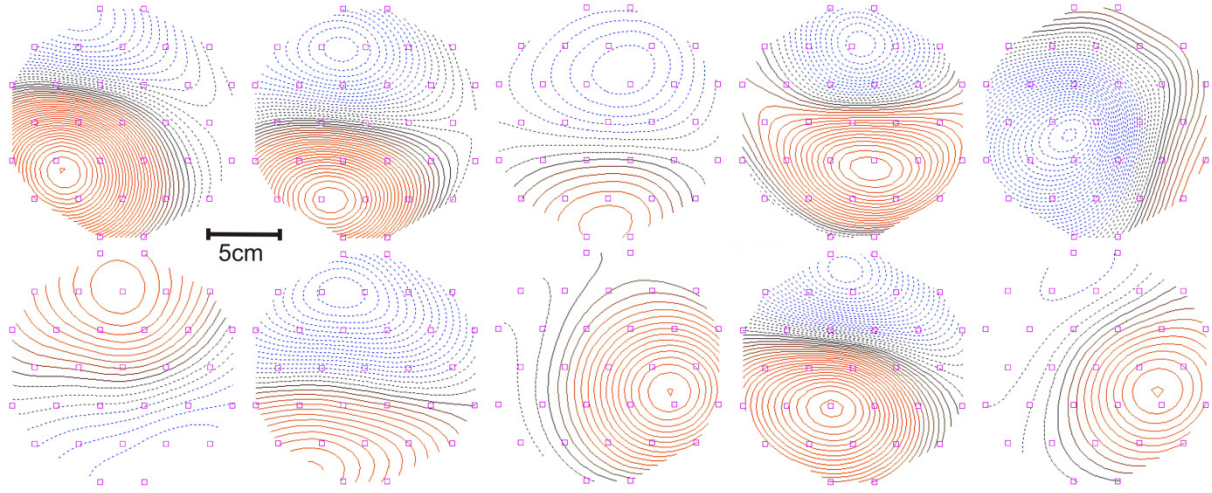
Figure 5.3 MEG topographies of 10 subjects obtained at the peak of the respective GFP for 1*alpha. The line increment for all MEG topographies is 10fT per line.

The strong positive EEG activity can be found in occipital regions with a maximum around the 10/20 electrode positions Po3, Poz, and Po4 extending to P3, Pz, P4, O1, Oz, and O2. The concurring MEG-topographies do not show a common form either (see Figure 5.3).
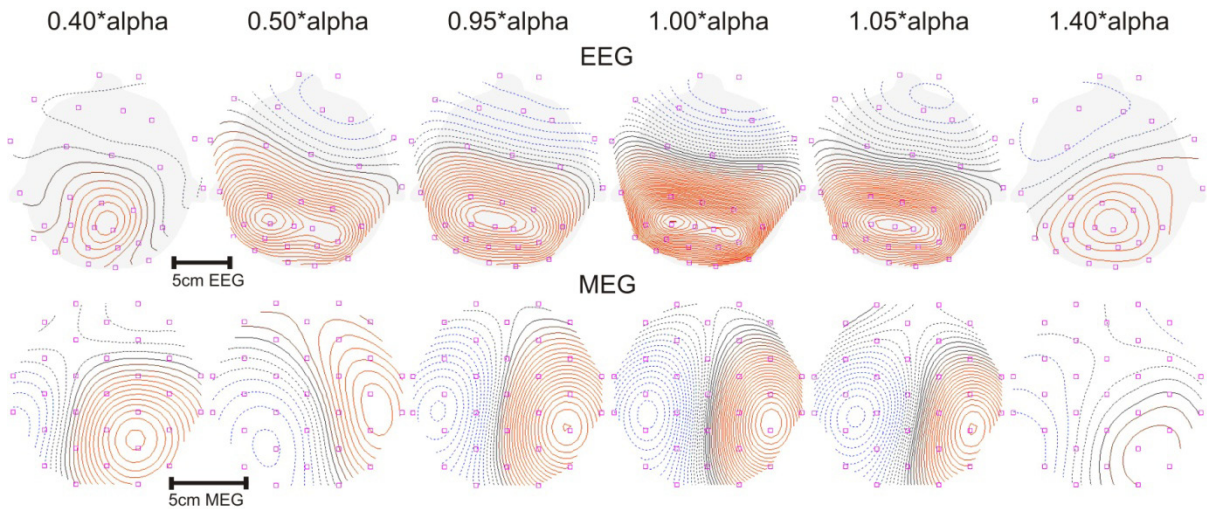
Figure 5.4: EEG and MEG topographies of one subject obtained at different stimulation frequencies. A visual similarity for the topographies of 0.50*alpha, 0.95*alpha, 1*alpha, 1.05*alpha is apparent. The other displayed topographies (also gained at the peak of the GFP) from stimulation frequencies are not comparable to the aforementioned ones. The line increment for the EEG-topographies is 0.5μV per line, for the MEG-topographies the line increment is 10fT.

Although no common EEG- or MEG-topography among the subjects can be determined, the responses for 1*alpha and 0.5*alpha produce intra-individually similar patterns. The same holds for topographies in the interval between 0.90*alpha and 1.10*alpha: they are visually

similar to 1*alpha. For topographies outside this interval the topographies obtained at comparable latencies to the stimulation ($0.9 * T_{ind,fr}$) and at the peaks of the GFP are visually different topographies. This is demonstrated in Figure 5.4, which depicts EEG and MEG examples for various stimulation frequencies.

In Figure 5.4, it becomes obvious that the response topographies depend on the stimulation frequency. Two types of responses exist for the EEG and MEG topographies. One type reveals a specific pattern for the stimulation frequencies from 0.9*alpha to 1.1*alpha and 0.5*alpha. For other stimulation frequencies no specific pattern is detected.

5.1.2. Development of response amplitudes with respect to the stimulus index

The first observations include the GFP obtained at stimulation with 1*alpha. Before the onset of the stimulation (i.e.: time index 0ms - 500ms) no specific response can be detected (see Figure 5.5). During the first 1.5 seconds (time index 501ms- 4260ms) of the stimulation, the GFP amplitude increases. In this case 1.5 seconds translate to an amount of approximately 15 stimulations. The amplitude of the GFP remains on an elevated level until the end of the stimulation. After the end of the stimulation, the GFP amplitudes remain at the same level for several hundred milliseconds and decrease rapidly to the GFP level before the onset of the stimulation (see Figure 5.5).
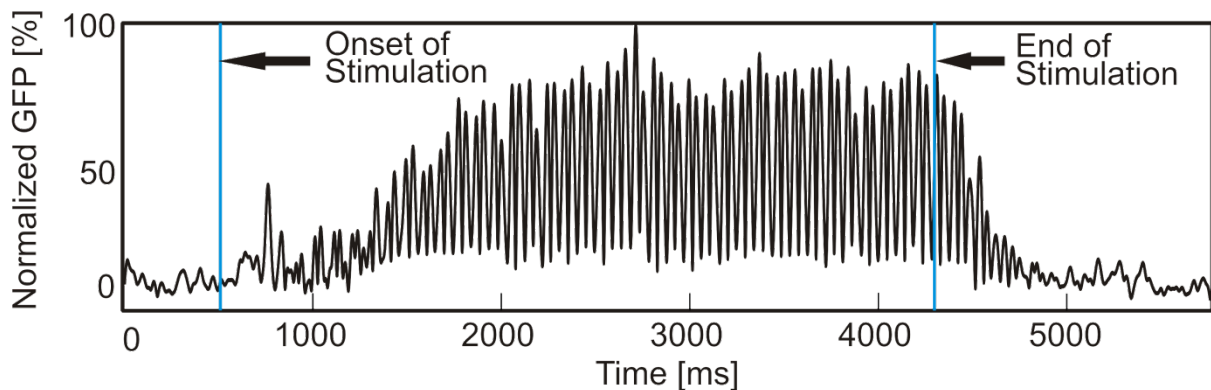
Figure 5.5: The development of the normalized GFP for stimulation with 1*alpha exemplified for one subject. The pre-stimulus ranges from 0ms to 500ms. The stimulation takes place between 501ms until 4260ms. Also the post-stimulus activity is given. The magnitude of the GFP increases over the first 1-1.5 seconds after stimulation onset. After the end of stimulation, the magnitudes remain on its former level for a short period of time. Thereafter it rapidly decreases.

5.1.3. Spectrum of flicker response

The magnitude of the flicker response depends on the stimulation frequency. A stimulation at 1*alpha elicits a much stronger response than a stimulation at, e.g., 0.4*alpha. This becomes obvious in a spectral analysis averaged over subjects and discriminated by stimulation frequencies. Table 5.1 lists the average power (interval 2-20Hz) from such an analysis performed by means of a periodogram of 1024 samples of filtered and averaged

responses. The onset of the analysis is the 10th stimulus (based on the results from section 5.1.2). The averaged elicited power in the analyzed part of the spectrum is high for the stimulation frequencies 0.5*alpha and 0.95*alpha through 1.05*alpha.

Table 5.1: Results of the spectral analysis averaged over subjects and discriminated by stimulation frequency. The stimulation frequencies are given as multiple of the resting alpha frequency (0.4*alpha – 1.6*alpha). The magnitudes of the EEG and MEG responses are normalized to the highest respective magnitude. The normalized magnitudes are highest around 0.5*alpha and 1*alpha.

	0.4	0.45	0.5	0.55	0.6	0.7	0.8	0.9	0.95	1.0	1.05	1.1	1.2	1.4	1.6
EEG	0.34	0.46	0.67	0.4	0.43	0.26	0.51	0.43	0.67	1.0	0.53	0.42	0.33	0.23	0.3
MEG	0.55	0.64	0.73	0.74	0.48	0.44	0.59	0.78	1	0.89	0.54	0.63	0.51	0.36	0.46

The responses obtained at various stimulation frequencies are spread differently over the analyzed spectrum. Figure 5.6 illustrates the distribution of the periodogram. Subfigures A (EEG) and B (MEG) in Figure 5.6 show the grand average periodogram, averaged over all subjects and stimulation frequencies. Again, the periodograms are calculated from a series of 2048 samples of filtered and averaged data, beginning at the 10th stimulus. For the given sample rate of 1 kHz, the frequency resolution is approximately 0.5Hz. Subfigures C (EEG) and D (MEG) of Figure 5.6 show the periodogram (2Hz-20Hz) averaged over subjects but discriminated by the stimulation frequency.

All spectra in Figure 5.6 indicate peaks at approximately 9-12Hz. The power at other frequencies is comparably low. A response to 0.4*alpha (bold blue line in subfigures C and D in Figure 5.6) stimulation adds only insignificantly to the average power. Furthermore, the power content is more evenly distributed than the other spectra. In the 0.4*alpha MEG-spectrum, the maximum lies at approximately 4Hz, not 10Hz. In the 0.5*alpha EEG-spectrum (bold red line in subfigures C and D in Figure 5.6), a clear peak for 10Hz appears, while in the MEG-spectrum the peaks are at approx. 5Hz and 10Hz and show a comparable magnitude (10Hz being stronger). The subsequent TMP-analysis will continue the investigation based on this spectral composition. As expected, the response for the 1*alpha spectrum (bold green line in subfigures C and D in Figure 5.6) show clear 10Hz peaks in both (EEG and MEG) spectra. The 1.6*alpha MEG and EEG spectrum (bold black line in subfigures C and D in Figure 5.6) reveals a behavior similar to the behavior of 0.4*alpha, more precisely both spectra show a low peak at approx. 10Hz and a second peak of comparable magnitude at the respective stimulation frequencies (~4Hz and ~16Hz).

A general observation drawn from the averaged MEG-spectrum (Subfigure B in Figure 5.6) suggests an elevated sensitivity of the MEG towards the low frequent activity/sources.

Please note that the elicited response-frequencies vary according to the individual alpha frequencies. Thus a smearing in the spectrum (e.g., the 0.5*alpha peak in the MEG-spectrum between 11Hz-12Hz) may occur.
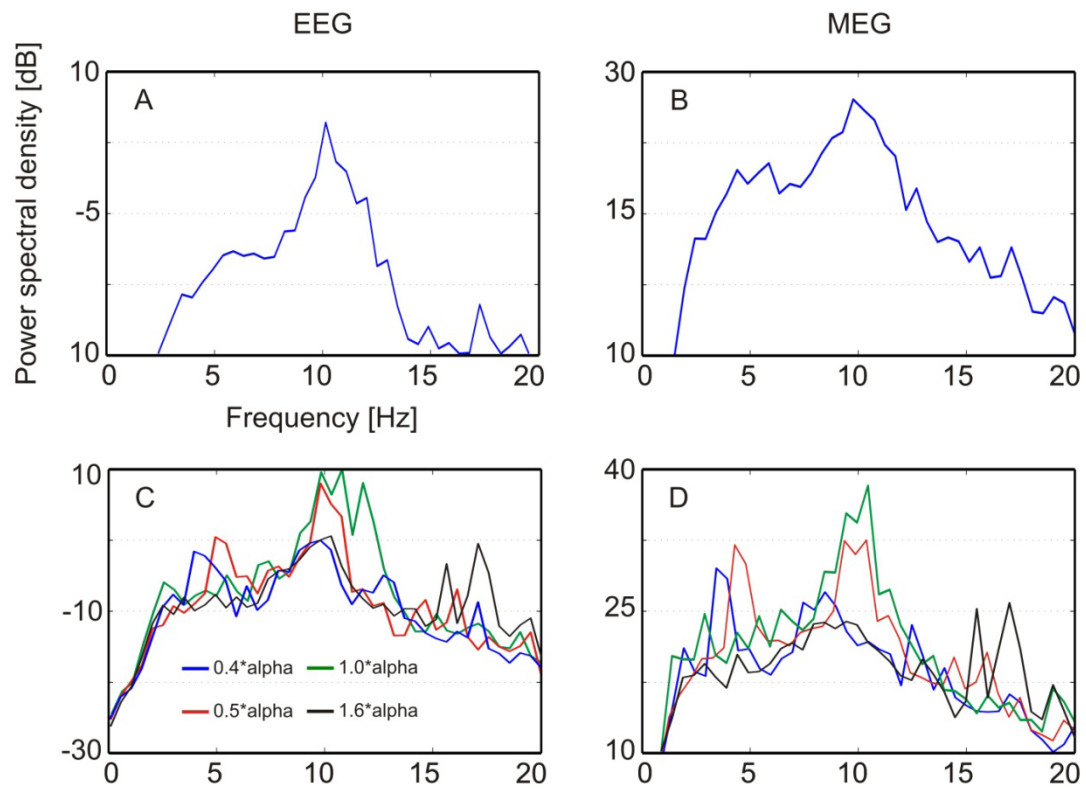
Figure 5.6: Periodograms of various stimulation frequencies for the EEG (subfigures A and C) and MEG (subfigures B and D). Subfigures A and B show the periodograms averaged over all subjects and stimulation frequencies. In subfigures C and D values are averaged over subjects but distinguished by stimulation frequencies. Power spectral densities for the following stimulation frequencies are shown: 0.4*alpha (blue), 0.5 *alpha (red), 1*alpha (green) and 1.6*alpha (black). The periodogram of the averaged MEG recordings shows a higher amount of ~5Hz activity in comparison to the EEG.

5.2. Topographic Analysis

5.2.1. Reference atom

The correlation coefficients between the reference atom and the 40 atoms building it, plus the 10 atoms obtained from 10 virtual stimulation periods (see section 4.1.2) quantify the similarity of the observed topographies (see section 5.1.1). The topography of a reference atom at maximum GFP is illustrated in Figure 5.7. The topographies vary over time.
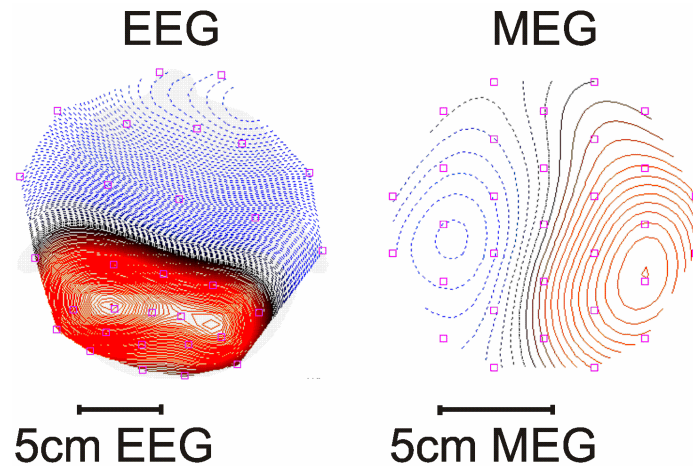
Figure 5.7: Topography of the reference atom of one volunteer at the maximum of the GFP: left EEG (line increment 0.1µV) right MEG (line increment 10fT).

The 40 + 10 stimuli produce a constantly high correlation from stimulus 10 to 43 in the correlation sequences. Before stimulus 10, there is an upward trend for the correlation coefficients. For the correlations from the 10th stimulus to the 40th stimulus, the coefficients are higher than 0.9 for 7 out of 10 volunteers (see example in Figure 5.8). The correlation values for the 10 atoms calculated after the end of the stimulation continued on the same level (Correlation coefficient > 0.9) for 3 atoms and drop thereafter to values comparable to the ones from the beginning of the stimulation (see example in Figure 5.8).

Thus, a correlation sequence plateau (note that there are only 40 stimuli; the next 10 atoms describe the ongoing EEG/MEG after the end of stimulation) is formed. For 3 out of 10 cases, a peak for stimulus 5, similar to the peak depicted in Figure 5.8 is detected. In 3 other cases the EEG-topographies became stable 4-6 stimuli later than the MEG- topographies.

Some channels show low correlation values, while most show similarly high correlation values. Correlation sequences with a mean outside the 90% confidence interval with respect to the mean and STD of all channels are excluded for the analysis of the correlation sequence plateau.

A comparison of the GFP at 1*alpha (see Figure 5.5) and a correlation coefficient sequence generated for 1*alpha (see Figure 5.8) reveals qualitative similarities of the respective structures. The GFP increases over a time of approximately 1000ms which is comparable –

for both, time and development - to the increase of the correlation coefficients over the first 10 stimuli. Additionally, both modalities show a stable phase afterwards. Both modalities show the same behavior after the end of stimulation, a continuation of stable amplitudes and correlation coefficients for the duration of 2-3 stimuli and a subsequent steep decrease.
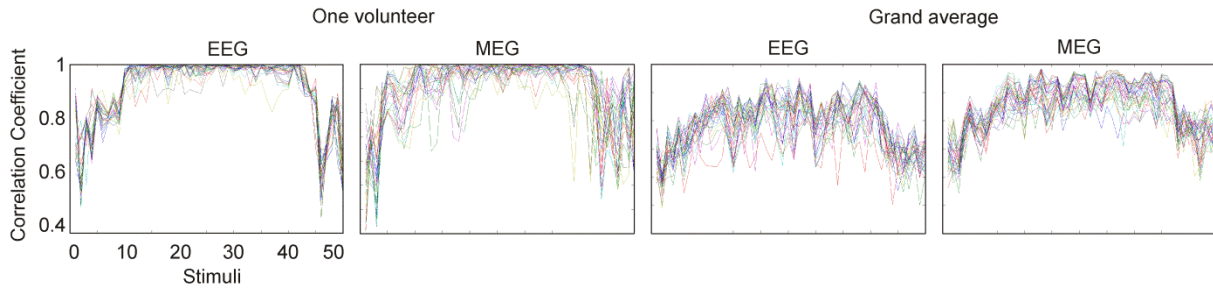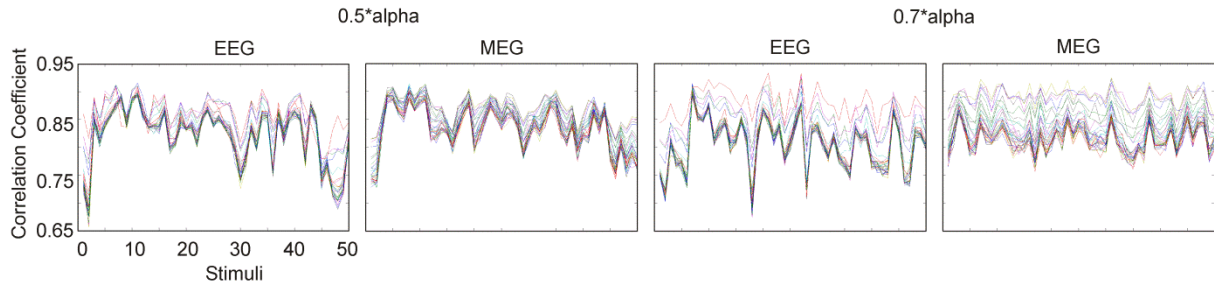

Figure 5.8: Correlation coefficient sequences for all EEG-channels and all MEG-channels plotted over 40 + 10 virtual stimuli for stimulation at 1*alpha (left: one volunteer; right: grand average for all volunteers). Note that the grand average included also those volunteers who did not show alpha entrainment. In all correlation sequences we can see an increasing slope in the beginning and a decrease after index 43.

5.2.2. **Multi trial**

The correlation analysis described in section 3.2.2 is now applied to all frequencies and all volunteers. Again, correlation sequences outside a 90% confidence interval are excluded from further investigation. Close to the individual alpha frequency, 3 phases of the correlation sequences (increase up to the 10th stimulus; plateau; a decrease starting with the 3rd virtual stimulus) become obvious, which are similar to the results in section 5.2.1 for 7 out of 10 volunteers.

Table 5.2 Percentage of subjects who show *good, moderate* or *weak* correlation sequences (E refers to the EEG, M to the MEG). Good and moderate cases can almost exclusively be found in close interval around the stimulation frequencies 0.5*alpha and 1*alpha.
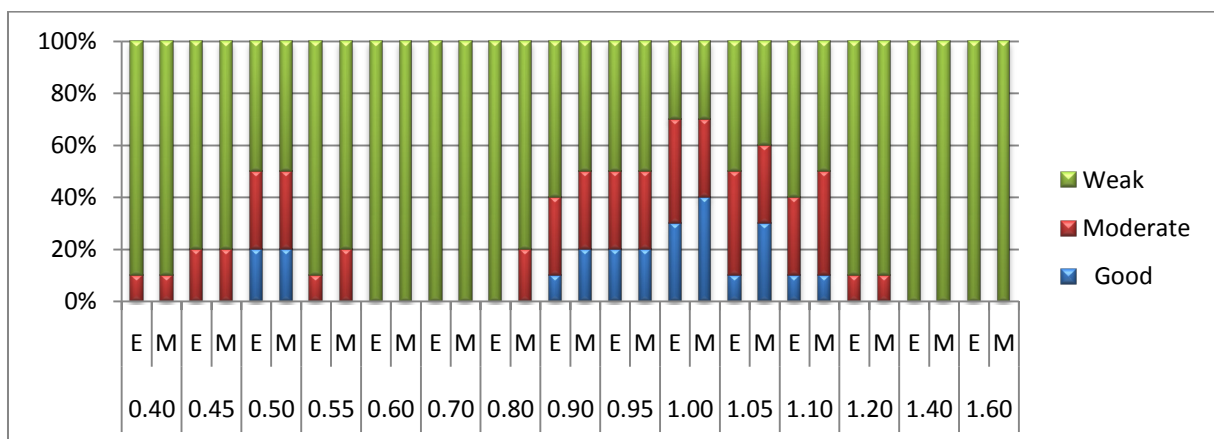
Subsequently the correlation sequences obtained from all stimulation frequencies are categorized as good, moderate and weak. A good correlation sequence contains a clear rise of correlation coefficients within the first 10 stimuli, a stable correlation sequence plateau and a clear decrease after the 43rd atom. For the moderately distinct correlation sequences a

rise over the first 10 stimuli as well as a decrease after the 43rd atom is also required. However, the correlation plateau could be interrupted for up to 5 stimuli. For weak resemblances, the three phases mentioned above are not clearly distinguishable. The results are given in Table 5.2.

For the stimulation frequencies 0.45*alpha until 0.55*alpha and 0.90*alpha to 1.10*alpha good to moderate correlation sequences are detected, which is not or is rarely the case outside the described frequency range. For the stimulation frequencies of 0.9*alpha and 1.10*alpha, the number of very and moderately distinct correlation plateaus decreases. For 0.5*alpha, 2 very distinct and 3 moderately distinct correlation plateaus are detected.

The increase of the correlation coefficients until the 10th stimulus and the decrease after the 43rd are still statistically validated, but are not as distinct as around 1*alpha. This might be due to a lower signal to noise ratio (SNR) resulting from weaker responses to stimulation. On the whole, slightly more good/moderate results are present for the MEG than for the EEG. According to the categorization, (see Table 5.2) the MEG scores equal or higher than the EEG.
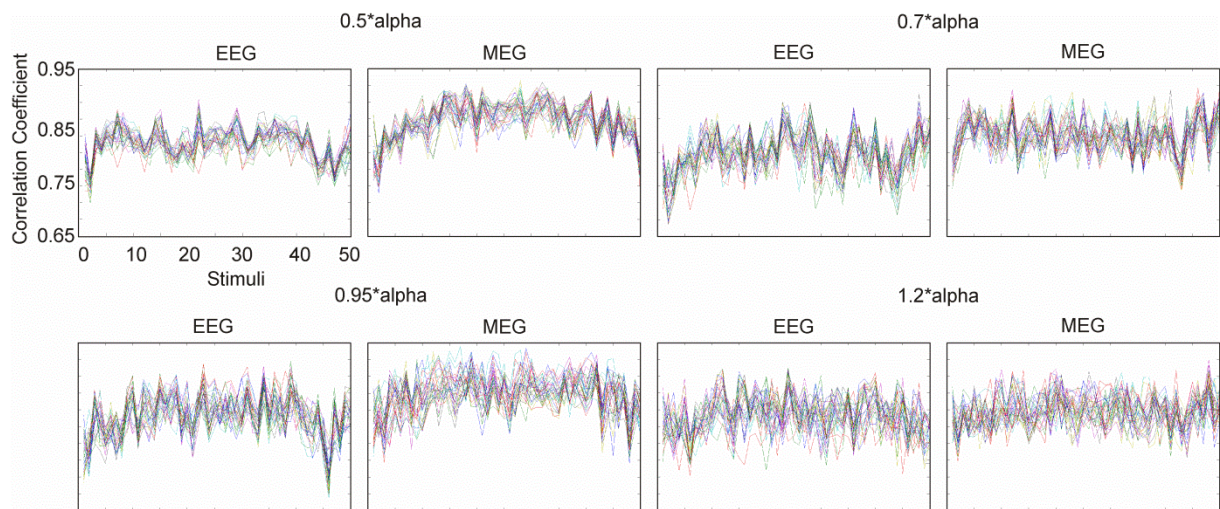
Figure 5.9: Correlation values for all EEG-channels and all MEG-channels plotted over 40 + 10 virtual stimuli for stimulation at 0.5, 0.7, 0.95, and 1.2*alpha (grand average for all volunteers). Note that the grand average includes also subjects who do not show alpha entrainment.

For 3 out of 10 subjects the rise takes only 5 stimuli. However, the 3 subjects with an early rise at 0.5*alpha are not the same as the 3 subjects who show a peak at stimulus 5 at 1*alpha (or the reference atom). Figure 5.9 shows the grand average of the correlation coefficients for four different stimulation frequencies. Noticeable correlation sequence plateaus are detected only for 0.5*alpha and 0.9*alpha to 1.1*alpha.

From the 10th until the 40th correlation coefficient of a sequence, the mean for each channel is calculated. Setting a threshold at 0.75 for the mean value reveals occipital and frontal regions of interest in the EEG. This is done separately for each subject and occurs only for the stimulation frequencies 0.5*alpha and 0.9*alpha to 1.1*alpha. When plotted onto a

head surface, channels above the threshold of the correlation values form two continuous patches for the stimulation frequencies 0.5*alpha and from 0.9*alpha till 1.1*alpha (see Figure 5.10 for an example of one subject). In the occipital region the energy in the observed channels is higher, in the frontal region lower. Therefore the frontal patch does not represent frontal activity but might stem from the occipital sources. In the MEG one region appears after applying a threshold of 0.9 for the correlation coefficients (again only in 0.5*alpha and 0.9*alpha - 1.1*alpha). The MEG region of high correlation coefficients covers and connects the channels with the highest absolute amplitude. The MEG is, however, located only over occipital part of the head, so no further information about the frontal region is available.

So far, analysis is based on averaged data. The next section focuses on single-trial analysis.
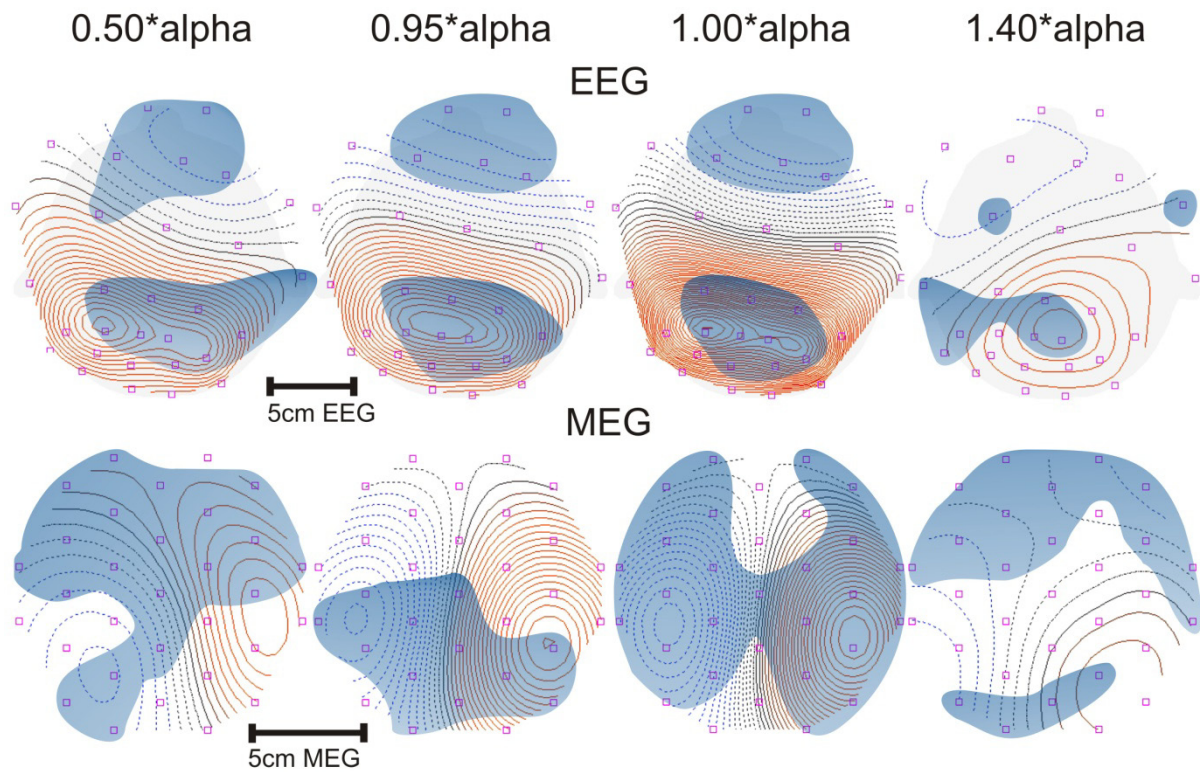
Figure 5.10: The marked patches indicate zones in which all electrodes show high correlation values (not activity) throughout the stimulation at various stimulation frequencies. The zones of high correlation in the EEG for 0.5*alpha 0.95*alpha and 1*alpha are located comparably in the frontal and occipital region, while the zones at 1.4*alpha are not related to these zones. The zones in the MEG are less clear, however large symmetric zones are found for the first three of the depicted stimulation frequencies. The line increment is 0.5μV for the EEG and 10fT for the MEG.

5.2.3. **Single trial**

Similar results to those described in the multi-trial analysis in section 4.1.2 are found also for 4 out of 10 subjects in the single trial case. Figure 5.11 displays the similarity between the individual reference and the single-trial atoms at 1*alpha for one of the four volunteers. For approximately 10 stimuli the correlation coefficients increase, thereafter the plateau is

reached. For 2 to 3 periods after the end of the stimulation high correlation-coefficients are still present. Thereafter the values drop to the initial values. This effect appears in EEG and MEG data.
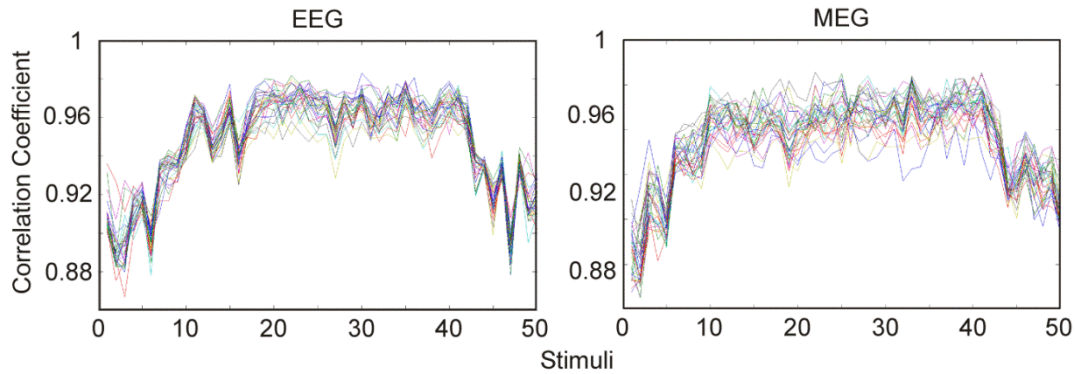
Figure 5.11: Correlation values for all EEG-channels and all MEG-channels plotted over 40 + 10 virtual stimuli for stimulation at 1*alpha for one volunteer (the correlation coefficient sequences are averaged over 20 single trains).

The results for the same volunteer at 0.5 and 0.7*alpha are displayed in Figure 5.12. As expected, the correlation coefficients obtained for 0.5*alpha show the same qualitative behavior as for 1*alpha. This behavior is, however, not that pronounced. For 0.7*alpha, this behavior cannot be found. Additionally, both the EEG and MEG channels show a more diverging behavior for 0.7*alpha.

Figure 5.12: Correlation values for all EEG-channels and all MEG-channels plotted over 40 + 10 virtual stimuli for stimulation at 0.5*alpha (left) and 0.7*alpha (right) for one volunteer (the correlation coefficient sequences are averaged over 20 single trains).

5.2.4. Frequency parameters

As stated in section 5.1.2, the magnitude of the GFP increases over the first 7-10 stimuli in both modalities. Furthermore, for certain stimulation frequencies, topographies increase in their similarity to the reference over the first 10 stimuli. This suggests the occurrence of an engagement for the first 10 stimuli and a disengagement effect after the end of stimulation. The following results give insight into the behavior of the TMP modulation parameters ξ and thus into the frequency.

The first observations are that, with the exception of 0.4*alpha, all stimulation frequencies reveal a behavior categorized as *good*. Thus, for most of stimulation frequencies, the

modulation parameter ξ increases over the first $5 - 10$ stimuli (depending on the stimulation frequency). From stimulus 11 to 42/43, the modulation parameter ξ lies outside the 90% confidence interval for a maximum of 3 instances per stimulation frequency. After the $42^{nd}/43^{rd}$ period, the modulation parameter ξ decreases (see Figure 5.13). This effect occurs in both modalities, the EEG and the MEG. As a special case, the responses of 0.45*alpha exhibit a plateau structure, but have the highest number of confidence interval violations and the weakest increase over the first stimuli.
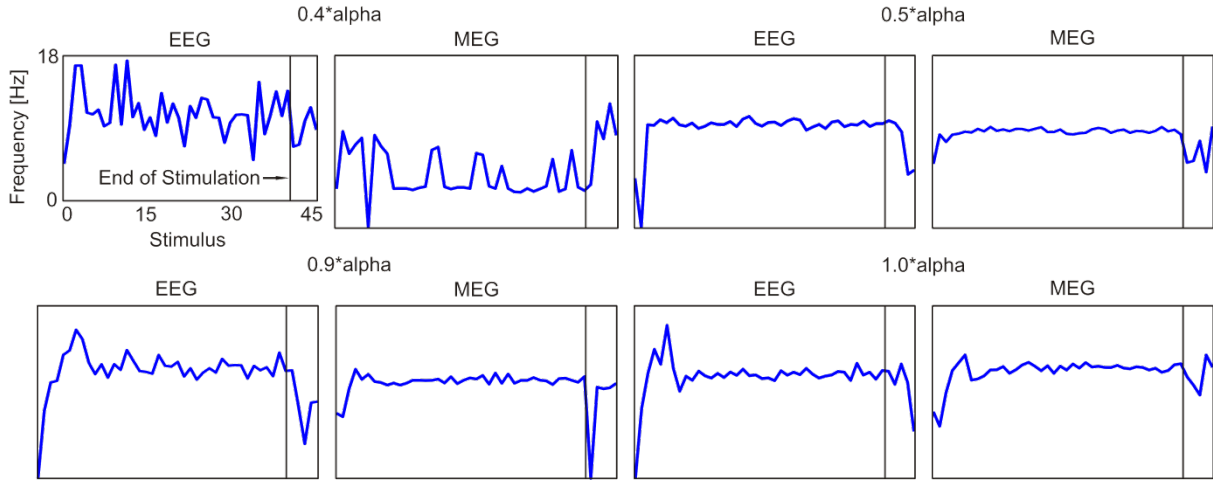
Figure 5.13: Modulation parameter ξ gained from single-trial analysis averaged over trials of one subject distinguished by stimulation frequencies and EEG/MEG. The vertical line indicates the end of the stimulation (stimulus 40).

The response frequencies are similar in the EEG and in the MEG in all cases except for 0.4*alpha (see Figure 5.13). Furthermore, the behavior along the stimuli is similar in EEG and MEG. For example, 0.9*alpha and 1*alpha show strong peaks in EEG for stimuli 5-10, which cannot be detected at 0.4*alpha. Peaks are less pronounced in the MEG than in the EEG. These overshoots in the MEG and the EEG might be an effect of the synchronization of coupled nonlinear oscillators as they are tuned to the stimulation frequency (Buchli et al. 2008). For 0.5*alpha, the overshoot does not occur, which might indicate a weaker coupling.

The modulation parameter ξ at the onset of the stimulation is 5 ± 0.7Hz for all averaged stimulation frequencies. Table 5.3 lists the modulation parameter ξ and its standard deviations for all stimulation frequencies. The highlighted stimulation frequencies show a comparatively low value for the standard deviation.

Table 5.3 The mean and the standard deviation of the modulation parameter ξ for one subject (same as in Figure 5.13). The highlighted stimulation frequencies show a comparatively low value for the standard deviation.

Stimulation Frequency	0.4	0.45	0.5	0.55	0.6	0.7	0.8	0.9	0.95	1	1.05	1.1	1.2	1.4	1.6
Mean (Hz)	4.8	5.8	11.3	5.9	6.4	7.3	8.6	10.3	10.9	11.6	11.6	11.4	12.3	13.8	16.4
STD	1.56	1.16	0.24	0.48	0.46	0.39	0.31	0.32	0.44	0.29	0.25	0.46	0.47	1.16	1.53

6. Results of Source Localization

6.1. Results of the Simulation

6.1.1. Introduction

The following sections describe the findings regarding the dependency of the localization precision, reconstruction of the dipole-phase, reconstruction of dipole directions and the GOF for the simulated cases portrayed above. The localization error is given in grid points, thus an error value of 1 is equal to a tenth of the head radius. The error of the dipole-phase reconstruction is given in [rad]. I calculate this phase-error by subtracting the absolute values of the phase-difference of the reconstructed dipoles ($\phi_{DA,rec}$, $\phi_{DA,Mirr,rec}$) from the simulated ones ($\phi_{DA,sim}$, $\phi_{DA,Mirr,sim}$). For the error of the dipole directions, the angles between the simulated dipoles and their reconstruction are determined. The two resulting angles are averaged. Since no negative angles could occur, this results in a Combined Direction Error, which is given in degrees. For each noise level the error values of the simulations at all grid positions are averaged and yield the results listed in Table 6.1-Table 6.5.

6.1.2. Localization, phase and direction errors: Case A

Case A uses a symmetric setup and sources with a phase difference of 1rad. As expected, the mean localization error increases with the noise level but remains smaller than one grid point. Additionally, the variance does not show any significant change. At low noise levels dipoles can be localized exactly, while elevated noise levels do not allow for an exact localization of the dipole. At low noise levels, the phases can be reconstructed with little error (mean: 0.06rad). The average phase error and small variance value indicate that the phases are estimated with little deviation from the simulation without noise. The error of the phase reconstruction increases with noise. The combined error of the reconstructed direction error fluctuates around a constant level for all noise levels. Since the GOF_{Sim} relates the quality of reconstruction to the simulation including noise, it decreases with an increase of noise.

As described in section 4.2.7, the localization errors are calculated for simulated generators placed in a transversal plane in the back half of the simulated head. In the descriptive figures (see below) only one half of the plane is displayed since the reconstructed dipoles are mirrored (on the X-axis). In this representation, an index of value 10 corresponds to the outer radius of simulated head shell. Missing grid point indices on the X or Y axis to 10 are explained by the head model, which has a brain shell radius of 0.7*outer head shell radius. The white area marks grid points outside the brain shell.
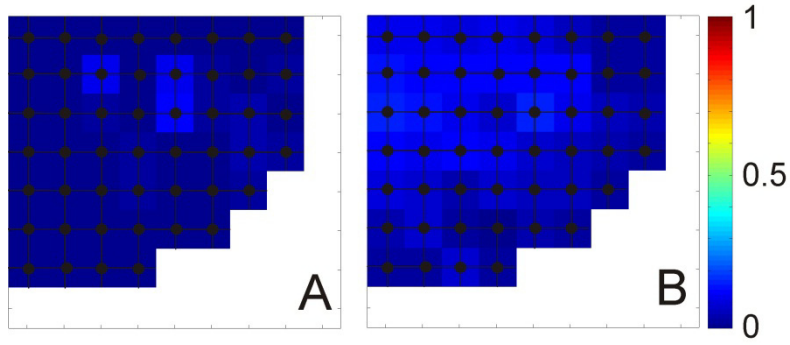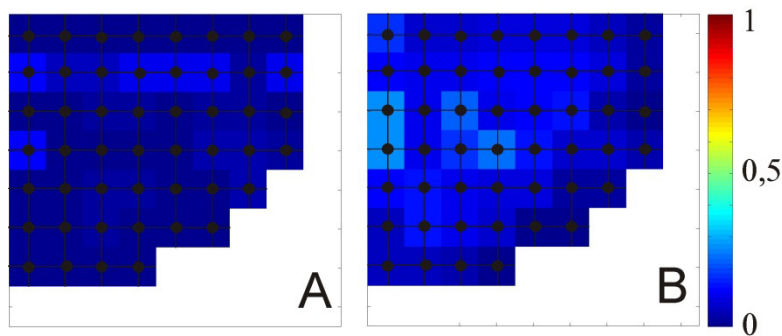
Figure 6.1: Localization error in Case A for all viable dipole positions in the simulated plane. Subfigure A shows the results for a noise level 0, while subfigure B shows the results for noise level 1. The error is color encoded (see scale) and is expressed in grid points. The white area lies outside the brain shell.

The localization errors of each simulated dipole is encoded in a color scale and allocated to its respective simulated position in the plane (Figure 6.1). The left hand side shows the zero noise case, while the right hand side displays results for a noise level of 1. The localization error depends on the location in the plane. The localization for the grid points at brain shell border or one grid point towards the center is on average better than for grid points deeper in the simulated brain. The localization error at the occipital end of the symmetry axis (and one grid point away) is comparably low.
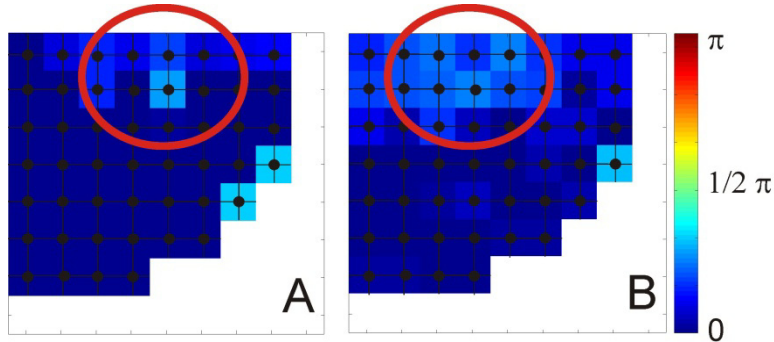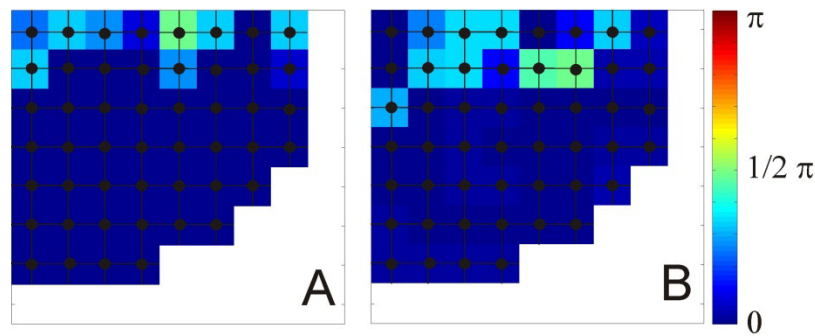

Figure 6.2: Map of the phase error in the simulated plane in case A. Subfigure A shows the results for noise level 0, while subfigure B shows the results for noise level 1. The phase error is color encoded, so that 'blue' signifies no error, while 'red' stands for a phase error of π rad. The red circles mark the zone of highest phase error. White lies outside the brain shell.

The phase errors at noise level of 0 are portrayed in the left subfigure of Figure 6.2. The right subfigure displays the phase reconstruction error for a noise level of 1. The reconstruction of phases shows dependency on the distance from the symmetry axis as well as the noise level. At a noise level of 0, the reconstruction of phases is worst on the symmetry axis. Phases are reconstructed with little error and variance for the rest of the plane except for 5 instances, one of which is located close to the symmetry axis, on half distance from the center of the brain shell to its border.

For the noise level 1, the phase reconstruction error is highest for the symmetry axis and the directly adjacent grid points. The incidences of high phase reconstruction error are concentrated around the grid point close to the symmetry axis specified for the 0 noise case

above (red circles in Subfigure B in Figure 6.2). Since the expected location of generators of the flicker experiment are located close to the symmetry axis, a noise dependent error of the phase reconstruction must be assumed.

For low noise the phases are reconstructed in a satisfactory manner, since only 11 out of 49 error values deviate from 0. Seven out of the 11 deviations occur for simulated sources on the symmetry axis. At all noise levels the phase reconstruction error increases with the proximity to the symmetry axis and at two locations on the brain shell border. Reconstructions at these locations consistently produce the strongest phase-error.
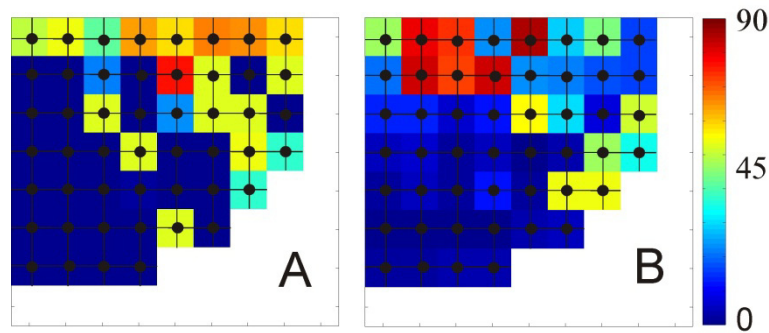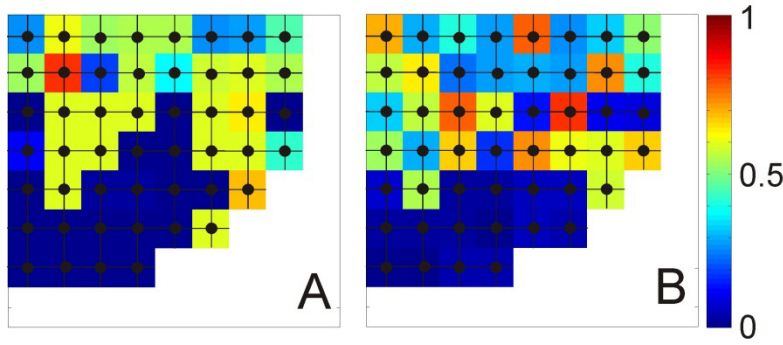

Figure 6.3: Combined Direction Error in degrees in the simulated plane in case A. Subfigure A shows the results for noise level 0, while subfigure B shows the results for noise level 1. The direction error is color encoded.

The Combined Direction Errors at noise level of 0 are portrayed in the left subfigure of Figure 6.3. The right subfigure displays the error of the direction reconstruction for a noise level of 1. For a zero noise level the error depends on the dipole position relative to the symmetry axis, the error being highest directly on the symmetry axis. Additionally, the Combined Direction Error increases with the proximity to the occipital region. Although the average value of the direction reconstruction error (see Table 6.1) yields a value of 22.3°, the directions are reconstructed with small deviations <5° for 28 out of 49 grid points. The remaining 21 (8 of which are on the symmetry axis) directions show an error of approximately 55°-65°, thus explaining the elevated variance values. The Combined Direction Error takes in account both dipole directions. The predominately high values for this error and the lack of error values between ~5° and ~55° can be interpreted as a (accidental) swap of the dipole-EEG-Topography-allocation; hence one of the located dipoles in the, e.g., *left* hemisphere, points towards the *right* (occipital) head surface. This would explain the direction error on the symmetry axis. However, another explanation is given in section 7.2.2.3.

In the case of noise level 1, the amount of high Combined Direction Error (~60°) is reduced to 7 incidences. The number of a more moderate direction reconstruction error is increased to 37. The directions are reconstructed with a high degree of error, which is explained by the increased noise in the simulated data. As subfigure B in Figure 6.3 shows, another region with a high degree of direction error occurs. It is the same region that accumulates high phase error of approximately 90° (compare with above Figure 6.2, red circles). Thus, in this

zone a double (accidental) swap of the dipole-EEG-Topography-allocation occurs: both dipoles point towards the opposite hemisphere. The dipole directions are not limited in any way (e.g., pointing towards the other hemispheres is not prohibited), since this would further restrict the modeled sources.

Table 6.1: The mean localization error, phase error and Combined Direction Error for case A (see Table 4.2) averaged over all simulations performed at a respective noise-factor (see section 4.2.7). Additionally, the variances as well as the minimum and maximum values of the respective parameter are given. The average GOF_{Sim} is listed.

Noise Level	Localization Error				Phase Error [rad]				Combined Direction Error (in °)				Mean GOF_{Sim}
	Mean	VAR	Min	Max	Mean	VAR	Min	Max	Mean	VAR	Min	Max	
0	0.01	0.001	0	0.12	-0.06	0.08	-0.99	0.56	22.3	822	0.06	82.3	91.0
0.1	0.02	0.002	0	0.24	-0.05	0.06	-0.99	0.45	16.9	553	0.07	73.8	83.0
0.2	0.03	0.001	0	0.12	-0.04	0.05	-0.73	0.52	20.1	673	0.08	81.3	79.2
0.3	0.04	0.002	0	0.26	-0.09	0.08	-0.99	0.57	25.8	725	0.23	82.0	75.1
0.4	0.04	0.001	0.0	0.12	-0.04	0.06	-0.94	0.49	24.0	748	0.23	81.5	73.2
0.5	0.06	0.001	0.01	0.12	-0.05	0.05	-0.85	0.28	22.7	659	0.32	89.4	71.4
0.6	0.06	0.001	0.01	0.13	-0.08	0.09	-0.92	0.60	22.3	711	0.67	87.9	68.9
0.7	0.07	0.002	0.01	0.26	-0.11	0.09	-0.99	0.40	23.6	702	0.35	89.1	67.3
0.8	0.07	0.001	0.01	0.15	-0.11	0.07	-0.88	0.42	25.1	704	0.15	86.8	65.4
0.9	0.08	0.002	0.01	0.16	-0.08	0.07	-0.77	0.53	22.4	560	0.7	78.3	65.0
1	0.09	0.002	0.02	0.16	-0.16	0.11	-0.98	0.51	25.3	733	0.4	87.9	62.8

6.1.3. **Localization, phase and direction errors: Case B**

The localization results as well as the phase- and direction error of case B (symmetric setup, equal phases during forward simulation) in respect to added white noise (see section 4.2.7) are listed in Table 6.2. As in case A, the localization error increases with the noise level. An exact localization of the dipoles is possible for noise levels up to 0.6. The maximum localization error increases with the noise.
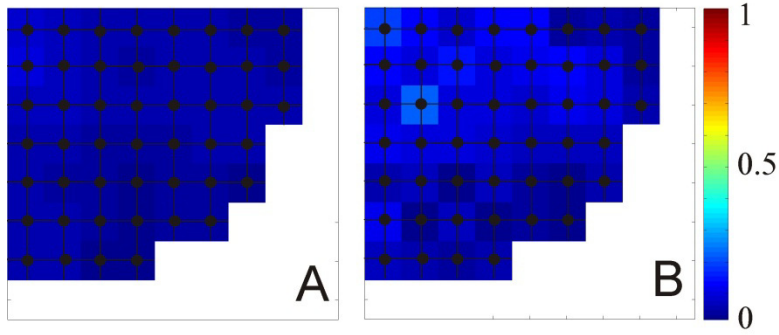

Figure 6.4: Localization error in Case B for all viable dipole positions in the simulated plane. Subfigure A shows the results for noise level 0, while subfigure B shows the results for noise level 1. The error is color encoded (see scale) and is expressed in grid points. The white area lies outside the brain shell.

The performance of the localization routine at noise level 0 is shown in subfigure A of Figure 6.4. Subfigure B shows the performance at noise level 1. At noise 0 the localization on the

symmetry axis produces zero localization errors. On the line one grid point besides the symmetry axis, the localization errors accumulate: 7 out of a total 19 localizations errors, and thus 5 out of 6 localization errors above 0.1, occur on this line. The other increased localization error occurs on the mid-coronal axis 3 grid points away from the symmetry axis.

At noise level 1, the localization error maximizes (0.28 grid points) again on the mid-coronal axis 2 and 3 grid points away from the symmetry axis. The symmetry axis itself and a border line of thickness of 1-2 grid points form a zone in which the localization errors are comparably lower than in the rest of the plane.
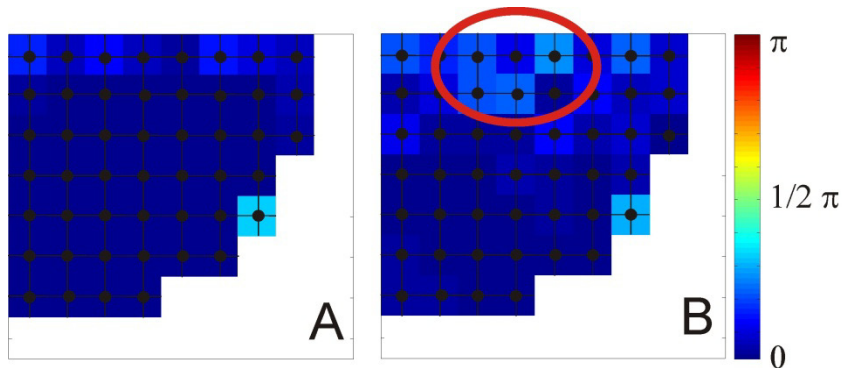

Figure 6.5: Map of the phase error in the simulated plane in case B. Subfigure A shows the results for noise level 0, while subfigure B shows the results for noise level 1. The phase error is color encoded, so that 'blue' signifies no error, while 'red' stands for a phase error of π rad. White lies outside the brain shell.

The phase reconstruction indicates a mean phase-error (calculated over the mean phases error for simulation with noise factors ranging from 0 to 1) oscillating around 0.03rad. Also the phase reconstruction variance does not exhibit a strong dependency on the noise level: at a noise level of 0 the phase error variance is 0.17, at the noise level of 1, it equals 0.24. For zero noise, the phases can be reconstructed perfectly in 39 out of 49 incidences. This number decreases to 20 out of 49 for a noise level of 1. However, 18 of the 29 erroneous reconstructions are well within the corresponding variance interval (see Table 6.2). Ten out of 11 remaining erroneous reconstructions are situated on the symmetry axis and the adjacent grid points

At noise level 0 (see Figure 6.5, Subfigure A), 7 out 10 phase reconstruction errors occur on the symmetry axis, thus for 7 out 8 grid points on the symmetry axis the phases are reconstructed with error. The Comparison to the results from noise level 1 suggests a dependency of the goodness of phase reconstruction in relation to the position in the head and the noise. It becomes obvious that sources on the symmetry axis are reconstructed with more error than in the rest of the plane.
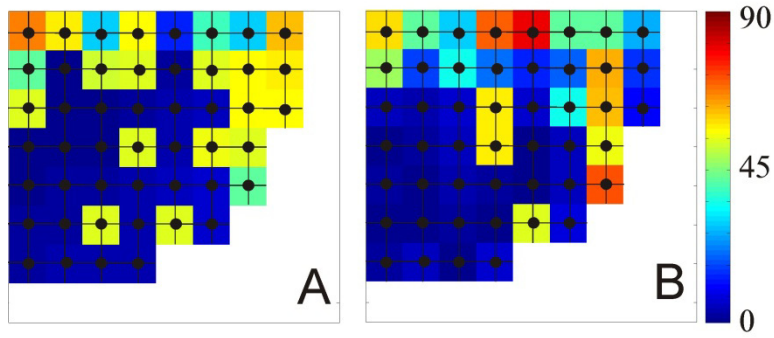
Figure 6.6: Combined Direction Error in degrees in the simulated plane in case B. Subfigure A shows the results for noise level 0, while subfigure B shows the results for noise level 1. The direction error is color encoded.

The combined error of the reconstructed direction error fluctuates around a constant level for all noise levels. The location dependent comparison of the noise levels shows for the 0 noise case 20 direction errors of around 50-60°. For the noise level 1, case this number decreases to 9, at the same time the number of direction errors of a higher degree (>60°) increases from 1 (0 noise case) to 9. Thus the amount of incorrect directions above ~50° remains on the same level. The directions of the lateral dipoles are reconstructed with little error (<20%) in both cases.

For 0 noise, 7 moderate (error 30-40°) direction errors occur on the symmetry axis towards occipital. The number of medium errors increases to 13 for a noise level of 1. Interestingly, the medium Combined Direction Errors accumulate on the symmetry axis and adjacent grid points. A band of higher error directions (>60°) separates the lateral low error (<20°) area from the central/occipital medium (50°-60°) zone (includes overlapping, see Figure 6.6, subfigure B).

Table 6.2: The mean localization error, phase error and Combined Direction Error for case B (compare Table 4.2) averaged over all simulations performed at a respective noise-factor (see section 4.2.7). Additionally the variances as well as the minimum and maximum values of the respective parameter are given. Furthermore the average GOF_{Sim} is listed.

Noise Level	Localization Error				Phase Error [rad]				Combined Direction Error (in °)				Mean GOF_{Sim}
	Mean	VAR	min	Max	Mean	VAR	Min	Max	Mean	VAR	Min	Max	
0	0.02	0.001	0	0.11	-0.01	0.17	-1.52	1.00	28.4	692	0.08	79.4	93.66
0.1	0.03	0.001	0	0.18	-0.07	0.18	-1.37	1.00	27.2	707	0.12	77.2	82.4
0.2	0.04	0.001	0	0.12	0.01	0.20	-1.56	1.26	24.9	695	0.20	81.6	76.7
0.3	0.05	0.001	0	0.15	-0.12	0.12	-1.05	0.48	27.4	724	0.23	88.1	73.0
0.4	0.05	0.002	0	0.13	0.05	0.20	-1.08	1.38	27.7	691	0.43	87.3	71.0
0.5	0.07	0.003	0	0.26	-0.01	0.25	-1.53	1.52	26.4	595	1.3	80.6	68.5
0.6	0.09	0.004	0	0.26	-0.05	0.40	-1.55	1.50	32.2	780	0.9	89.4	66.5
0.7	0.08	0.003	0.01	0.23	0.03	0.21	-1.43	1.39	27.0	690	1.1	87.0	65.1
0.8	0.09	0.003	0	0.27	-0.07	0.17	-1.46	1.48	33.9	723	1.6	81.6	63.3
0.9	0.10	0.003	0.02	0.25	-0.02	0.15	-1.51	1.03	36.8	816	0.8	87.3	61.8
1	0.11	0.004	0.02	0.28	-0.06	0.24	-1.49	1.07	31.3	669	2.0	89.3	61.9

6.1.4. **Localization, phase and direction errors: Case C**

In case C the positioning of the simulated generators is not symmetric, the asymmetry equals a shift of 1 grid point. Simulation results are listed in Table 6.3. The table shows that, in case C, the simulated generators cannot be localized exactly. This is expected since the algorithm tries to find a symmetrical solution to the asymmetric setup.

The average localization error increases with the noise from 0.06 grid points to 0.11 grid points. This increase of 0.05 grid points is approximately half the increase found for case A. However, the variances of the localization error are of a comparable magnitude for cases A and C, while case C exhibits less fluctuation of the variances along the increasing noise level.

The mean phase error averaged over noise levels 0 to 1 equals -0.042rad for case C with a corresponding variance of the mean phase error of 0.0023. Thus Case C exhibits a different behavior than Case A, which shows approximately double the average of the mean phase error (-0.80rad) and less variance (0.0017) of mean phase error. Furthermore the variance of the phase error in case C (mean of the phase error variances from noise levels 0 to 1 equals 0.065rad) is in general lower than in case A (mean of the phase error variances from noise levels 0 to 1 equals 0.074rad), but the variance of the phase error variances is lower for case A (0.00035rad) than for case C (0.00063rad).

Table 6.3: The mean localization error, phase error and Combined Direction Error for case C (compare Table 4.2) averaged over all simulations performed at a respective noise-factor (see section 4.2.7). Additionally the variances as well as the minimal and maximal values of the respective parameter are given. Furthermore the average GOF_{Sim} is listed.

Noise Level	Localization Error				Phase Error [rad]				Combined Direction Error (in °)				Mean GOF_{Sim}
	Mean	VAR	Min	Max	Mean	VAR	min	Max	Mean	VAR	Min	Max	
0	0.06	0.001	0.03	0.11	-0.00	0.04	-0.99	0.44	25.8	639	1.1	80.6	90.8
0.1	0.06	0.001	0.03	0.13	-0.03	0.05	-0.91	0.50	25.8	738	1.0	85.3	83.1
0.2	0.07	0.001	0.03	0.13	-0.06	0.04	-0.97	0.38	26.5	672	1.3	81.6	78.6
0.3	0.07	0.001	0.03	0.14	-0.04	0.05	-0.78	0.47	25.0	640	0.61	75.8	75.8
0.4	0.08	0.001	0.04	0.16	-0.07	0.06	-0.78	0.47	24.7	639	1.2	83.6	72.8
0.5	0.08	0.001	0.03	0.17	-0.01	0.05	-0.74	0.44	24.9	658	1.6	74.0	71.4
0.6	0.08	0.001	0.04	0.12	-0.03	0.09	-0.97	0.56	24.5	551	1.8	79.0	69.3
0.7	0.09	0.001	0.03	0.23	0.03	0.07	-0.96	0.52	27.5	557	1.1	77.5	71.4
0.8	0.11	0.002	0.04	0.26	-0.13	0.12	-0.99	0.46	28.4	628	1.0	82.8	71.2
0.9	0.10	0.002	0.03	0.24	-0.01	0.06	-0.75	0.52	31.3	628	1.6	80.7	68.6
1	0.11	0.002	0.04	0.24	-0.11	0.09	-0.89	0.38	24.9	676	0.6	84.3	67.7

The average of Combined Direction Error is slightly higher for case C (26.4°) than for case A (22.8°), while both cases show a similar accompanying variances of 6.5° (case A) and 6.6° (case C). The mean for the variance of the Combined Direction Error is smaller for case C (639.0°) than for case A (690.0). The obtained mean GOF_{Sim} for case C is, except for low noise levels (0 to 0.2), higher than in case A.
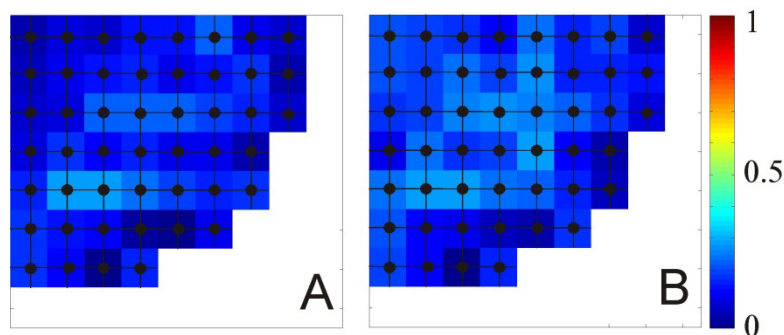
Figure 6.7: Localization error in Case C for all viable dipole positions in the simulated plane. Subfigure A shows the results for noise level 0, while subfigure B shows the results for noise level 1. The error is color encoded (see scale) and is expressed in grid points. The white area lies outside the brain shell.

The left hand side of Figure 6.7 shows the localization error for grid points in the simulated plane for the 0 noise case, while the right hand side displays results for a noise level of 1. For a noise level of 0 the localization error does not reveal dependency on the location in the plane. For the elevated noise level 1 in case C, the localization routine yields the best results for the grid points at the brain shell border and the lateral region. Comparably low is the localization error at the occipital end of the symmetry axis. The localization error increases for grid points deeper in the simulated brain; however the simulations in case C do not reveal any area in which the localization errors accumulate.

Figure 6.8: Map of the phase error in the simulated plane in case C. Subfigure A shows the results for noise level 0, while subfigure B shows the results for noise level 1. The phase error is color encoded, so that 'blue' signifies no error, while 'red' stands for a phase error of π rad. The red circle marks the zone of highest phase error. White lies outside the brain shell.

The mean phase error fluctuates around an average error of -0.042rad. At zero noise the phases are reconstructed with an error of 0 for 37 out of 49 times. The inaccurate phase reconstructions accumulate on the symmetry axis. At noise level 1, the number of correct phase reconstruction has decreased to 30. In this case, the phase reconstruction error is pronounced at the midsagittal plane and decreases with the distance thereof. For several grid points on the symmetry axis and the adjacent row, the simulations yield a region (see red circle in Figure 6.8, subfigure B) containing phase error of comparably high magnitude. It is located similar to the zone of elevated and concentrated phases errors found for case A (see subfigure B in Figure 6.2), which suggests an identical underlying cause.
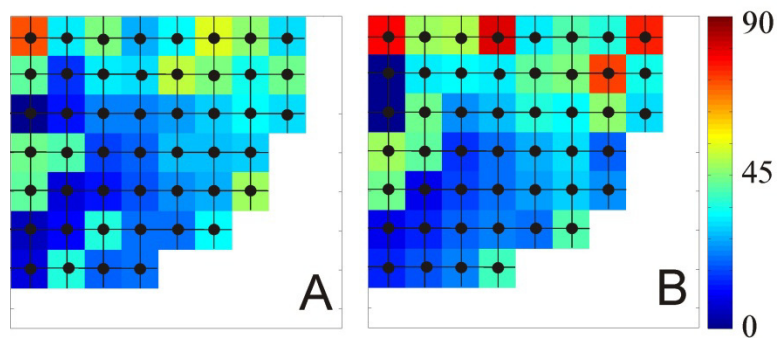
58

Figure 6.9: Combined Direction Error in degrees in the simulated plane in case C. Subfigure A shows the results for noise level 0, while subfigure B shows the results for noise level 1. The direction error is color encoded.

The Combined Direction Error fluctuates around a constant level for all noise levels. For the noise level zero, the directions are reconstructed with the highest error (40°-60°) on the symmetry axis plus the adjacent grid points and the occipital region of the brain shell (see subfigure A in Figure 6.9). For the rest of the plane, the directions are reconstructed with an error of less than 15°. Reconstruction error between 15° and 40° occurs at only 2 positions. For the noise level 1, the reconstruction error of directions are concentrated similar to the noise level zero on the symmetry axis and the occipital region of the brain shell, forming a region of low direction reconstruction error at the lateral region of the brain shell (see subfigure B in Figure 6.9). However, the error magnitudes are distributed differently: at noise level zero the interval of high error was in the close range from 40° to 60°, at noise level 1 the range increases to an interval from 40° to 90°. Most prominent are the high reconstruction errors in the occipital region and the middle of the symmetry axis (see subfigure B in Figure 6.9). The later region is identical to the region that produces high phase reconstruction error at noise level 1 (compare subfigures B in Figure 6.8 and Figure 6.9). This noise dependent behavior of the direction reconstruction is similar to case A, which again suggests identical underlying cause in both cases.

6.1.5. **Localization, phase and direction errors: Case D**

Case D uses different models for the simulation and the inverse solution. A symmetrical setup of dipoles with a phase difference of 1rad is set up. Table 6.4 shows the concurrent statistics. Albeit the average localization error starts on a comparatively high level and also exhibits a dependency on noise, the variance of the localization error is independent of the simulated noise levels. The localization error at noise level zero in case C (0.18 grid points) is considerably higher than the localization error at noise level 1 for case A (0.11). The same holds for a comparison between the variance of the localization error of the mentioned cases. The minimum as well as the maximum reconstruction errors are also independent of the noise level in the simulated range.

The mean phase error fluctuates around an average error of 0.03rad, while the phase error variance fluctuates around 0.11. Note however, that -independent of the noise- in only 10-12 cases out of 49 the phase can be reconstructed with an error of 0.

The combined error of the reconstructed direction error fluctuates around a constant level for all noise levels. For case D, the GOF_{Sim} decreases with an increase in the noise.

Table 6.4: The mean localization error, phase error and Combined Direction Error for case D (compare Table 4.2) averaged over all simulations performed at a respective noise-factor (see section 4.2.7). Additionally the variances as well as the minimum and maximum values of the respective parameter are given. Furthermore the average GOF_{Sim} is listed.

Noise Level	Localization Error				Phase Error [rad]				Combined Direction Error (in °)				Mean GOF_{Sim}
	Mean	VAR	Min	Max	Mean	VAR	Min	Max	Mean	VAR	Min	Max	
0	0.18	0.004	0.06	0.33	0.04	0.12	-0.70	0.75	0.18	0.003	0.06	0.33	82.8
0.1	0.18	0.004	0.05	0.33	-0.03	0.10	-0.76	0.67	0.18	0.003	0.06	0.33	76.4
0.2	0.18	0.004	0.06	0.33	0.03	0.09	-0.54	0.66	0.18	0.004	0.05	0.33	73.4
0.3	0.19	0.004	0.05	0.33	-0.09	0.12	-0.75	0.69	0.19	0.004	0.06	0.32	71.1
0.4	0.18	0.003	0.06	0.33	0.11	0.09	-0.64	0.70	0.18	0.003	0.06	0.32	69.2
0.5	0.19	0.004	0.05	0.33	0.04	0.11	-0.77	0.74	0.19	0.004	0.05	0.33	67.3
0.6	0.19	0.003	0.06	0.31	0.10	0.10	-0.63	0.74	0.19	0.003	0.06	0.31	65.9
0.7	0.19	0.004	0.06	0.30	0.14	0.14	-0.53	0.71	0.19	0.004	0.06	0.30	65.0
0.8	0.20	0.004	0.05	0.31	0.09	0.11	-0.71	0.74	0.20	0.004	0.05	0.31	62.2
0.9	0.21	0.004	0.05	0.32	-0.03	0.12	-0.75	0.61	0.21	0.004	0.05	0.32	60.6
1	0.21	0.004	0.05	0.31	-0.00	0.10	-0.65	0.77	0.21	0.004	0.05	0.31	60.2

Subfigure A in Figure 6.10 shows the distribution of the localization error in the zero noise case, while subfigure B represents the case at noise level 1. For noise level 0 the distribution of the localization error is low in the center and the border of the brain shell. Between the zones of relative low error, especially towards the lateral border, the error is elevated above the mean localization error. For noise level 1, the localization error is lowest at the brain shell border, which includes the occipital region. The localization error for sources on the symmetry axis is on the level of the mean localization error. Again, the area between the center and the border of the brain shell exhibits the highest localization error in the simulation plane.

Figure 6.10: Localization error in Case D for all viable dipole positions in the simulated plane. Subfigure A shows the results for noise level 0, while subfigure B shows the results for noise level 1. The error is color encoded (see scale) and is expressed in grid points. The white area lies outside the brain shell.

The phase error of case D at zero noise (see Figure 6.11) is elevated in area of 3-by-3 grid points on and close to the symmetry axis (see subplot A). Additional four positions on the brain shell border produce strong phase error (~0.74rad). These positions exhibit a strong phase reconstruction error also for higher noise levels, as Subfigure B shows for noise level 1. Also the occipital region and the symmetry axis show high phase reconstruction error. Thus, the positions of high localization error and high phase reconstruction error are different. Additionally, the area of accumulated phase reconstruction error in case D and noise level of 0 agrees with the ones identified for the cases A and C. For higher noise levels this area persists.
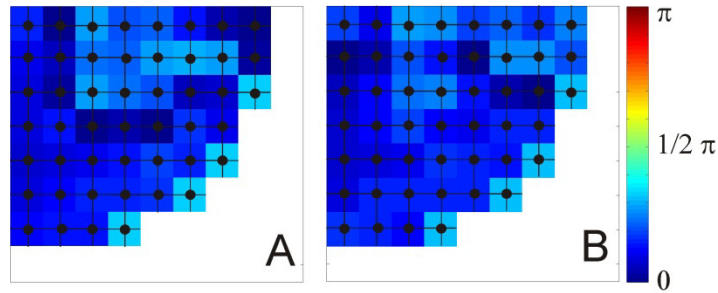
Figure 6.11: Map of the phase error in the simulated plane in case D. Subfigure A shows the results for noise level 0, while subfigure B shows the results for noise level 1. The phase error is color encoded, so that 'blue' signifies no error, while 'red' stands for a phase error of π rad. White lies outside the brain shell.

As the mean Combined Direction Error shows little dependency on the noise for the analyzed noise level interval, also the distribution of the error follows the same pattern for low and high noise levels. Figure 6.12, subplot A shows the distribution in the zero noise case. The direction error is pronounced on the symmetry axis and the occipital region. From the described positions, the Combined Direction Error gradually decreases towards the midcoronal plane. For elevated noise levels (for noise level 1 see subfigure B) the zone of high direction error extends towards the midcoronal plane. In both cases the centre of the brain shell reveals a direction error of more than 70°. Additionally, for the elevated noise levels more grid points show (maximum value 3) a direction reconstruction error above 70°. They are found on the symmetry axis and in the occipital region.

Figure 6.12: Combined Direction Error in degrees in the simulated plane in case D. Subfigure A shows the results for noise level 0, while subfigure B shows the results for noise level 1. The direction error is color encoded.

In this case the reconstruction of the direction differs from cases A-C and E. While the general structure (error increases with proximity to symmetry axis and occipital region) is still present, the average level of error is increased. An additional difference is the increased reconstruction error at the midcoronal plane.

6.1.6. **Localization, phase and direction errors: Case E**

In case E the simulated symmetric dipoles possess a phase difference of 1 rad, however the fixed phase TMP-approximation applied for solving the inverse solution does not reproduce the phases of the simulated channels. The TMP parameters approximating the simulated values therefore are not optimal and thus introduce an error into the second step of the source localization algorithm. The dipole fit on the other hand explicitly allows for 2 dipoles of independent phases in the reconstruction. As in case B, the localization error increases with the noise level. An exact localization of the dipoles is possible for noise levels up to 0.4 (see Table 6.5, identical to case A). The mean localization error increases with noise. Compared to case A, the mean localization error is 0.01 to 0.02 points stronger in case E. The variance of localization error in case E is on the same level as in case A for lower noise levels, but rises above case A for noise levels 0.9 and 1.

Table 6.5: The mean localization error, phase error and Combined Direction Error for case E (compare Table 4.2) averaged over all simulations performed at a respective noise-factor (see section 4.2.7). Additionally the variances as well as the minimum and maximum values of the respective parameter are given. Furthermore the average GOF_{Sim} is listed.

Noise Level	Localization Error				Phase Error [rad]				Combined Direction Error (in °)				Mean GOF_{Sim}
	Mean	VAR	Min	Max	Mean	VAR	Min	Max	Mean	VAR	Min	Max	
0	0.02	0.001	0	0.11	-0.82	0.11	-1.00	-0.10	28.4	692	0.1	79.4	92.8
0.1	0.03	0.001	0	0.18	-0.78	0.18	-1.00	0.55	27.2	707	0.1	77.2	82.3
0.2	0.04	0.001	0	0.11	-0.75	0.19	-1.00	0.55	34.9	695	0.2	81.6	75.7
0.3	0.05	0.001	0	0.11	-0.88	0.07	-1	-0.12	27.4	724	0.2	88.1	72.4
0.4	0.05	0.001	0	0.13	-0.84	0.11	-1	0.48	27.7	691	0.4	87.3	70.3
0.5	0.06	0.001	0.01	0.14	-0.95	0.03	-1.00	-0.18	26.4	595	1.3	80.6	68.5
0.6	0.07	0.002	0.01	0.21	-0.79	0.12	-1.00	0.41	32.2	780	0.9	89.4	65.9
0.7	0.07	0.002	0.01	0.16	-0.87	0.09	-1.00	0.40	27.0	690	1.1	87.0	65.2
0.8	0.09	0.002	0.02	0.22	-0.87	0.09	-1.00	0.38	33.9	723	1.6	81.6	63.0
0.9	0.10	0.003	0.03	0.23	-0.82	0.16	-1.00	0.56	36.8	816	0.8	87.3	61.6
1	0.11	0.003	0.02	0.24	-0.89	0.08	-1	0.25	31.3	669	2.0	89.3	61.9

The phases of the simulated dipoles are reconstructed with an error of around -0.84rad. Thus, on average, the dipoles are reconstructed with a (mean) phase difference of 0.16rad, although the TMP approximation does not allow for any phase difference in the approximated channels in this case. Compared to case B (symmetric setup, equally phased simulated dipoles) the mean phase errors are elevated for all noise levels (except noise level 1) in case E. This suggests that fixed-phase TMP-approximation introduces an additional

error or bias to the phase reconstruction (and potentially localization) by approximating more of the signal energy on one hemisphere.

The Combined Direction Error fluctuates around a constant level for all noise levels. For case C, the GOF_{Sim} decreases with an increase in the noise.

Subfigure A in Figure 6.13 shows the distribution of the localization error on the simulated plane for noise level 0 for case E. No accumulations of localization error occur, however the localization is best at the border of the brain shell and the symmetry axis. The single grid point for which the localization error is increased (center of the section of the midcoronal axis) shows an analogy to case B (compare Figure 6.4 subfigure B). At a noise level of 1 (subfigure B in Figure 6.13) the overall localization error has increased, however the localization is best at the brain shell border. Also here a high localization error is found on the midcoronal axis. The localization error in the occipital region of the brain shell remains below 0.1 grid points.
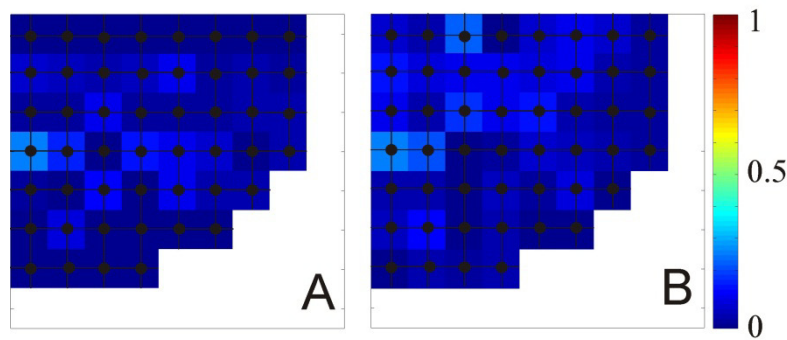
Figure 6.13: Localization error in Case E for all viable dipole positions in the simulated plane. Subfigure A shows the results for noise level 0, while subfigure B shows the results for noise level 1. The error is color encoded (see scale) and is expressed in grid points. The white area lies outside the brain shell.

Subfigure A in Figure 6.14 shows the distribution of the phase reconstruction error for the noise level 0 in case E. At 12 grid points, the phase reconstruction error does not amount to the expected -1rad. 7 out of the 12 incidences occur directly on the symmetry axis or on the adjacent grid points. The remaining 5 errors are positioned towards the lateral border of the brain shell. This distribution of phase reconstruction error on the analyzed plane is similar to the results for noise levels 0 and 1 in case B.
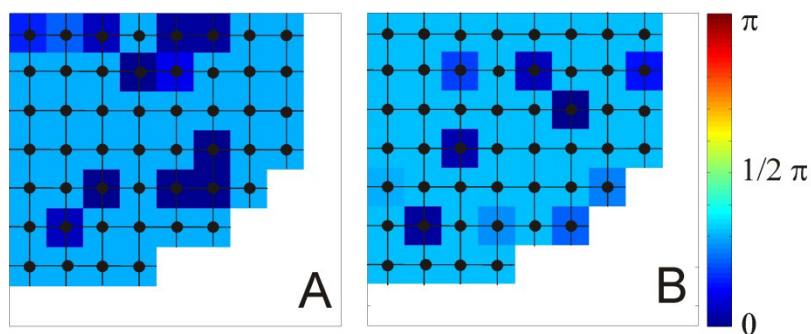
Figure 6.14 Map of the phase error in the simulated plane in case E. Subfigure A shows the results for noise level 0, while subfigure B shows the results for noise level 1. The phase error is color encoded, so that 'blue' signifies no error, while 'red' stands for a phase error of π rad. White lies outside the brain shell.

At noise level 1 (see subfigure B in Figure 6.14) the grid points producing phase reconstruction errors are more randomly distributed: hence, none of the 10 flawed phase reconstructions can be found on the symmetry axis. An inspection across the different noise levels reveal that the phase error is concentrated in the interval ranging from -1 rad to -0.95 rad at 34 44 out of 49 grid points. The degree of phase error is randomly distributed between -0.949rad and +0.6rad for the remaining grid points.

The distribution of the Combined Direction Error on the plane reveals an area of high error in the occipital region and steep gradient towards a region of low error at the mid coronal axis for a noise level of 0 (see subfigure A in Figure 6.15). The highest error occurs in the occipital region of the brain shell on the symmetry axis and the adjacent grid points. At 21 out of 49 grid points the direction can be reconstructed with an error below 15°. For elevated noise levels (noise level 1 see subfigure B in Figure 6.15) another area of high noise forms on the midcoronal axis towards the lateral border. The occurrences of high Direction Error shift towards the center of the analyzed quarter plane and the center of the brain shell. A good reconstruction of the direction (error below 15°) is possible in 12 cases.
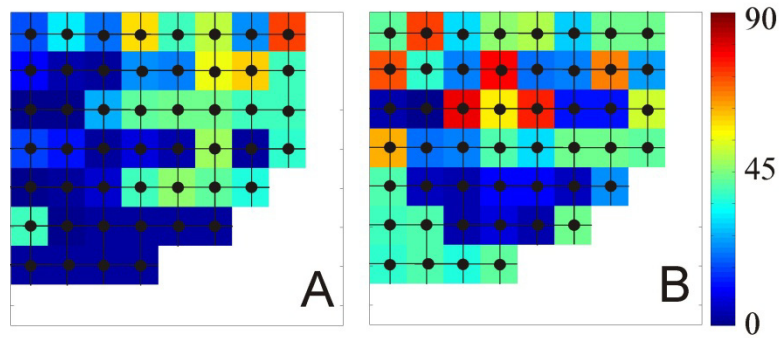
Figure 6.15: Combined Direction Error in degrees in the simulated plane in case E. Subfigure A shows the results for noise level 0, while subfigure B shows the results for noise level 1. The direction error is color encoded.

6.2. **Application to measured EEG-data**

6.2.1. **TMP-parameter: modulation ξ**

As described in section 4.2.5, the data are approximated by TMP-atoms. The modulation parameter ξ relates to the (main) frequency of the atom and thus the analyzed signal. Table 6.6 lists the modulation ξ expressed as frequency in Hz for the TMP-approximation for the subjects in relation to the stimulation frequencies presented as multiples of the individual alpha.

Table 6.6: Modulation parameter ξ in [Hz] of the TMP approximation itemized for the subjects and their stimulation frequency given as multiple of the individual alpha frequency (0.4*alpha – 1.6*alpha). The modulation parameter ξ for 0.5*alpha yields results similar to 1*alpha.

ξ	0.4	0.45	0.5	0.55	0.6	0.7	0.8	0.9	0.95	1	1.05	1.1	1.2	1.4	1.6
Subject 1	7.8	8.2	10.2	7.8	6	6.9	8.3	9.2	9.4	9.9	10.4	11.1	12.8	13.9	16
Subject 2	4.3	5.5	10	5.3	5.8	7.5	9.4	10	9.6	9.8	10.2	10.6	11.6	14.1	15.6
Subject 3	5	5.1	10.2	10.3	6.3	7.8	8.7	9.8	10	10.4	11.4	11.6	13.1	15.7	16.7
Subject 4	8	4.8	8.5	5.6	5.9	6.7	7.8	8.6	9.3	9.4	10.5	10.4	11.4	16.2	15.2
Subject 5	5.8	7.5	10.6	5.5	6	7.4	7.9	9.7	9.5	10	10.4	11.1	11.9	14.8	16.7
Subject 6	8.3	9.6	10	10.1	11.5	16	19	10.9	11.2	11.7	11.6	12.2	13.3	15.6	17.9
Subject 7	9.1	4.8	10.4	7.1	6.5	7.2	8.2	9.3	9.8	10.5	11.3	12	12.5	14.3	16.7
Subject 8	14	4.2	10.8	13.9	17.4	7.5	17	13.7	10.6	11.1	11.1	11.6	13.3	14.7	17.2
Subject 9	5.1	14.2	11.9	13	9.5	10	8.6	10.8	10.4	11.6	11.7	12	13.3	15.2	17.2
Subject 10	7.5	5.3	9.9	7.1	7	11.6	10.8	11	11.8	11.9	13.1	13.5	14.8	16.7	20.2

Please note that the mean response frequency at the stimulation with 1*alpha equals the alpha frequency of the respective subject, in so far that differences do not exceed 0.1 Hz. Table 6.7 lists the response frequencies standardized to the alpha frequencies of the respective subject.

Table 6.7: The estimated modulation parameter ξ standardized to the individual alpha frequency of a subject. Stimulation frequency is given as multiple of the individual resting alpha. Except for 3 subjects, the results for 0.5*alpha are close to 1*alpha.

Normalized ξ	0.4	0.45	0.5	0.55	0.6	0.7	0.8	0.9	0.95	1	1.05	1.1	1.2	1.4	1.6
Subject 1	0.79	0.83	1.03	0.79	0.61	0.70	0.84	0.93	0.95	1	1.05	1.12	1.29	1.40	1.62
Subject 2	0.44	0.56	1.02	0.54	0.59	0.77	0.96	1.02	0.98	1	1.04	1.08	1.18	1.44	1.59
Subject 3	0.48	0.49	0.98	0.99	0.61	0.75	0.84	0.94	0.96	1	1.10	1.12	1.26	1.51	1.61
Subject 4	0.85	0.51	0.90	0.6	0.63	0.71	0.83	0.91	0.99	1	1.12	1.11	1.21	1.72	1.62
Subject 5	0.58	0.75	1.06	0.55	0.6	0.74	0.79	0.97	0.95	1	1.04	1.11	1.19	1.48	1.67
Subject 6	0.63	0.45	0.83	0.6	0.59	1.01	0.92	0.92	0.99	1	1.10	1.13	1.24	1.40	1.70
Subject 7	0.87	0.46	0.99	0.68	0.62	0.69	0.78	0.89	0.93	1	1.08	1.14	1.19	1.36	1.59
Subject 8	1.26	0.38	0.97	1.25	1.57	0.68	1.53	1.23	0.95	1	1.00	1.05	1.20	1.32	1.55
Subject 9	0.44	1.22	1.03	1.12	0.82	0.86	0.74	0.93	0.90	1	1.01	1.03	1.15	1.31	1.48
Subject 10	0.63	0.45	0.83	0.6	0.59	0.97	0.91	0.92	0.99	1	1.1	1.13	1.24	1.4	1.7
Mean	0.7	0.63	0.98	0.79	0.74	0.77	0.91	0.97	0.96	1	1.06	1.1	1.21	1.44	1.6
Variance	0.07	0.07	0.03	0.07	0.09	0.01	0.05	0.01	0.00	0	0.00	0.00	0.00	0.01	0.00

For the stimulation frequency of 0.5*alpha the standardized modulation parameter ξ of the TMP atoms is close to 1 and possesses a small variance of 0.03 (see Figure 6.16). In contrast to all other responses, the 0.5*alpha response thus is double the stimulation frequency. Furthermore the mean response frequency for 0.9*alpha and 0.95*alpha are close to 1 and have low variance values. Notable outliers exist (i.e.: values outside the interval defined by the mean plus twice the standard deviation of a column.) and lead to a comparatively high value for the mean at the stimulation frequency 0.8*alpha (see subject 8 at 0.8*alpha).
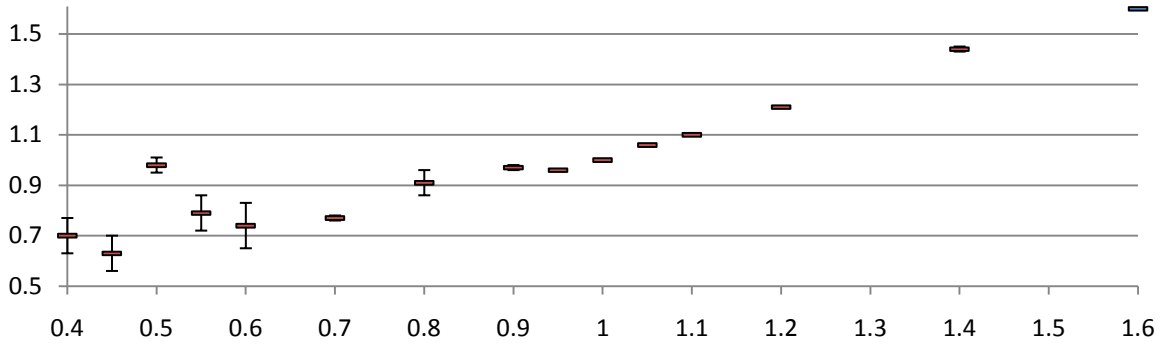
Figure 6.16: Mean (red) and variance (black T-shapes) values (according to Table 6.7) of the standardized modulation parameter ξ (y-axis) plotted versus the stimulation frequencies (individual alpha multiple, y-axis).

6.2.2. Localization

The localization algorithm localizes mirrored dipoles for each subject and each stimulation frequency. For each subject I choose the stimulation frequency 1*alpha as reference point since this is where the strongest alpha activity is detected. In the topographic analysis (see section 4.1) this is explained in more detail. The activity obtained at 1*alpha is located occipital towards the border of the brain shell. The localization is equivalent to area 17 in the cortex (see Figure 6.17).
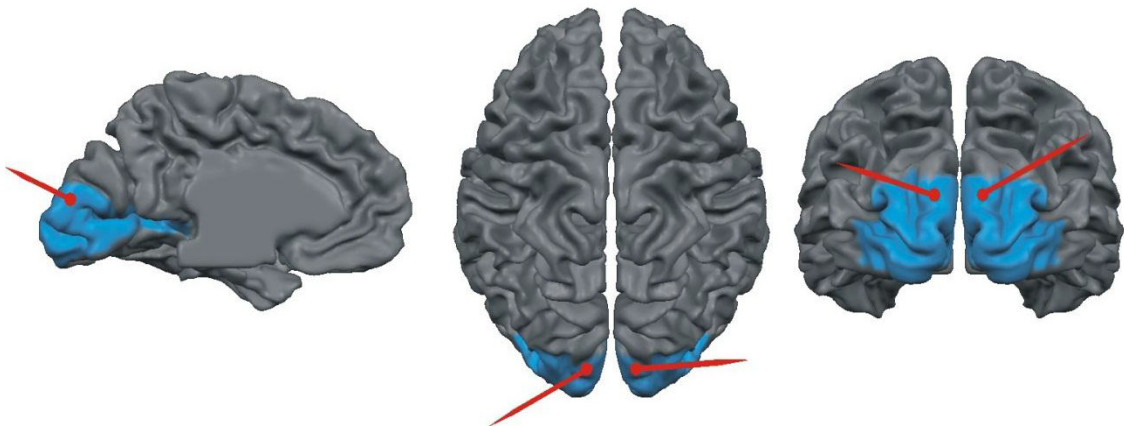
Figure 6.17: Localization of the 1*alpha component in area 17 (highlighted in blue) in the occipital region. Left: mid sagittal view of the left hemisphere; Mid: top view; Right: occipital view. In this illustrative example the localized dipole positions and directions of the mirrored Dipole Atoms (Red arrows) are reproduced for the same subject as in Figure 5.1. The dipoles are localized in area 17 and mirrored at the midsagittal plane. The according directions are not symmetric.

Next, the Euclidean distance was calculated subject-wise between the 1*alpha reference dipole and dipoles localize for the other frequencies. Table 6.8 lists the results, but does not include the values for 1*alpha as they are equal to zero, therefore they don't contain any valuable information.

Table 6.8: The distances of the reconstructed dipoles of each subject to the according reconstructed dipoles at 1*alpha. The values for 1*alpha are equal to zero and therfore not listed. The mean in the right-most column indicates the rounded mean of the intra-individual distances. Subjects highlighted are excluded from further investigation.

Stimulation	0.4	0.45	0.5	0.55	0.6	0.7	0.8	0.9	0.95	1.05	1.1	1.2	1.4	1.6	Mean
Subject 1	0.19	0.38	0.25	0.18	0.3	0.44	0.13	0.39	0.28	0.13	0.08	0.17	0.34	0.44	0.26
Subject 2	0.21	0.07	0.09	0.33	0.25	0.35	0.24	0.22	0.13	0.13	0.04	0.27	0.37	0.41	0.22
Subject 3	0.26	0.12	0.06	0.23	0.26	0.36	0.59	0.2	0.12	0.05	0.39	0.18	0.26	0.31	0.24
Subject 4	0.13	0.16	0.01	0.01	0.31	0.11	0.1	0.13	0.02	0.16	0.23	0.26	0.19	0.19	0.14
Subject 5	0.23	0.99	0.2	0.92	0.15	0.86	0.06	0.04	0.15	0.01	0.22	0.06	0.18	0.17	0.3
Subject 6	0.79	0.76	0.68	0.85	0.89	0.81	0.86	0.67	0.45	1.29	0.2	0.89	0.71	0.71	0.75
Subject 7	0.31	0.25	0.06	0.3	0.14	0.24	0.34	0.93	0.08	0.24	0.13	0.16	0.23	0.25	0.26
Subject 8	0.4	0.56	0.36	0.5	0.53	0.42	0.42	0.07	0	0.36	0.14	0.21	0.24	0.24	0.32
Subject 9	1.27	0.35	0.34	0.34	0.36	0.16	1.27	0.04	0.45	0.31	0.49	0.32	0.55	0.33	0.47
Subject 10	0.32	0.59	1.36	0.22	0.9	0.37	1.11	0.99	1.04	0.26	0.2	0.08	0.23	0.35	0.57
Mean	0.41	0.42	0.34	0.39	0.41	0.41	0.51	0.37	0.27	0.29	0.21	0.26	0.33	0.34	0.35
Variance	0.12	0.09	0.17	0.08	0.08	0.06	0.19	0.13	0.1	0.13	0.02	0.06	0.03	0.02	0.04

The mean values of the Euclidean dipole distances of and the according variances are plotted in Figure 6.18. No immediate apparent distinction can be made here. However, this statistics comprises two types of subjects, the first type shows alpha entrainment, while the second does not. Section 6.2.3 separates the two types.
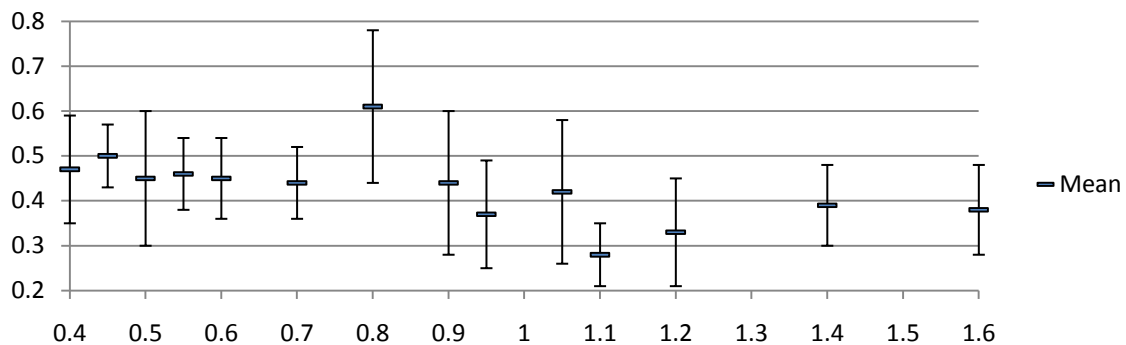
Figure 6.18: Mean and variance of the Euclidean distances between the diploes at 1*alpha and the stimulation frequencies shown (the alpha multiples of the stimulation are on the x-axis, while the distances are on the y-axis).

6.2.3. **Allocation of 0.5*alpha**

Motivated by the findings regarding the modulation parameter ξ at 0.5*alpha (see Figure 6.16), the localization results of this stimulation frequency require a more detailed examination. I test if dipole locations obtained from stimulation with 0.5*alpha are on

average similar to the locations from the group of frequencies ranging from 0.9*alpha to 1.1*alpha named *alpha-group* in the following. Afterwards it is verified that 0.5*alpha does not belong to the group of stimulation frequencies ranging from 0.4*alpha to 0.8*alpha (excluding 0.5*alpha) and 1.2*alpha to 1.6*alpha, termed *no-alpha-group*. The distinction between the stimulation frequency groups is sketched in the topographic analysis in section 5.2. The topographic analysis in section 5.2.2 suggests that 3 subjects do not show sufficient alpha entrainment, which is in accordance with the literature (Lazarev 2001) and (potentially) leads to two groups for the subjects: an *entrainment-group* (EG) and a *no-entrainment-group* (NEG).

First, it is tested if 1 or more subjects differ(s) from the remaining subjects in respect to the Euclidean distance between the dipole at 1*alpha and other stimulation frequencies. The distance values for 1*alpha are ignored at this step and the following steps, since 1*alpha is the reference point for the distance calculation. For each subject, the mean of the distances is calculated (see Table 6.8). From this mean, the mean of the means ($Mean2$) and the Standard Deviation of the means STD_{M2} is computed. Subsequently, the 85% confidence interval is determined for the given distribution of 10 values, for 9 degrees of freedom the confidence interval around $Mean2$ ranges from $Mean2 - 1.099 * STD_{M2}$ to $Mean2 + 1.099 * STD_{M2}$. Based on the values given in Table 6.9, subjects 4, 6 and 10 (highlighted in Table 6.8) are removed from further investigation on a 15% significance level.

Table 6.9: The mean of dipole distance means (denoted $Mean2$) and the standard deviation of the dipole distance means (STD_{M2}) as well as the limits of the interval $Mean2 - 1.099 * STD_{M2}$ and $Mean2 + 1.099 * STD_{M2}$.

$Mean2$	STD_{M2}	1.099*STD_{M2}	$Mean2$-1.099*STD_{M2}	$Mean2$+1.099*STD_{M2}
0.355	0.187	0.206	0.149	0.561

For further investigation the data is split in two groups defined by the stimulation frequency: *no-alpha-group* and *alpha-group* (see Table 6.10 for the *no-alpha-group* and Table 6.12 for the *alpha-group*). The stimulation frequency 0.5*alpha is so far assumed to not belong to any group. Table 6.10 lists the Euclidean distances of the remaining subjects for the no-alpha-group as well as the mean values for each stimulation frequency across subjects.

Table 6.10: Euclidean distances between the reconstructed dipoles of each subject of the entrainment group and the according dipoles at 1*alpha for the *no-alpha-group* of stimulation frequencies. The listed data here are a subgroup of Table 6.8 and exclude subject 4, 6 and 10. Also the stimulation frequencies 0.5, 0.9, 0.95, 1.05 and 1.1*alpha are excluded. The distance mean in this table is calculated from the subgroup of subjects.

Stimulation	0.4	0.45	0.55	0.6	0.7	0.8	1.2	1.4	1.6
Subject 1	0.19	0.38	0.18	0.3	0.44	0.13	0.17	0.34	0.44
Subject 2	0.21	0.07	0.33	0.25	0.35	0.24	0.27	0.37	0.41
Subject 3	0.26	0.12	0.23	0.26	0.36	0.59	0.18	0.26	0.31
Subject 5	0.23	0.99	0.92	0.15	0.86	0.06	0.06	0.18	0.17
Subject 7	0.31	0.25	0.3	0.14	0.24	0.34	0.16	0.23	0.25
Subject 8	0.4	0.56	0.5	0.53	0.42	0.42	0.21	0.24	0.24
Subject 9	1.27	0.35	0.34	0.36	0.16	1.27	0.32	0.55	0.33
Distance Mean	0.41	0.39	0.4	0.28	0.4	0.44	0.2	0.31	0.31

Next it is tested if 0.5*alpha belongs to the *no-alpha-group* described in Table 6.10. The mean of distance means (MDM_{nag}, subscript *nag* relates to *no-alpha-group*) across stimulation frequencies and the according standard deviation (STD_{nag}) are calculated. For 9 samples and thus 8 degrees of freedom the 90% confidence interval ranges from $MDM_{nag} - 1.397 * STD_{nag}$ until $MDM_{nag} + 1.397 * STD_{nag}$. The corresponding values as well as the mean value for 0.5*alpha are listed in Table 6.11.

Table 6.11: The mean of Euclidean dipole distance means (MDM_{nag}) of the *no-alpha-group*, its standard deviation and the 90% confidence interval. Additionally the mean value for 0.5*alpha is given.

MDM_{nag}	STD_{nag}	$1.397 * STD_{nag}$	$MDM_{nag} - 1.397 * STD_{nag}$	$MDM_{nag} + 1.397 * STD_{nag}$	Mean 0.5*alpha
0.349	0.078	0.109	0.240	0.460	0.194

Table 6.11 states that, at the 10% significance level, the stimulation frequency 0.5*alpha does not belong to the compared group. However, it is notable that the stimulation frequency of 1.2*alpha does not belong to this group either (again at the 10% significance level); it is therefore highlighted in Table 6.10.

Next it is checked if the distances obtained at 0.5*alpha and 1.2*alpha fall into the same group as distances in the proximity to the reference 1*alpha (Table 6.12).

Table 6.12: Euclidean distances between the reconstructed dipoles of each subject of the entrainment group and the according dipoles at 1*alpha for the *alpha-group* (of frequencies). Additionally the values for 1.2*alpha are listed. Also this table lists a subset of data from Table 6.8. Subjects 4, 6 and 10 are excluded; the distance mean is calculated for the presented subset of subjects.

Stimulation	0.9	0.95	1.05	1.1	0.5	1.2
Subject 1	0.39	0.28	0.13	0.08	0.25	0.17
Subject 2	0.22	0.13	0.13	0.04	0.09	0.27
Subject 3	0.2	0.12	0.05	0.39	0.06	0.18
Subject 5	0.04	0.15	0.01	0.22	0.2	0.06
Subject 7	0.93	0.08	0.24	0.13	0.06	0.16
Subject 8	0.07	0	0.36	0.14	0.36	0.21
Subject 9	0.04	0.45	0.31	0.49	0.34	0.32
Distance mean	0.27	0.1729	0.1757	0.2129	0.1943	0.2

The procedure is the same as in the previous step. First, the mean of means (MDM_{ag}, subscript *ag* relates to *alpha-group*) and the standard deviation (STD_{ag}) of means are calculated for the *alpha-group*. For four values and thus 3 degrees of freedom the 87% confidence interval is given by $MDM_{ag} - 1.385 * STD_{ag}$ and $MDM_{ag} - 1.385 * STD_{ag}$. The corresponding values are listed in Table 6.13.

Table 6.13: The mean of Euclidean dipole distance means (MDM_{ag}) of the *alpha-group* the according standard deviation and the 87% confidence interval is listed.

MDM_{ag}	STD_{ag}	$1.385 * STD_{ag}$	$MDM_{ag} - 1.385 * STD_{ag}$	$MDM_{ag} + 1.385 * STD_{ag}$
0.208	0.045	0.063	0.145	0.271

According to the respective mean values, it can be assumed, at 13% significance level, that the distances to the reference obtained for the stimulation frequencies 0.5*alpha and 1.2*alpha belong to the *alpha-group*.

6.2.4. **Phase results**

The TMP-based algorithm estimates the difference of phases $\phi_{DA} - \phi_{DA.Mirr}$ between the two reconstructed dipoles. Table 6.14 contains the estimated phase differences for all subjects and stimulation frequencies.

Table 6.14: Difference $\phi_{DA} - \phi_{DA.Mirr}$ between the phase parameters of the mirrored dipoles in rad.

Stimulation	0.4	0.45	0.5	0.55	0.6	0.7	0.8	0.9	0.95	1	1.05	1.1	1.2	1.4	1.6
Subject 1	0.05	0.01	0.18	0.08	0.04	0.2	0.42	0.07	0.05	0.06	0.01	0.74	0.01	0.24	0.1
Subject 2	0.01	0.2	0.05	0.3	0.02	0.05	0.32	0.04	0.22	0.34	0	0.01	0.13	0.01	0.04
Subject 3	0.01	0.01	0.02	0.03	1.15	0.17	0.01	0.27	0.26	0.2	0.28	0.54	1.39	0.13	0.14
Subject 4	0.15	0.02	1.45	0.6	0.4	0.16	0.08	0.95	0.34	0.47	0.4	0.59	0.88	1.02	0.06
Subject 5	0.17	0.43	0.2	0.13	0.01	0.6	0.02	0.41	0.26	0.4	0.33	0.51	0.05	0.04	0.18
Subject 6	0.03	0.15	0.06	0.01	0	0.27	0.01	0.29	0.27	0.86	0.63	1.51	1.55	0.08	0.13
Subject 7	0.14	0.04	0.01	0.75	0.34	0.53	0.82	0.32	0.35	0.06	0.04	0.99	1.23	0.32	0.07
Subject 8	0.35	0.07	0.18	0.02	0.06	0.01	0.46	0.39	0.3	0.13	0.08	0	0.04	0.37	1.06
Subject 9	0.05	0.3	0.54	0.37	0.54	0.91	0.05	0.24	0.01	0.19	0.9	0.42	0.14	0.21	0.23
Subject 10	0.25	0.12	0.84	0.08	0.1	0.95	0.5	0.15	0.19	0.85	0.71	0.03	0.01	0.28	0.48
Phase Mean	0.12	0.14	0.35	0.24	0.27	0.39	0.27	0.31	0.23	0.36	0.34	0.53	0.54	0.27	0.25

Earlier on (see section 6.2.3) subjects 4, 6 and 10 were excluded from the analysis. Table 6.15 lists the mean phase difference values for the remaining 7 subjects (*entrainment-group*).

Table 6.15: Mean phase difference $\phi_{DA} - \phi_{DA.Mirr}$ calculated for subjects 1, 2, 3, 5, 7, 8 and 9 (the *entrainment-group*), thus excluding subjects that were rejected before based in dipole distances (see section 6.2.3).

Stimulation	0.4	0.45	0.5	0.55	0.6	0.7	0.8	0.9	0.95	1	1.05	1.1	1.2	1.4	1.6
EG Phase Mean	0.11	0.15	0.17	0.24	0.31	0.35	0.3	0.25	0.21	0.2	0.23	0.46	0.43	0.19	0.26

Table 6.15 reveals that the phase differences of the EG phase mean at the lower end of the stimulation spectrum are relatively low. The average phase difference increases beginning at 0.55/0.60*alpha. When the stimulation frequency reaches the interval from 0.9*alpha to 1.1*alpha, the phase difference decrease again, to a level slightly above that from the lower end of the stimulation spectrum. Beginning with 1.1*alpha, the phase difference increase again, but reach another low at 1.4*alpha. Noteworthy is the impact of choosing only the *entrainment-group* of the phase parameters of 0.5*alpha and 1*alpha. The exclusion of 3 subjects from the phase mean decreases the value of the E phase mean by 51.0% (0.5*alpha) or 44.0% (1*alpha), while the mean change is 18.0%. The similar behavior of the mentioned stimulations frequencies with respect to phase and the similarity at other

aspects, which are related to the entrainment behavior (modulation parameter, both belong to the alpha group etc.) suggests that 1) the three subjects do not show alpha entrainment and 2) that the responses at 0.5*alpha and 1*alpha stem from similar states of the underlying oscillatory network.
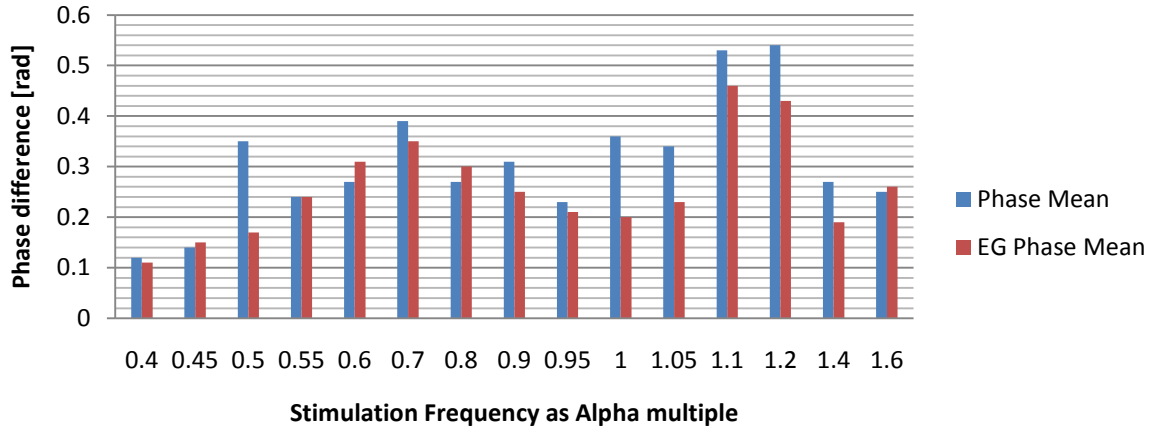
Figure 6.19: Mean of the phase difference $\phi_{DA} - \phi_{DA.Mirr}$ **(y-axis) according to stimulation frequency (x-axis) over all subjects (blue, 'Phase Mean') and mean of the phase difference** $\phi_{DA} - \phi_{DA.Mirr}$ **for subjects belonging to the entrainment-group (red, 'EG Phase Mean').**

6.2.5. Dipole amplitudes

The dipole amplitudes show interindividual magnitude differences. Interindividual normalization compensates for the difference in magnitude and allows for subsequent averaging. The gained average is again normalized to obtain the normalized dipole strength (see Figure 6.20). The mean values and the according STD of the Normalized Dipole Strength are listed in Table 6.16.
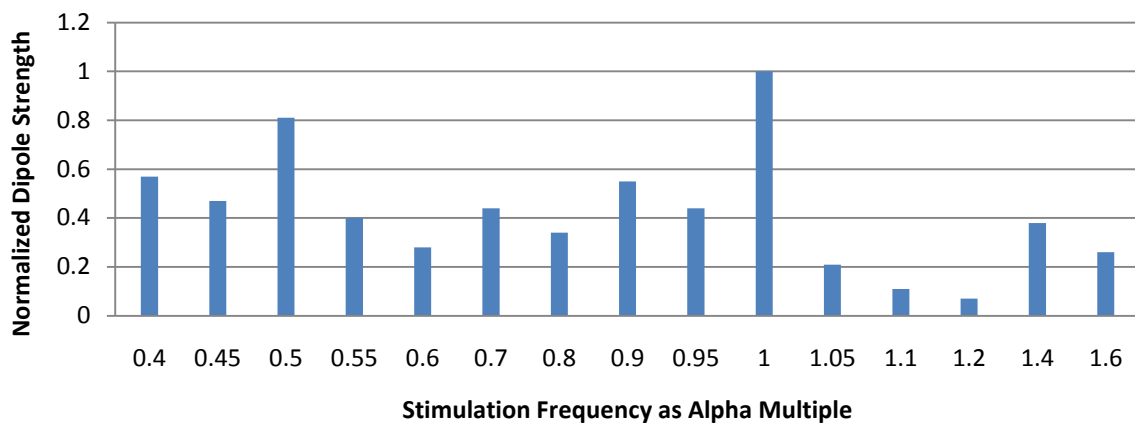
Figure 6.20: The strength of the normalized Dipole Atoms ('Normalized Dipole Strngth', y-axis) plotted versus the stimulation frequency (x-axis) expressed as alpha multiple. Fitted dipoles are stronger for 0.5*alpha and 1*alpha.

Table 6.16 lists also the mean and the standard deviation (STD) of the normalized Dipole Atom strength. According to these values, the confidence interval for 14 degrees of freedom is given by $0.42 \pm 1.345 * 0.25$, thus spans from 0.08 to 0.76. Based on these figures the Dipole Atoms fitted for 0.5*alpha and 1*alpha significantly differ from the Dipole Atoms of the other stimulation frequencies at 10% significance level.

Table 6.16: List of the normalized and averaged strength of the Dipole Atoms and the STD over 10 subjects and the mean of the normalized DA-strength as well as the according STD.

	0.4	0.45	0.5	0.55	0.6	0.7	0.8	0.9	0.95	1	1.05	1.1	1.2	1.4	1.6	Mean	STD
Norm. DA-strength	0.57	0.47	0.81	0.4	0.28	0.44	0.34	0.55	0.44	1	0.21	0.11	0.07	0.38	0.26	0.42	0.25
STD	0.39	0.33	0.5	0.31	0.21	0.35	0.31	0.33	0.36	0.4	0.14	0.12	0.08	0.31	0.24		

6.2.6. GOF results

Table 6.17 shows the values for the obtained values of the goodness of fit GOF_{Meas} for all subjects and stimulation frequencies. The GOF_{Meas} is computed on noisy data, so that values above 90 are not expected (compare to GOF_{Sim} in Table 6.1 for a noise level dependency in the ideal reconstruction case), also the self-evident dissimilarity of the applied forward head model and the real head induces errors (compare Table 6.4). The average Goodness of Fit across the various GOF_{Mean} of the different stimulation frequencies amounts to $GOF_{MeanAvg} = 72.2$. The according standard deviation equals $STD_{GOFAvg} = 5.4$. Thus, with 14 degrees of freedom the 95% confidence interval is given by:

$$GOF_{MeanAvg} \pm 1.761 * STD_{GOFAvg} = 72.2 \pm 9.5. \qquad (6.1)$$

The GOF_{Mean} obtained for 0.4*alpha does, at the 5% significance level, differ from the remaining stimulation frequencies. Possibly 0.4*alpha show a generally lower SNR, which decreases the respective GOF_{Meas}.

Table 6.17: The Goodness of Fit GOF_{Obs} for reconstruction of the real data with one atom and mirrored dipoles show by subject and stimulation frequency. Additionally the mean Goodness of fit GOF_{Mean} for each stimulation frequency and the according STD is given.

GOF_{Obs}	0.4	0.45	0.5	0.55	0.6	0.7	0.8	0.9	0.95	1	1.05	1.1	1.2	1.4	1.6
Subject 1	34.4	48.8	83.1	80.1	78.6	44.9	67.8	82	63.3	89.8	84.4	88.9	83.7	72.4	90.1
Subject 2	63.2	65.2	72	50.6	66	74.3	74.4	77.4	79.3	91.2	75.3	77.2	62.7	76.3	85.5
Subject 3	72.6	78	70.9	59.1	82.3	73.3	74.9	82.5	82.1	81.5	76.8	79.7	79.3	70.5	75.6
Subject 4	54.4	76.9	72.2	83.3	74.5	72.2	78.9	76.4	83.4	81.4	79.4	82.4	73.9	78.8	67.4
Subject 5	65.2	76.7	48.5	73	66.2	71.2	71.9	65.8	56.4	43.1	69.3	72.6	78.3	72.5	75.9
Subject 6	56.6	59.3	61.1	55.5	48.4	67.6	81.2	83.2	63.3	69.3	84.6	60.8	70	67.8	73.5
Subject 7	71.9	72.2	56.2	73.2	78.9	77.4	71	78	95.3	81.6	83.5	78.6	84.4	78.1	80.3
Subject 8	46.8	69.1	63.1	72.7	65.7	63.9	49.1	52.5	66.7	81.1	67.7	61.9	89.6	90.1	85.5
Subject 9	46.4	83.3	63.6	71.5	80.5	78.6	72.5	79.2	72.6	83.8	81.5	65.9	79.6	59.2	77.8
Subject 10	69.6	81.6	68.5	71.3	50	69.5	75.4	78.6	77.3	79.9	61	85.6	42.7	83.4	87.3
GOF_{Mean}	58.11	71.11	65.92	69.03	69.11	69.29	71.71	75.56	73.97	78.27	76.35	75.36	74.4	74.9	79.9
STD	12.7	10.79	9.65	10.57	12.21	9.62	8.82	9.47	11.74	13.7	8.04	9.78	13.5	8.56	7.13

The average $STD_{GOF,Meas}$ calculated for GOF_{Meas} has a mean value of $STD_{GOF,Meas} = 10.4$ and itself shows a $STD_{STD,GOF} = 2.0$, which indicates a relative stability of the GOF_{Meas} and thus stable localization results.

6.2.7. **Average noise level**

As described in section 4.1.1 only one atom is built by averaging the EEG-recordings obtained for the stimuli 10-40. Beside the atom, the Matching Pursuit algorithm yields also residuum (averaged recording minus atom). Hence a signal-to-noise-ratio is estimated from an atom (signal) and the corresponding residuum (noise). This allows for comparing the results obtained from simulated and recorded data. The SNR is estimated by the standard formula (Equation 4.12). Also in this case the power of the signal and the noise are estimated by the periodogram. Thus for each subject a SNR-value is calculated for the data representing each stimulation frequency. Table 6.18 lists the average SNR-value for each stimulation frequency; the SNR-average is calculated across the subjects.

Table 6.18: The SNR, between the forward calculation of the reconstructed mirrored dipole atoms of the first iteration and the residual, averaged across the subjects itemized by stimulation frequency.

Stimulation Frequency	0.40	0.45	0.50	0.55	0.60	0.70	0.80	0.90	0.95	1.00	1.05	1,10	1,20	1,40	1,60
SNR [dB]	15	13	14	17	15	17	16	18	20	20	20	20	18	19	22

The SNR-values given in Table 6.18 lie in an interval from 13db to 22dB. This range of SNR values is covered in the simulations (see Table 4.3). When comparing the SNRs of the simulation and real data one must take into account that there is noise in the real data, which is not white, and thus directly comparing the SNRs may be misleading. Nevertheless, the lower end of the SNR range of the real data may be interpreted as a noise level of approximately 0.5, and the upper end may be interpreted as lying between noise levels 0.1 and 0.2. According to this comparison chart the stimulation frequency of 1*alpha produces a signal with an SNR of 20dB or a noise level of 0.2.

7. Discussion

7.1. Topographic analysis

To my knowledge, for the first time intra-individually similar topographies at stimulation frequencies in an interval close to the individual alpha frequency and half of the alpha frequency are reported, although there has been research in the topographic analysis (Lehmann 1980). Response plateaus in these intervals for both multi-trial and single-trial data are observed. An engaging/disengaging effect in the topographic analysis is discovered for the stimulation frequencies 0.5*alpha and 0.9*alpha to 1.1*alpha. The engagement effect is indicated by the increase of the correlation coefficients over the stimuli 1-10, which is accompanied by an adjustment of the modulation parameter ξ calculated for atoms in the same stimulus interval and stimulation frequency. After the end of the stimulation (stimulus 40), the responses are unchanged until stimulus 42/43. Afterwards the disengagement effect occurs, which becomes apparent in the decrease of the correlation coefficients (i.e.: topographic similarity) as well as the sudden adjustment of the frequency of the atoms. For stimulation frequencies other than 0.5*alpha and 0.9*alpha to 1.1*alpha neither do the observed topographies show similarity to the reference nor do the correlation coefficient sequences show the engaging/disengaging effect.

The modulation parameter ξ increases during the first 10 stimuli for all stimulation frequencies except for 0.4*alpha. Furthermore, for this frequency no decrease of the modulation parameter ξ after the end of stimulation occurs, hence no modulation parameter plateau is detectable. For the remaining 14 stimulation frequencies, a *good* modulation parameter plateau is substantiated by means of a 90% confidence interval. Therefore, the three phases in the modulation parameter plateau can be interpreted as follows: (1) the increase from stimulus 1 to 10 is a tuning of the underlying oscillatory system for almost all stimulation frequencies, although this is not necessarily mirrored by amplitudes or topographic similarities, (2) the plateau from 11 to 42/43, characterized by a small STD, resembles a stable response to the stimulus and thus stable response oscillation which continues for two/three cycles after the end of stimulation, (3) the decrease after the 42nd/43rd stimulus marks the end of the entrainment effect (compare last paragraph in section 2.1.3.3). The effect of part (1) is likely to be based on a forced oscillation, since also for forced oscillations the amplitude of the forced oscillator depends on its eigenfrequency and the stimulation frequency. Furthermore, forced oscillations exhibit a transient behavior at the onset as does the cortical response. Other experiments with flickering light, causing a SSVEP (Fedotchev et al. 1990; Herrmann 2001; Lazarev et al. 2001), do not report an ongoing oscillation after the end of the stimulation.

The overshoots of the modulation parameter (see Figure 5.13) recorded for single-trial activity (at 0.9*alpha and 1*alpha) can be interpreted as a tuning of the oscillators towards the driving frequency. This effect does not occur for 0.5*alpha, which may be due to the difference in stimulation incidence to brain response frequency when compared to 1*alpha.

At 1*alpha, the stimulation frequency and the response frequency are (approximately) identical, so that there is one stimulation per entrained brain oscillation. For 0.5*alpha, however, the stimulation frequency is half the response frequency, which translates to one stimulation per two entrained brain oscillations. The evidence for the tuning, including the overshoot, of the underlying network gained from single stimulation periods of the single-trial analysis has so far -to my knowledge- not been reported in literature.

The responses of 0.4*alpha however do not seem like a forced oscillation. I interpret the lack of such behaviour as a result of the frequency depending attenuation of the underlying cellular structure. The M-cells of the central visual pathway react well to 10Hz stimulation. In this experiment the response in the 10Hz-band is attenuated for low and high stimulation frequencies (see section 5.1.3, Merigan and Maunsell 1993). The notional lower attenuation limit for the stimulation frequency should therefore be in the range of 0.4*alpha and 0.45*alpha. No speculation can be made about the upper attenuation limit, since the responses of the highest stimulation frequency of the experiment (1.6*alpha) show a clear modulation frequency plateau, although a comparably large STD over the stimuli 11 to 40 exists. It can thus be assumed that the alpha system is based on the M-cell-pathway of the visual system. More precisely, the cortical areas/layers/networks in which the M-pathways terminate provide the anatomical basis for the oscillatory structure.

Especially the findings (relatively low power, no modulation parameter plateau) made for the region around 4Hz, more precisely 0.4*alpha, band are confirmed in other experiments. For example (Herrmann 2001) show in the grand average of the fundamental frequency (i.e.: response frequency equals stimulus frequency) that the magnitude of the flicker responses to low stimulation frequencies (~4Hz) is nearly undetectable, a sharp increase follows up to 8-13Hz and thereafter the response slowly degrades until a frequency of about 60Hz.

My research results lead to the conclusion that there is a link between the attenuation frequency and the individual alpha frequency based on the observation that responses to stimulation depend on a subject's individual resting alpha. For example the resting alpha (or 1*alpha) of one subject is 11.8Hz which roughly matches the 1.2*alpha multiple of another subject. Of course the responses magnitudes depend on the alpha factor. The same holds for responses to 0.4*alpha: The highest 0.4*alpha frequency is 4.72Hz, which equals 0.50*alpha for the subject with the lowest resting alpha. Yet the attenuation does occur only around the 0.4*alpha case for both subjects.

The activities approximated by TMP decomposition have similar frequency content in both modalities, MEG and EEG. The observed activity in the EEG mainly stems from the occipital region. Since also the MEG is recorded over the back of the head it can be assumed that EEG and MEG approximate activity that stems from the same source.

The first step of the topographic analysis is the computation of the correlation coefficient sequences between the reference atom and the 40 atoms building it, as well as 10 atoms calculated after the end of the real stimulation. The resulting correlation sequences can be

divided into 3 phases: an increase, a correlation plateau, and a decrease. The latter starts 3 stimulation intervals after the end of stimulation. One may conclude that the visual system needs 5-10 stimuli to produce topographically stable responses which remain stable for 3 virtual stimuli after the stimulation ends. Thus, individually calculated reference atoms can indeed be used as reference for all volunteers.

In the multi-trial analysis, the correlation coefficient sequences have qualitatively the same structure around 0.5*alpha and 1*alpha as have the correlation coefficient sequences described for the reference atoms. In both cases, this occurs for 7 out 10 volunteers, which is in accordance with results for alpha entrainment in the literature (Lazarev et al. 2001).

The results for the single-trial analysis are not as distinct as for the multi-trial analysis. An analogous correlation sequences is found around 0.5*alpha and 1*alpha, but only for 3 out of 10 volunteers. These 3 subjects are the same ones who show the best results in the multi-trial analysis, which leads to the conclusion that the SNR is not sufficient in the other cases.

The reference atom is constructed from stimuli 1-40 instead of 10-40, since all 40 atoms represent the response to the complete stimulation sequence. Additionally, this allows for a better comparability between the correlation sequence of the reference atom with the 40 atoms building it on one hand, and the correlation sequences described above in multi- and single-trial analysis on the other hand. In the multi-trial analysis for 3 volunteers with a reference atom built from stimuli 10-40, no difference is discovered. The increased magnitude of the GFP over the first 7-10 stimuli serves as explanation, since the energy contained in atoms from the early stimuli is comparatively low. The first stimuli have reduced influence on the average of the 40 atoms building the reference.

The initial rise in the correlation sequences is interpreted as an engaging effect of the assumed underlying network of oscillators. This view is supported by the fact that also the amplitudes in the averaged data increase with the first stimulations. The fact, that it takes approximately 10 stimuli to stabilize the responses and about 3 periods to destabilize after stimulation end, suggests that the neural oscillators are tuned in the beginning and de-phase afterwards. For any stimulation frequency other than 0.5*alpha and 0.9*alpha to 1.1*alpha no such behavior is observed. This is in line with the interpretation of (Fedortchev et al. 1990) who note resonance phenomena during their photic driving experiments, when they change the rate of stimulation frequencies from 1 Hz to 15 Hz in steps of 0.05 Hz. However, for steps of 2Hz they observe weaker resonance peaks, which is the consequence of insufficient stimuli of one frequency for a strong resonance to build up.

The topographic engagement and disengagement effects could be observed in slightly more cases for the MEG than for the EEG. Additionally MEG topographies are categorized (see Table 5.2) equally or better (i.e.: more topographies categorized as *good* instead of *moderate*) in comparison to the EEG topographies. This result is in line with (Schwab et al. 2006) who state that their results are more pronounced in the MEG than in the EEG for all volunteers for the same kind of stimulation.

After the introduction of a threshold for the correlation sequences, occipital and frontal regions of interest are found in the EEG. These regions are pronounced for the stimulation frequencies 0.5*alpha and 0.9*alpha to 1.1*alpha and contain higher energy in the occipital patch and lower energy in the frontal region. Based on the topography of the reference atom (Figure 5.7), it is assumed that the occipital patch with higher energy content is produced by two or more sources which are located in the occipital region and influence the frontal region. The model of two active centers would explain the high correlation between channels. The two regions found in the MEG do not contradict my assumption, since the lower energy channels in MEG are located at the margin in direction towards the neck. Note that the MEG channels only cover the back of the head.

Only one atom approximates the response activity, since only the first atoms are significant, although the paired t-test (see section 4.1.1) shows exceptions for 5 cases. The first TMP-atom always has the highest energy content, describing the strongest oscillation in the signal. The first atom describes the major oscillation of one or more symmetric and synchronous sources caused by the rhythmic stimulation, which can also be seen in the power spectra (Schwab et al. 2006). Note that one atom can describe topographies, which might have two or more underlying sources. Based on the results from (Kawaguchi et al. 1993), who state that inter-hemispheric phase difference decreases during photic driving, especially when individual EEG-frequencies coincide with stimulation frequencies, at least two oscillatory sources might be considered. Furthermore (Engel et al. 1989) demonstrate that neurons located in spatially separate columns in the visual cortex can show synchronous oscillatory responses.

The MP-Algorithm is able to approximate the data sufficiently well. In regard to the single-trial analysis the limitation is set by the SNR in some cases.

7.2. Source localization

7.2.1. General aspects

The new method combines features from the Matching Pursuit Method and the source localization to what is called here a Dipole Atom. Dipole Atoms have coordinates in space, a direction and a description of activity given by a Matching Pursuit parameter set. Thus Dipole Atoms allow for sparse signal representation in time, frequency and space. In the case of a mirrored dipole model, also the phases of the underlying sources are maintained. The following subsections discuss the results from verification and application to real data. For all cases (see Table 4.2), except case D, the GOF_{Sim} is on similar levels.

7.2.2. **Simulations**

7.2.2.1. Localization

In general the localization error in all cases is best at the lateral brain shell border and in the occipital region and increases towards the center of the simulated head plane. This holds for case D, which is in fact the most realistic case in the sense that it applies different models for forward and inverse calculations. The method shows its highest localization power in the occipital region, which is required for the analysis of the experimental data. This is explained by the higher electrode density at the back of the head, which leads to better localization results in the underlying area(s).

As expected, case A (see Table 6.1) shows lowest average localization error and variance. The maximum GOF_{Sim} obtained is 99.91. Towards the centre of the simulated head the GOF_{Sim} decreases. On one hand, for case B, an exact localization of single dipole-pairs is possible at higher noise levels than for case A. On the other hand, the maximum localization error for case B is more susceptible to noise than for case A, which is indicated by the higher variance in case B. Additionally, case B describes an area towards the midfrontal plane of the simulated head, in which (comparatively) high localization errors occur. Thus, the approach with two dipoles derives localization precision from phase information (being the only difference between case A and B). Disentangling dipoles without phase difference involves higher cost.

Asymmetries of neural structures stem from differences of tissue distributions between the two brain hemispheres (Toga and Thompson 2003). However, the proposed source model positions the sources symmetrically by minimizing the error, which leads to the loss of exact localization of the neural generators. The susceptibility of the localization by symmetric model to a simulation created by an asymmetric simulation is tested in case C (see also Table 6.3). Case C starts at low noise with a higher average localizations error than case A, but reveals a comparable variance of the localization error. A noise level of 0 in case C produces the same average localization error as a noise level of 0.5 in case A. The variance of the localization error is similar to case A for all noise levels. Additionally the impact of noise in case C causes an increase of the mean error to a (slightly) lesser degree than in case A. The model fits asymmetric geometries and most importantly maintains a small localization variance also if the simulated (or real) sources deviate from the model in matters of geometry.

The impact of different models is described by case D. The localization error in case D at zeros noise is above the levels of case A. The influence of an increase of noise does carry almost no weight in the analyzed noise range. The variance of the localization error, however, remains unchanged as do the minimum and maximum values of the localization error. This does not occur for the other cases. Thus, using different models (3-shell versus 4-shell) has more impact than the simulated noise. The achieved GOF_{Sim} at 0 noise is comparable to the GOF_{Sim} at noise level of 0.1 for case A.

Case E lies in between cases A and B in what regards the mean localization error, its variance and minimum and maximum values. Thus localization also works on a similar level as in cases A and B. In general, the standard TMP performs better than a fixed phase TMP.

7.2.2.2. *Phases*

In general phases are best reconstructed towards the lateral brain shell border. Dipoles directly located on the symmetry axis or one grid point away show the highest susceptibility to phase estimation errors. Phase reconstruction error is already present at low noise levels directly on the symmetry axis. An increase in the noise increases the area in which phase reconstruction error occurs. The area increases towards the lateral border of the brain shell. However, the phase reconstruction error accumulates in a well-defined zone close to the symmetry axis in the cases A, C, D. The existence of this zone cannot be proven or rejected in case B. Phase reconstruction in case E at zero noise produces a small strip on the symmetry axis on which phase errors occur. While this strip is comparable to the area of erroneous phase reconstruction in the other cases, no such zone exists at higher noise levels, where the phase reconstruction errors appear to be randomly distributed in plane.

Case A reproduces phases most reliably, since the mean phase error and the phase error variance are the lowest compared to the other cases. Case C is on a similar level in both measures. This indicates that an asymmetric positioning of the source does not influence the phase reconstruction to a measurable extend.

Case D shows a low mean phase estimation error, similar to case A. However the corresponding variance is double the variance of case A and remains invariant towards the increase in noise. In matters of phase reconstruction, two different models for simulation and solving the inverse problem have less impact than identical phases in the sources.

The phase estimation in case E shows an expected high mean error, since the fix-phased TMP approximation does not take into account the phases in the simulated channels. Reconstruction is therefore impossible. The according variance is similar to case D.

The phase reconstruction in case B has a high variance, of approximately 4 times that of case A, but revealing lower absolute values. I expect that case B and E show similar variances and mean values in the reconstruction of phases, since both construct a TMP-approximation with fixed phases: case B is simulated with 0 phase shift across the channels; case E approximates the simulation with a fixed phase. The variances indeed are on a similar level. However, the mean values of phase reconstruction in case E are 2 to 3 times as big as in case B. Hence, the high mean phase reconstruction error in case E confirms that the fixed-phase estimation method encounters problems in disentangling sources.

7.2.2.3.   Orientation

The reconstruction of direction seems flawed and is prone to error mostly on the symmetry axis and the occipital region of the brain shell. Interestingly, the areas of (high) direction error seem to overlap with the areas of phase reconstruction error (see Figure 7.1). Although this overlap is not perfect, the structures thereof are similar. In the visual comparisons (see Figure 7.1) case E is excluded, since it shows a random distribution of the phase errors over the plane at the chosen noise level. Additionally, the Combined Direction Error encompasses the whole plane.

Of course this visual evaluation does not serve as a confirmation in any way. However, it hints at a process, which yields similarly shaped zones for high phase error and Combined Direction Error for each case respectively on one hand, but also yields different shapes for different cases on the other hand. Cases A, C and D reveal in this regard similar 'L'-shapes. The similarity can be explained by the fact that the respective forward models in cases A and C differ just in parameters, which have no direct influence on the phase reconstruction: the setup of the simulator dipoles is not exactly symmetric. Cases A and D use different models for the inverse solution. A dissimilar 'I'-shaped zone exists in case B. An explanation for the difference in shape can originate in the dissimilarity of case A and case B. Case B diverges from cases A, C and D in so far that the dipole-phase parameter changes in such a way that both simulated dipoles have identical phases. Hence, a relation between the phase error and Direction error is suspected. This excludes an (direct) influence of the localization error, because no overlap to the 'I'- and 'L'-shaped zones can be found.
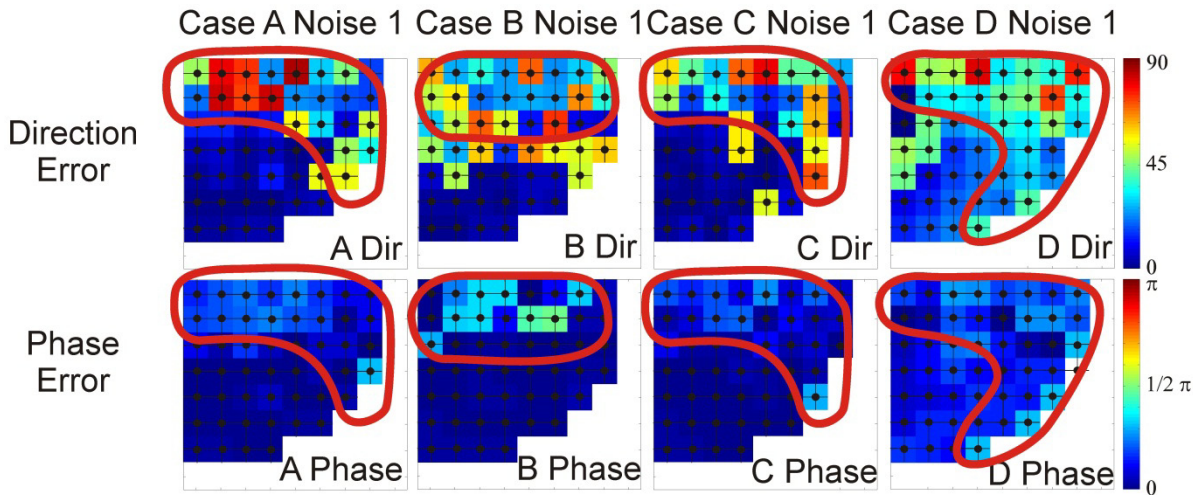
Figure 7.1: Maps of the Direction Error and phase error in the simulated plane for cases A, B, C, D. The subfigures show the results for noise level 1. The Direction Error is color encoded from 0° (blue) to 90° (red). The phase error is color encoded, so that 'blue' signifies no error, while 'red' stands for a phase error of π rad. The color encoding is consistent for all displayed cases. The red lines mark the zone of highest coincidental direction and phase error. White lies outside the brain shell.

Cases A, B, C, E constitute what is also referred to as an "inverse crime" as the forward calculation (the simulated EEG) and the solving of the inverse problem (localization of the Dipole Atom) are based on the same theoretical model (Lead field). In case A, additionally, the underlying geometric setups (sensor positions, symmetric setup of generators) are

identical in the forward and inverse calculations. Under these circumstances, the inverse solution is expected to achieve equality between forward and the inverse solution, if the parameters found for the solution of the inverse problem are identical to the parameters used in the forward calculation (considering simulations, of course). (Colton and Kress 2003) suggest that this is only a trivial solution and should therefore be avoided. Yet (Wirgin 1999) points out that 'committing this crime can, at the very least, reveal the non-uniqueness of the inverse problem'. For inverse solution based on dipole atoms, the non-uniqueness and dependency on the phase is investigated (see section 4.2.6). The calculation of the inverse solution for one dipole atom produces not only the solution of the best estimation of direction, but potentially also 7 other solutions with other estimations of direction, where 6 out of 7 solutions are orthogonal to the best solution and one solution is antiparallel. Each of these 8 results represents one solution for one octant of the Euclidean three-dimensional coordinate system. Case A allows for examination of two dipole atoms. Under the assumption that one of the dipoles is the best direction estimation, the other dipole (note: depends on phase) may be reconstructed as a) the best direction estimate, b) antiparallel to a), or c) orthogonal to a). In the generalized case, it is to be expected that the Combined Direction Error shows also three distinct errors: I) both direction estimations are the best solution, which leads to an error of zero plus error from noise, II) one orthogonal direction estimation error, which leads to an error of 45° ((90°+0°)/2) plus error from noise, and III) an antiparallel direction error leading to a Combined Direction Error of 90° plus error from noise. These expectations match the aggregation of Combined Direction Errors in well separated intervals: e.g., case A, uncovers the occurrence of Combined Direction Error in two separate intervals: 0-5° and 55°-65°. Additionally there also occurs Combined Direction Error in the range of 90°.

7.2.3. **Application to measured data**

7.2.3.1. General findings

As expected from the anatomy/physiology of the brain, the centers of activity are located in the occipital region of the brain where visual information is processed. Due to the low number of subjects - of whom only 7 subjects out of 10 show alpha entrainment - the localization reveals two groups of responses. Thus, the present TMP-based source localization algorithm localizes mirrored sources and reveals new information about the underlying alpha system. Dipole Atoms fitted for 0.5*alpha and 1*alpha differ significantly from Dipole Atoms fitted for other stimulations frequencies in terms of strength (see section 6.2.5). This is expected, since the spectral power densities of the flicker responses show similar results (see section 5.1.3).

7.2.3.2.   TMP-parameter: modulation ξ

The frequency estimation, based on the modulation parameter ξ, of the response frequency of a subject to stimulation with 1*alpha is identical to the estimation obtained by spectral analysis. At 1*alpha stimulation, the response equals the individual resting alpha.

The modulation parameter ξ of the mirrored dipole atoms confirms that the main response frequency is twice the stimulation frequency exclusively for stimulation with 0.5*alpha. Hence, the response frequency at 0.5*alpha correlates with the individual resting alpha frequency. The underlying neural oscillatory network must therefore be tuned to its preferred state in two of the examined cases: first, by stimulation with the resting alpha frequency and, second, by stimulation with half the resting alpha frequency. Therefore I formulate the strong assumption that for both cases the same neuronal network is activated in a similar manner (see section 6.2.3 for the allocation of 0.5*alpha).

For stimulation frequencies ranging from 0.9*alpha to 1.1*alpha the effect of response frequencies close to 1.0*alpha is demonstrated by (Schwab et al. 2006). The findings listed in Table 6.7 verify this for 0.9*alpha and 0.95*alpha. The analysis of (Schwab et al. 2006) at 0.5*alpha reveals for one subject (individual resting alpha 10.7Hz) a response frequency of 10.5Hz, which is equal to a response of 0.98*alpha at a stimulation of 0.5*alpha. This result based on one individual is in line with the results of 7 out of 10 subjects in my analysis. However, the results across all subjects in (Schwab et al. 2006) do not show this effect, and seemingly, do not include the results of the before mentioned single subject.

7.2.3.3.   Localization

For stimulation with 1*alpha, the activity is located in area 17 of the visual cortex, which meets the expectations. Localization results obtained at other stimulation frequencies exhibit distance to a varying degree, but stay in most cases under 1 grid point, which equals to roughly one centimeter. The localization results are divided into two groups. The first ranges from 0.4*alpha to 0.8*alpha and excludes 0.5*alpha and includes 1.4*alpha and 1.6*alpha. The second group originally comprises the range from 0.9*alpha to 1.1*alpha. Following the results from the statistical analysis, I state that the stimulation frequencies 0.5*alpha and 1.2*alpha belong to the second group at the 13% significance level. Therefore the mean distance of 0.5*alpha and 1.2*alpha are (at the 13% significance level) closer to 1*alpha than the members of the other group of stimulation frequencies.

The reason why also 1.2*alpha is closely located to 1*alpha is explained by the observation that stimulation with 1.2*alpha does also elicit topographies similar to those obtained from 1*alpha in few cases (see Table 5.2). For a closer explanation see section 7.3.

The mean distances of 0.45*alpha and 0.55*alpha are far from the ones of the 0.9*alpha-1.1*alpha & 0.5*alpha. Since the modulation parameters ξ differ by factor 2, it becomes

clear, that the responses from 0.45*alpha and 0.55*alpha differ from 0.5*alpha also in terms of frequency. This leads to the conclusion that the neural substrate responds in a different state, or that the responses originate at a different area on the visual cortex, which is supported by the relatively larger distance to the 1*alpha localization.

The experiment (see section 3.1) employs a stimulation of a large portion of the retina if not the entire field of vision. This stimulation pattern should therefore activate (almost) the entire V1 (see Figure 2.2), thus yielding a size of the source. (Andrews et al. 1997) measured mean surfaces of approximately 2400mm² for the V1 of each hemisphere.

7.2.3.1.   Phases

The dipoles at 1*alpha are located close to the symmetry axis. The simulation shows that the phase estimation exhibits the highest variance at and close to the symmetry axis. This introduces a high variance in the phase estimation of the diploes located close to 1*alpha. However, the phase differences of the dipoles replicate the phase differences of the occipital area of the respective hemisphere of the brain. Thus, the results gained by localized dipoles are in accordance with the findings made by (Kawaguchi et al. 1993), who also detect inter-hemispherical phase differences (see section 2.1.3.3).

7.2.3.2.   Directions

The test of the source localization algorithm by simulation reveal that the reconstructions of the dipole directions are inconsistent. However, an assumption of the general orientation of the sources can be made based on the results of the EEG and MEG in the topographic analysis. The topographic effects occur in MEG and EEG recordings, so that the relevant source is picked up clearly by both modalities. This should preclude strictly radial or strictly tangential orientations.

The more tangentially sources are orientated in superficial areas, the higher their SNR in MEG recordings, and thus, the more precise the MEG signal approximation and reconstruction of MEG topographies. A more radial orientation favors the EEG in the same way. In the study of (Goldenholz et al. 2009), the SNR for the MEG is 'often larger' than for the EEG in superficial simulated sources, which are orientated perpendicular to the white/grey matter boundary. My algorithm localizes the neurons activated during the flicker stimulation, in the superficial region of V1. Additionally, in the results of the topographic analysis the MEG shows clearer results. Thus, a more tangential than radial orientation of the underlying oscillator(s) can be concluded.

7.3. Vistas on the visual system during repetitive visual stimulation

During repetitive visual stimulation with flickering light, the visual system is tuned to the stimulation frequency. The exceptions in the present experiment are 0.5*alpha, 0.9*alpha, 0.95*alpha, 1.05*alpha and 1.1*alpha, where the response frequency approximately equals the individual alpha frequency. Thus, these results deviate from the statement formulated before. The prevalent interpretation is that a coupled system of non-linear neural oscillators forms the functional basis.

For topographic analysis this translates to a coupled system of spatially defined oscillators, which generates the specific topographies analyzed above. The specific topography then depends on a specific phase relation of arbitrary value of the oscillators. It is thus reasonable to assume that the phase relation between the oscillators is stable, if stable topographies are detected as in section 5.2. The phases for the localized mirrored diploes are, however, different for stimulation frequencies which show similar topographies. Thus, other areas in the brain must relate to the localized sources in the V1. Typically, the LGN is assumed to function in this role (Lopes da Silva 1991a; Sherman et al. 2001; Bruno et al. 2006). It might also be worth exploring the higher visual centers with a close connection to the M-pathway (dorsal pathway) of higher visual cortices. In fact, there is evidence that cortical regions, other than the primary visual cortex, respond to visual stimulation (Lazarev et al. 2004).

Modeling the sources of the SSVEP with more than just one pair of mirrored dipoles, might also explain the observed characteristic topographies which differ from subject to subject. A model with for example 2 mirrored dipole atom pairs, based on dipole model of the VEP developed by (Di Russo et al. 2001), might be able to describe the individual topographies. Based on the observations of thalamic temporal framing (Lörincz et al. 2009) it might also be expected that an individually fixed phase relation between the two mirrored sources exists, which actually causes the inter-individually differing topographies.

Independent from the position in space, during synchronization, the phase difference between two oscillators remains stable (Pikovsky et al. 2001). Hence, the topographies generated by synchronized (neural) oscillators are stable (disregarding noise from other sources). The synchronization of oscillators depends on two factors. The first factor is the frequency difference between the eigenfrequency of a driven oscillator and the stimulation frequency of the driving oscillator (assuming a driving oscillator of fixed frequency). This is also called detuning. The second factor is the strength of the coupling of the two oscillators. Given a fixed coupling (coupling is constant in the given experiment), the amount of detuning determines if the driven oscillator will synchronize to the driver (Pikovsky et al. 2001). If the detuning is too large, no synchronization (fixed phase relation) occurs.

Interestingly, the opposite occurs in the described experiment. At a certain detuning between the flickering light and the individual alpha frequency (1*alpha - 0.9*alpha = 0.1*alpha, thus detuning of ~1Hz), the visual system is still synchronized to a 1*alpha

generator and not the stimulation. This results in the observed topographic similarities and ongoing oscillations after the end of stimulations. At bigger values for detuning, the visual system responds at a frequency equal to the stimulation. Here no synchronization of oscillators occurs since the topographies do not show intra-trial similarity (for one subject) and no continuation or interruption of oscillation after the end of stimulation occurs. The effect of detuning also depends on the strength of the coupling between the two oscillators. This effect should be detectable in an experiment similar to the one used in this study. The flashes of each stimulation frequency should then be presented in two levels of luminosity. Here a decrease of luminance of the stimulation should lead to an increase in the interval of stimulation frequencies around 1*alpha, which elicit alpha entrainment.

The interpretation of these observations might be, that synchronization occurs only for stimulation at (and close to) subharmonic frequencies, fundamental frequencies and harmonics. In the other cases, the measured frequency is generated from the activity fed through the visual system, thus no intrinsic oscillation occurs.

In case of stimulation at values of detuning just outside the interval which causes synchronization, the underlying oscillators might show synchronization-like behavior for short periods of time. If the coupled system in the visual system is stimulated at 1.2*alpha, phase relations similar to 1*alpha might occur. The topographies obtained at this stimulation frequency might thus, on average, be similar (though not statistically significant) to the reference topography. Furthermore, this similarity can influence the localization, resulting in dipole positions close to 1*alpha.

8. Appendix

Appendix 1: Solutions to optimization condition for one dipole:

Equation 4.10 (see below denoted as Equation 8.1 is solved for variables $dirx, diry$ and $dirz$ and yields 8 solutions:

$$F_{Meas,Sen}^2 - \left((c_{Sensor\,,x}, c_{sensor\,,y}, c_{sensor\,,z}) * cos(\xi t + \phi_{DA}) \begin{pmatrix} dirx \\ diry \\ dirz \end{pmatrix} \right)^2 = 0 \quad (8.1)$$

Solution1:
$$\begin{cases} dirx \to -\dfrac{F_{Maes,Sen}*\text{Sec}\,[\xi t + \phi_{DA}]}{c_{Sensor\,,x}}, \\ diry \to -\dfrac{F_{Maes,Sen}*\text{Sec}\,[\xi t + \phi_{DA}]}{c_{Sensor\,,y}}, \\ dirz \to -\dfrac{F_{Maes,Sen}*\text{Sec}\,[\xi t + \phi_{DA}]}{c_{Sensor\,,z}} \end{cases}$$

Solution 2:
$$\begin{cases} dirx \to -\dfrac{F_{Maes,Sen}*\text{Sec}\,[\xi t + \phi_{DA}]}{c_{Sensor\,,x}}, \\ diry \to -\dfrac{F_{Maes,Sen}*\text{Sec}\,[\xi t + \phi_{DA}]}{c_{Sensor\,,y}}, \\ dirz \to \dfrac{F_{Maes,Sen}*\text{Sec}\,[\xi t + \phi_{DA}]}{c_{Sensor\,,z}} \end{cases}$$

Solution 3:
$$\begin{cases} dirx \to -\dfrac{F_{Maes,Sen}*\text{Sec}\,[\xi t + \phi_{DA}]}{c_{Sensor\,,x}}, \\ diry \to \dfrac{F_{Maes,Sen}*\text{Sec}\,[\xi t + \phi_{DA}]}{c_{Sensor\,,y}}, \\ dirz \to -\dfrac{F_{Maes,Sen}*\text{Sec}\,[\xi t + \phi_{DA}]}{c_{Sensor\,,z}} \end{cases}$$

Solution 4:
$$\begin{cases} dirx \to -\dfrac{F_{Maes,Sen}*\text{Sec}\,[\xi t + \phi_{DA}]}{c_{Sensor\,,x}}, \\ diry \to \dfrac{F_{Maes,Sen}*\text{Sec}\,[\xi t + \phi_{DA}]}{c_{Sensor\,,y}}, \\ dirz \to \dfrac{F_{Maes,Sen}*\text{Sec}\,[\xi t + \phi_{DA}]}{c_{Sensor\,,z}} \end{cases}$$

Solution 5:
$$\begin{cases} dirx \to \dfrac{F_{Maes,Sen}*\text{Sec}\,[\xi t + \phi_{DA}]}{c_{Sensor\,,x}}, \\ diry \to -\dfrac{F_{Maes,Sen}*\text{Sec}\,[\xi t + \phi_{DA}]}{c_{Sensor\,,y}}, \\ dirz \to -\dfrac{F_{Maes,Sen}*\text{Sec}\,[\xi t + \phi_{DA}]}{c_{Sensor\,,z}} \end{cases}$$

Solution 6:
$$\begin{cases} dirx \to \dfrac{F_{Maes,Sen}*\text{Sec}\,[\xi t + \phi_{DA}]}{c_{Sensor\,,x}}, \\ diry \to -\dfrac{F_{Maes,Sen}*\text{Sec}\,[\xi t + \phi_{DA}]}{c_{Sensor\,,y}}, \\ dirz \to \dfrac{F_{Maes,Sen}*\text{Sec}\,[\xi t + \phi_{DA}]}{c_{Sensor\,,z}} \end{cases}$$

Solution 7:
$$\begin{cases} dirx \rightarrow \dfrac{F_{Maes,Sen}*\mathrm{Sec}\,[\xi t+\phi_{DA}]}{c_{Sensor\,,x}}, \\[2mm] diry \rightarrow \dfrac{F_{Maes,Sen}*\mathrm{Sec}\,[\xi t+\phi_{DA}]}{c_{Sensor\,,y}}, \\[2mm] dirz \rightarrow -\dfrac{F_{Maes,Sen}*\mathrm{Sec}\,[\xi t+\phi_{DA}]}{c_{Sensor\,,z}} \end{cases}$$

Solution 8:
$$\begin{cases} dirx \rightarrow \dfrac{F_{Maes,Sen}*\mathrm{Sec}\,[\xi t+\phi_{DA}]}{c_{Sensor\,,x}}, \\[2mm] diry \rightarrow \dfrac{F_{Maes,Sen}*\mathrm{Sec}\,[\xi t+\phi_{DA}]}{c_{Sensor\,,y}}, \\[2mm] dirz \rightarrow \dfrac{F_{Maes,Sen}*\mathrm{Sec}\,[\xi t+\phi_{DA}]}{c_{Sensor\,,z}} \end{cases}$$

9. References

Abeles M., (1982): *Role of cortical neuron: integrator or coincidence detector?*. Israel Journal of Medical Sciences 1982, 18(1):83-92.

Alonso J.M., Usrey W.M. and Reid R.C., (1996): *Precisely correlated firing in cells of the lateral geniculate nucleus*. Nature 383:815–819.

Andersen P. and Andersson SA., (1968): *Physiological basis of the alpha rhythm*. New York, Appleton-Century-Crofts.

Andrews, Halpern and Purves, (1997): *Correlated Size Variations in Human Visual Cortex, Lateral Geniculate Nucleus, and Optic Tract*. J. Neurosci, 17: 2859-2868.

Baillet S., Mosher, J. C. and Leahy R.M., (2001): *Electromagnetic Brain Mapping*. IEEE Signal Processing Magazine, 18: 14-30.

Başar E., (1998): *Brain Function And Oscillations: Volume I: Brain Oscillations. Principles And Approaches*. Springer-Verlag.

BEMFI, Figure 13.2 A, B from http://www.bem.fi/book/13/13.htm; Accessed 24.01.2012.

Berg P. and Scherg M., (1994): *A fast method for forward computation of multiple-shell spehrical head models*. Electroencephalogr. Clin. Neurophysiol., 90: 58–64.

Berger H., (1929): *Über das Elektrenkephalogram des Menchen*. Arch. Psychiatr. Nervenkr. 87:527–570.

Brodmann K., (1909): *Vergleichende Lokalisationslehre der Grosshirnrinde in ihren Prinzipien dargestellt auf Grund des Zellenbaues*. Leipzig: Barth; Tables: Public Domain.

Bruno R. and Sakmann B., (2006): *Cortex is driven by weak but synchronously active thalamocortical synapses*. Science 312, 1622.

Buchli J., Righetti L., Ijspeert A. J., (2008): *Frequency analysis with coupled nonlinear oscillators*. Physica D, doi:10.1016/j.physd.2008.01.014.

Buehren M., (2008): *Differential Evolution*. Version dating: 26.08.2008, Source: http://www.mathworks.com/matlabcentral/fileexchange/18593-differential-evolution.

Castelo-Branco M., Neuenschwander S. and Singer W., (1998): *Synchronization of visual responses between the cortex, lateral geniculate nucleus, and retina in the anesthetized cat*. J. Neurosci. 18: 6395-6410.

Castro-Alamancos M.A. and Connors B.W., (1996): *Cellular mechanisms of the augmenting response: short-term plasticity in a thalamocortical pathway*. J Neurosci, 16: 7742–7756.

Castro-Alamancos M.A., Rigas P. and Tawara-Hirata Y., (2006): *Resonance (approximately 10 Hz) of excitatory networks in motor cortex: effects of voltage-dependent ion channel blockers*. J. Physiol. 2007 Jan 1; 578(Pt 1):173-91.

Chartrian G.E., Bergamini L., Dondey M., Klass D.W., Lennox-Buchthal M. and Petersen I., (1974): *A glossary of terms most commonly used by clinical electroencephalographers*. Electroencephalography and clinical Neurophysiology 37: 538–548.

Connors B.W. and Amitai Y., (1997): *Making waves in the neocortex*. Neuron 18:347–349.

Colton D. and Kress R., (1998): *Inverse Acoustic and Electromagnetic scattering theory*. Springer, Berlin, 1992, p.121, 289 (new edition: 1998, p.133, 304).

Cuffin B.N. and Cohen D., (1979): *Comparison of the magnetoencephalogram and electroencephalogram*. Electroencephalogr. Clin. Neurophysiol. 47: 132–146.

de Munck J.C., van Dijk B.W. and Spekreijse H., (1988): *Mathematical dipoles are adequate to describe realistic generators of human brain activity.* IEEE Trans. Biomed. Engrg. 35: 960–966.

de Tommaso, M., Stramaglia S., Schoffelen J.M., Guido M., Libro G., Losito L., Sciruicchio V., Sardaro M., Pellicoro M. and Puca F.M., (2003): *Steady-state visual evoked potentials in the low frequency range in migraine: a study of habituation and variability phenomena*. International Journal of Psychophysiology 49(2): 165-174.

Di Russo F., Martinez A., Sereno M., Pitzalis S. and Hillyard S.A., (2001): *Cortical Sources of the early components of the Visual Evoked Potential*. Human Brain Mapping 15:95-111.

Durka P.J., Matysiak A., Montes E.M., Sosa P.V. and Blinowska K.J., (2005): *Multichannel matching pursuit and EEG inverse solutions*. J. Neurosci. Methods 148(1):49-59.

Engel A.K., König P., Gray C.M. and Singer W., (1989): *Oscillatory Responses in Cat Visual-Cortex Exhibit Inter-Columnar Synchronization Which Reflects Global Stimulus Properties*. Nature 338(6213): 334-337.

Fedortchev A. I., Bondar A. T. and Konovalov V.F. (1990): *Stability of resonance EEG reactions to flickering light in humans*. Int. J. Psychophysiol. 9(2): 189-93.

Flint A.C. and Connors B.W., (1996): *Two types of network oscillations in neocortex mediated by distinct glutamate receptor subtypes and neuronal populations*. J Neurophysiol. 75:951–957.

Frank E., (1952): *Electric Potential Produced by Two Point Current Sources in a Homogeneous Conducting Sphere*. Journal of Applied Physics 23(11):1225 - 1228

Gratkowski M., Haueisen J., Arendt-Nielsen L., CN Chen A. and Zanow F., (2006): *Time-Frequency Filtering of MEG Signals with Matching Pursuit*. J Physiology-Paris, 99: 47-57.

Gratkowski M., Haueisen J., Arendt-Nielsen L. and Zanow F., (2007): *Topographic Matching Pursuit of spatio-temporal bioelectromagnetic data*. Przeglad Elektrotechniczny 83(11): 138-141.

Gratkowski M., Haueisen J., Arendt-Nielsen L., CN Chen A. and Zanow F., (2008): *Decomposition of biomedical signals in spatial and time-frequency modes*. Methods of Information in Medicine 47(1): 26-37.

Gray H., (1918): *Anatomy of the Human Body.* Philadelphia: Lea & Febiger, 1918; Online edition: Published May 2000 by Bartleby.com; © 2000 Copyright Bartleby.com, Inc., Accessed during 2011 and 2012.

Goldenholz D.M., Ahlfors S., Hämäläinen M.S., Sharon D., Ishitobi M., Vaina L.M. and Stufflebeam S.M., (2009): *Mapping the Signal-To-Noise-Ratios of cortical Sources in Magnetoencephalography and electroencephalography*. Human Brain Mapping 30:1077-1086.

Halbleib A., Gratkowski M., Schwab K., Ligges C., Witte H. and Haueisen J., (2012): *Topographic analysis of engagement and disengagement of neural oscillators in photic driving: a combined electroencephalogram/magnetoencephalogram study*. J. Clin. Neurophysiol 29:33-41.

Hämäläinen M., Hari R., Ilmoniemi R., Knuutila J., and Lounasmaa O.V., (1993): *Magnetoencephalography - theory, instrumentation, and applications to noninvasive studies of the working human brain*. Reviews of Modern Physics, 65: 413-497.

Hara J., Musha T. and Shankle W.R., (1999): *Approximating Dipoles from Human EEG Activity: The Effect of Dipole Source Configuration on Dipolarity Using Single Dipole Models.* IEEE Transactions on Biomedical Engineering 46(2):125-9

Herrmann C.S. and Demiralp T., (2005): *Human EEG gamma oscillations in neuropsychiatric disorders*. Clin. Neurophysiol. 116: 2719–2733.

Herrmann C.S., (2001): *Human EEG responses to 1-100 Hz flicker: resonance phenomena in visual cortex and their potential correlation to cognitive phenomena*. Exp. Brain Res. 137(3-4): 346-53.

Ito H., Gray C. and Viana Di Prisco G., (1994): *Can oscillatory activity in the LGN account for the occurrence of synchronous oscillations in the visual cortex?*. Soc Neuroscience Abstr. 20:134.

Jahnsen H. and Llinás R., (1984a): *Electrophysiological properties of guinea pig thalamic neurons: an in vitro study*. J. Physiol 349: 205-226.

Jahnsen H. and Llinás R., (1984b): *Ionic basis for the electroresponsiveness and oscillatory properties of guinea pig thalamic neurons in vitro*. J. Physiol. 349:227-247.

Jasper H., (1958): *The ten-twenty electrode system of the International Federation*. In: Electroencephalography and clinical neurophysiology. 10:371–375

Jin Y., Potkin S. G., Sandman C.A. and Bunney W.E., (1998): *Topographic analysis of EEG photic driving in patients with schizophrenia following clozapine treatment*. Clinical Electroencephalography 29(2): 73-78.

Jin Y., Potkin S. G., Sandman C.A. and Bunney W.E., (1997): *Electroencephalographic photic driving in patients with schizophrenia and depression*. Biol. Psychiatry 41(4): 496-9.

Kalitzin S., Parra, J., Velis D.N. and Lopes da Silva F.H., (2002): *Enhancement of phase clustering in the EEG/MEG gamma frequency band anticipates transitions to paroxysmal epileptiform activity in epileptic patients with known visual sensitivity*. IEEE Trans Biomed Eng. 49(11): 1279-86.

Kandel E. R., (2000): *Principles of neural science*. (4th ed., pp. 1247–1279). New York: McGraw-Hill.

Karameh F.N., Dahleh M.A., Brown E.N. and Massaquoi SG., (2006): *Modeling the contribution of lamina 5 neuronal and network dynamics to low frequency EEG phenomena*. Biol. Cybern. 4: 289–310.

Kastner S., Schneider K.A. and Wunderlich K., (2006): *Beyond a relay nucleus: neuroimaging views on the human LGN*. Progress in Brain Research 155:125-143.

Kawaguchi T., Jijiwa H. and Watanabe S., (1993): *The dynamics of phase relationships of alpha waves during photic driving*. Electroencephalogr. Clin. Neurophysiol. 87(3): 88-96.

Lazarev V.V., Simpson D.M., Schubsky B.M. and de Azevedo L.C., (2001): *Photic driving in the electroencephalogram of children and adolescents: harmonic structure and relation to the resting state*. Braz. J. Med. Biol. Res 34(12): 1573-84.

Lazarev V.V., Infantosi A.F.C., Valencio-de-Campos D. and de Azevedo L.C., (2004): *Topographic aspects of photic driving in the electroencephalogram of children and adolescents*. Brazilian Journal of Medical and Biological Research 37(6): 879-891.

Lazarev V.V., Pontes A., Genofre M.A. and de Azevedo L.C., (2006): *EEG photic driving in neuropsychiatric diseases in children*. International Journal of Psychophysiology 61(3): 317-317.

Lehmann D. and Skrandies W. (1980): *Reference-free identification of components of checkerboard-evoked multichannel potential fields*. Electroenceph Clin Neurophysiol 48:609-621.

Lehtelä L., Salmelin R. and Hari R., (1997): *Evidence for reactive magnetic 10-Hz rhythm in the human auditory cortex*. Neurosci. Lett. 222:111–114.

Lopes da Silva F.H., Van Lierop T.H.M.T., Schrijer C.F.M. and Storm van Leeuwen W. (1973): *Organization of thalamic and cortical alpha rhythms: spectra and coherences*. Electroenceph. clin. Neurophysiol., 35: 627-639.

Lopes da Silva F.H. and Storm van Leeuwen W., (1978): *The cortical alpha rhythm in dog: the depth and surface profile of phase*. In: M.A.B. Brazier and H. Petsche (Eds.), *Architectonics of the Cerebral Cortex*. Raven Press, New York, 319-333.

Lopes da Silva F.H., Vos J.E., Mooibroek J. and Van Rotterdam A., (1980): *Relative contributions of intracortical and thalamo-cortical processes in the generation of alpha rhythms, revealed by partial coherence analysis*. Electroenceph. Clin. Neurophysiol. 50:449-456.

Lopes da Silva F.H., Amitai Y., and Connors B., (1991a): *Intrinsic oscillations of neocortex generated by layer 5 pyramidal neurons*. Science 251: 432–435.

Lopes da Silva F.H., (1991b): *Neural mechanisms underlying brain waves: from neural membranes to networks*. Electrenc. and clinical Neurophys. 79: 81-93.

Lopes da Silva F.H., (2010): *EEG: Origin and measurement*. Chapter 2 In: *EEG – fMRI Physiological Basis, Technique and Applications*. Editors: Mulert C., Lemieux L., XXII, 539p. ISBN: 978-3-540-87918-3.

Lörincz M.L., Kékesi K.A., Juhász G., Crunelli V. and Hughes S.W., (2009): *Temporal framing of thalamic relay-mode firing by phasic inhibition during alpha rhythm*. Neuron, 63(5):683-696.

Lund J.S., (1988): *Anatomical organization of macaque monkey striate visual cortex*. Annu. Rev. Neurosci. 11:253–288.

Mallat S.G., and Zhang Z.F., (1993): *Matching Pursuits with Time-Frequency Dictionaries*. IEEE Transactions on Signal Processing 41(12): 3397-3415.

Mallat S.G., (1998): *A Wavelet Tour of Signal Processing*. Academic Press.

Merigan W.H. and Maunsell J.H., (1993): *How parallel are the primate visual pathways?*. Annu. Rev. Neurosci. 16:369–402.

Miranda de Sa A.M. and Infantosi A.F., (2005): *Evaluating the entrainment of the alpha rhythm during stroboscopic flash stimulation by means of coherence analysis*. Med. Eng. Phys. 27(2): 167-73.

Mosher J. C., Leahy R. M. and Lewis P. S., (1999): *EEG and MEG: Forward Solutions for Inverse Methods*. IEEE Trans. Biomed. Engineering 46:245-259.

Murakami S. and Okada Y., (2006): *Contributions of principal neocortical neurons to magnetoencephalography and electroencephalography signals*. J. Physiol. 575(3):925–36.

Neuenschwander S. and Singer W., (1996): *Long-range synchronization of oscillatory light responses in the cat retina and lateral geniculate nucleus*. Nature 379:728 –733.

Nunez P.L., Wingeier B.M. and Silberstein R.B., (2001): *Spatialtemporal structures of human alpha rhythms: theory, microcurrent sources, multiscale measurements, and global binding of local networks*. Human Brain Mapping 13:125–164.

Nunez P.L., (1995): *Neocortical Dynamics and Human EEG Rhythms*. Oxford University Press, New York, NY.

Nunez P. L. (1981): *Electric Fields of the Brain*. The Neurophysics of EEG. Oxford University Press, New York, NY.

Odom J.V., Bach M., Barber C., Brigell M., Holder G., Marmor M.F., Tormene A.P. and, Vaegan, (2004): *Visual evoked potentials standard*. Doc. Ophthalmol. 108:115–123.

Parra J., Kalitzin S. N., Iriarte J., Blanes W., Velis D.N. and Lopes da Silva F.H. (2003): *Gamma-band phase clustering and photosensitivity: is there an underlying mechanism common to photosensitive epilepsy and visual perception?* Brain 126(Pt. 5): 1164-72.

Pascual-Marqui R.D., Michel C.M. and Lehman D., (1994*): Low resolution electromagnetic tomography: a new method to localize electrical activity in the brain*. Int. J. Psychophysiol., 18:49–65.

Pikovsky A., Rosenblum M. and Kurths J., (2001): *Synchronization: a universal concept in nonlinear sciences*. Cambridge University Press.

Rager G. and Singer W., (1998): *The response of cat visual cortex to flicker stimuli of variable frequency*. Eur. J. Neurol. 10:1856-1877.

Rush S. and Driscoll D. A. (1968): *Current distribution in the brain from surface electrodes*. Anesth. Analg., 47:717–723.

Sarvas J., (1987): *Basic mathematical and electromagnetic concepts of the biomagnetic inverse problem*. Phys. Med. Biol. 32 11.

Schwab, K., Ligges C., Jungmann T.; Hilgenfeld B., Haueisen, J. and Witte H., (2006): *Alpha entrainment in human electroencephalogram and magnetoencephalogram recordings*. Neuroreport 17(17): 1829-1833.

Sherman S. M. and Guillery R. W., (2001): *Exploring the thalamus*. San Diego, CA: Academic Press.

Sherman S. M., (2007): *The thalamus is more than just a relay*. Current Opinion in Neurbiology 17:417-422.

Sherman S. M., (2009): *Thalamic Mechanisms in Vision.* In: *Encyclopedia of neuroscience*. L.R.Squire (Editor-in-chief), Academic Press Oxford, U.K., 9: 929-944.

Sherman S. M., (2012): *Thalamocortical interactions.* Cur. Opinion in Neurobiology 22:1-5.

Silberstein, R.B., (1995): *Steady-state visually evoked potentials, brain resonances, and cognitive processes*. In: *Neocortical dynamics and human EEG rhythms*. P. L. Nunez. Oxford, Oxford University Press: 272-303.

Sillito A.M., Jones HE., Gerstein GL., and West DC., (1994): *Feature-linked synchronization of thalamic relay cell firing induced by feedback from the visual cortex*. Nature 369:479–482.

Speckmann E.J., Elger C. and Altrup U., (2004): *Neurophysiologic basis of the electroencephalogram*. In: Niedermeyer, E., Lopes Da Silva, F. (Eds.), *Electroencephalography: Basic Principles, Clinical Applications, and Related Fields*. 5th edR Lippincott, Williams and Wilkins, Baltimore, pp. 149–163 (chapter 12).

Stam C.J., Pijn P.J., Suffczynski P. and Lopes da Silva F.H., (1999): *Dynamics of the human alpha rhythm: evidence for non-linearity?.* Clin. Neurophysiol. 110(10): 1801-13.

Steriade M., and Llinás, R. (1988): *The functional states of the thalamus and the associated neuronal interplay*. Physiol. Rev. 68:649-742.

Steriade M., Gloor P., Llinás R.R., Lopes da Silva F.H. and Mesulam M.M., (1990): *Basic mechanisms of cerebral rhythmic activities*. Electroenceph. Clin. Neurophysiol. 76:481–508.

Steriade M., (2000): *Corticothalamic Resonance, states of vigilance and mentation.* Neuroscience 2000 101(2):243-276.

Stok C. J., (1986): *The inverse problem in EEG and MEG with application to visual evoked responses*. Ph.D. thesis, University of Twente, Enschede.

Storn R. and Price K., (1997): *Differential Evolution – A Simple and Efficient Heuristic for global Optimization over Continuous Spaces.* Journal of Global Optimization, Volume 11, Number 4, 341-359, DOI: 10.1023/A:1008202821328.

Sun M., (1997): *An Efficient Algorithm for Computing Multishell Spherical Volume Conductor Models in EEG Dipole Source Localization*. IEEE Trans. Biomed. Engineering, vol. 44, pp. 1243-1252.

Takahashi, T., Kamata K. and Tsukahara Y., (1998): *High-amplitude photic driving response and occipital lobe epilepsy*. Recent Advances in Human Neurophysiology 1162: 565-569.

Tallon-Baudry C. and Bertrand O., (1999): *Oscillatory gamma activity in humans and its role in object representation*. Trends in Cognitive Sciences 3:151-162.

Thut G., Schyns P.G. and Gross J., (2011): *Entrainment of perceptually relevant brain oscillations by non-invasive rhythmic stimulation of the human brain*. Frontiers in Psychology Vol.2, doi: 10.3389/fpsyg.2011.00170.

Toga A.W. and Thompson P.M., (2003): *Mapping Brain Asymmetry*. Nature Reviews Neuroscience 4 (1): 37–48. doi:10.1038/nrn1009. PMID 12511860.

von Helmholtz H., (1853): *Ueber einige Gesetze der Vertheilung elektrischer Ströme in körperlichen Leitern, mit Anwendung auf die thierisch-elektrischen Versuche*. Ann. Phys. Chem. 89:211-233.

Wirgin A., (1999): *Some quasi-analytic and numerical methods for acoustical imaging of complex media*. In: *Wavefield Inversion*. Wirgin A. (ed.), Springer, Vienna.

List of Figures

List of Tables

Erklärung

Ich versichere, dass ich die vorliegende Arbeit ohne unzulässige Hilfe Dritter und ohne Benutzung anderer als der angegebenen Hilfsmittel angefertigt habe. Die aus anderen Quellen direkt oder indirekt übernommenen Daten und Konzepte sind unter Angabe der Quelle gekennzeichnet.

Bei der Auswahl und Auswertung folgenden Materials haben mir die nachstehend aufgeführten Personen in der jeweils beschriebenen Weise unentgeltlich geholfen:

1. Prof. Dr.-Ing. habil. Jens Haueisen: Themenwahl; Interpretation der Analysen

2. Dr.-Ing. Maciej Gratkwoski: Einstieg in Matching Pursuit

3. Dipl.-Ing. Daniel Strohmeier: Beitrag zur Implementierung der Quellelokalisationssoftware

Weitere Personen waren an der inhaltlich-materiellen Erstellung der vorliegenden Arbeit nicht beteiligt. Insbesondere habe ich hierfür nicht die entgeltliche Hilfe von Vermittlungs- bzw. Beratungsdiensten (Promotionsberater oder anderer Personen) in Anspruch genommen. Niemand hat von mir unmittelbar oder mittelbar geldwerte Leistungen für Arbeiten erhalten, die im Zusammenhang mit dem Inhalte der vorgelegten Dissertation stehen.

Die Arbeit wurde bisher weder im In- noch im Ausland in gleicher oder ähnlicher Form einer Prüfungsbehörde vorgelegt.

Ich bin darauf hingewiesen worden, dass die Unrichtigkeit der vorstehenden Erklärung als Täuschungsversuch angesehen wird und den erfolglosen Abbruch des Promotionsverfahrens zu Folge hat.

Konstanz,

Andreas Halbleib